TRANSITIONAL PHENOMENA IN INTERMEDIATE-ENERGY HEAVY-ION REACTIONS

By

Nathan Thomas Boden Stone

A DISSERTATION

Submitted to
Michigan State University
in partial fulfillment of the requirements
for the degree of

DOCTOR OF PHILOSOPHY

Department of Physics and Astronomy

1996

ABSTRACT

TRANSITIONAL PHENOMENA IN INTERMEDIATE-ENERGY

HEAVY-ION REACTIONS

By

Nathan Thomas Boden Stone

Many studies have been performed pertaining to the subject of nuclear matter phase transitions and also related transitions in nuclear reaction decay mechanism. In Chapter 3 we present a study of central heavy-ion collisions in the entrance channels, ^{20}Ne+^{27}Al, ^{40}Ar+^{45}Sc, ^{87}Kr+^{93}Nb, and ^{129}Xe+^{139}La, for a large range of beam energies, for the purpose of identifying transitions in the reaction decay mechanism for those systems. We have defined quantitative measures of the relative sizes of the three largest fragments in these central events using new variables derived from charge Dalitz plots. We then relate the values of these quantities to the predominance of specific reaction decay mechanisms. Transitions from sequential binary disassembly to multifragmentation were observed at $\sim$50 and $\sim$30 MeV/nucleon in the ^{40}Ar+^{45}Sc and ^{129}Xe+^{139}La entrance channels, respectively, and trends observed for the ^{87}Kr+^{93}Nb reactions indicate a similar transition at a beam energy slightly below 35 MeV/nucleon.

Recent theoretical calculations based on transport theories have predicted the occurrence of exotic break-up geometries at intermediate energies. These geometries include bubbles and toroids, which are considered non-compact because of their hol-

low centers, as well as disks. Experimental searches to date have not been able to confirm these predictions. However one group has shown an agreement between their data, for one system at one beam energy, and emission from a toroidal configuration as opposed to a single-source ellipsoidal configuration. In Chapter 4 we present a study of central collisions in the ^{86}Kr+^{93}Nb system at incident energies ranging from 35 to 95 MeV/nucleon. Our results comprise the first systematic experimental results which both provide evidence for the decay of nuclear matter from a toroidal geometry and confine this occurrence to a finite range within the beam energies studied for this system. We use two experimental observables, intermediate mass fragment multiplicities and power-law exponents of ordered charge distributions, to establish that the system decays from a non-compact break-up geometry. We then use event shapes to show that the decaying system is more coplanar in shape, thus implying that the geometry is toroidal. We find that the toroidal geometries are produced for beam energies between 60 and 75 MeV/nucleon.

To my wife Kathy,

to our children both now and yet to come,

and to our LORD.

To you I have pledged my lifelong love and service.

Soli Deo Gloria.

ACKNOWLEDGEMENTS

Here I would like to acknowledge those people who have made substantial contributions to my work, training, and general well-being.

To my advisor, Gary Westfall: I shall be always in your debt for your guidance, insight, support, and even defense. You have counseled me in everything from what to wear to an interview, to what to write in a PRL, to how to survive in East Lansing. Your contribution is not only professional, but personal. Your character and leadership was as compelling to me as your analysis when I first met you as an undergraduate. It is largely to your credit (or blame) that I pursued post-graduate training in physics, and beyond. You have my thanks.

To Skip Vander Molen: You have taught me much of what I know about the art of data acquisition. You have fanned into flame that ember in me which burns for the *real* truth, as opposed to the most convenient interpretation, or straight-line fit. You have bailed me out on many late nights after many long days.

To Robert Pak: You have been a listening ear and an open mind in many discussions of methodology, presentation, FORTRAN, and faith. You are almost always the one to hear my latest ideas first. We have shared many successes as well as trials, and our commonality has been a strength to our friendship, our families, and our work. May it continue to always be so. I am grateful to you for sharing not only your time, but your self with me.

To Bill Llope: You introduced me to PAW and got me started on analysis before I was even started in classes. You also guided me through what was to become my first publication. Thanks for helping to show me the ropes.

To my fellow graduate students: Gene, Yee, Omar, Dan (who told me everything I need to know about Berkeley), Betina, and Justin. Your combined brain power,

camaraderie, humor, and character are what has made being in the 4π group one of the most enjoyable parts of my training. I cannot over-estimate the significance of being accepted, challenged, and appreciated by my peers.

To Paul Simms: Your influence beginning in my early undergraduate years continues to impact my life today. You have been my professor, my employer, my mentor, and my friend. You were also careful not to neglect my character training for my academic training. It was you who first recommended me to my research position as an REU, and to several positions since then.

I am also grateful to the coordinators and participants in the REU program, without whose efforts I would not have seen the side of research which led me to pursue post-graduate training and physics as a career. I must also thank those at the NSCL who have provided the environment that has made my work easier, faster, and better. This includes the computer group in their relentless pursuit of glitch-free programming (and disk storage), the operations group for the beam which I often have taken for granted, and the NSCL faculty as a whole whose combined vision has secured a place for this lab in the future.

A particular thanks must go to Jules Kovacs and Stephanie Holland, for their administrative work on my behalf. Her Serene Highness has faithfully ensured this Humble Servant's enrollment, payment, and otherwise official existence. Your contributions are invaluable.

To my Mother, who could attest from my early years that I am an experimentalist, and to my Father, whose curiosity and lack of inhibitions I have inherited; to my siblings, who forced me at an early age to learn to overcome difficult situations; and to my dog, who unwillingly participated in some of my earliest experiments. You put the "form" in my formative years.

To God, for giving me the talents and predisposition fitting to my task, and for filling my life with "rare and beautiful treasures." To my wife, one such treasure, who has given me her faithful love and support, and many beautiful treasures of her own. Her strength has been my strength, her hopes my hope, and her dreams our dream. For this, and all of her daily sacrifices along the way, my Ph. D. is her Ph. D. "He who finds a wife finds a good thing." I must also thank my wife's family, now my family, who have provided not only the obvious contribution, but who have provided much love and support to us in these past 5 wonderful years.

There are undoubtedly others whose names could fill more pages as their memories fill my mind. My overwhelming sentiment is both of gratefulness and indebtedness. I hope that I will give to those who would ask of me as willingly and fully as those who have given to me.

And last but not least, this work was supported by NSF grants Nos. PHY 89-13815, PHY 92-14992, and PHY-95-28844 (NSCL/MSU). Thank you, tax-payers all.

Contents

LIST OF TABLES ix

LIST OF FIGURES x

1 Introduction 1

1.1 Phase Transitions 1

1.2 Decay Mechanisms 7

1.2.1 Relation to Charge Observables 8

1.3 Non-Compact Geometries 12

2 Experimental 22

2.1 The 4π Array 22

2.2 The Zero Degree Detector 28

2.2.1 Design 29

2.2.2 Construction 35

2.2.3 Detector Response 39

3 Transitions in Decay Mechanism 47

3.1 Dalitz Triangles 47

3.2 Experimental Measurements 53

3.2.1 Mean Distances: D_{cent} and D_{edge} 55

3.2.2 Constraints 57

3.2.3 Acceptance Effects 60

4 Observation of Non-Compact Geometries 64

4.1 Signatures 64

4.2 Experimental Measurements 68

4.2.1 IMF Multiplicity 68

4.2.2 Ordered Charges 70

4.2.3 Event Shapes 76

5 Conclusion **89**

A High Voltage Circuit Components **91**

B Centrality Selection **93**

B.1 Numerical Calculations 94

B.2 Autocorrelations 96

C Simulation Parameter Definitions **100**

C.1 Temperature 101

C.2 Charge and Multiplicity Distributions 104

LIST OF REFERENCES **108**

List of Tables

1.1 Critical exponents extracted from charge moments analysis of 1.0 GeV/ nucleon Au+C listed with values derived from other critical systems [Gilk94]. 5

2.1 Punchin energies for the ZDD, based on 0.67mm thick scintillating plastic. 32

2.2 Azimuthal angles for the ZDD. (Note: Since the ZDD chamber is separate from the 4π ball, if the ball is rotated, these angles will change accordingly. These angles are reported assuming a 3.7° tilt (clockwise, looking down the beampipe) of the 4π ball.) 39

4.1 Definitions of event shape variables. The limiting cases shown in the last columns represent the values obtained for the aspect ratios $\frac{1}{3}$:$\frac{1}{3}$:$\frac{1}{3}$, $\frac{1}{2}$:$\frac{1}{2}$:0 and 1:0:0, respectively[Cugn83]. The definition of Eccentricity depends on the momentum-space configuration. Prolateness (oblateness) is defined via the relation $q_1 - q_2 > (<) q_2 - q_3$. 77

A.1 List of Components for PMT socket. 92

A.2 List of Components for the PMT divider. 92

List of Figures

1.1 The second conditional moment m_2 (see Equation 1.1) plotted versus the reduced multiplicity n for three-dimensional bond percolation lattices. Four different system sizes, $Z_0 = 3^3$(open circles), 5^3(closed circles), 9^3(crosses), and 50^3(triangles), are shown[Camp88]. 2

1.2 Extracted values of the power-law exponent τ versus the calculated temperature for six experimental systems: p+Ag (0.21-4.9 GeV) (circles); p+U (4.5, 5.5 GeV) (crosses); p+Xe and p+Kr (80, 350 GeV) (squares); C+Ag and C+Au (180, 360 GeV) (triangles)[Pana84]. The inset shows a charge distribution at the minimum in τ. 4

1.3 Extraction of the critical exponents (a) β and (b) γ from experimental data [Gilk94] and (c) τ from a percolation calculation [Elli94]. Ordinate and abscissa values are the conditional moments defined in Equation 1.1. 6

1.4 (a) 2-Body and (b) 3-Body asymmetry (defined in the text) plotted versus the centrality variable Z_{bound}[Kreu93]. Markers are mean values extracted for 600 MeV/nucleon collisions of Au on C (circles), Al (triangles), Cu (squares) and Pb (stars). The dotted, dashed and solid lines represent values extracted from GEMINI, COPENHAGEN, and percolation calculations, respectively. 9

1.5 Logarithm of the largest charge versus logarithm of the normalized second charge moment (defined in the text) for (a) 35 MeV/nucleon ^{40}Ca+^{40}Ca data, (b) a multifragmentation model by Sa and Gross, (c) a sequential decay model by Richert and Wagner, (d) the GEMINI sequential decay model[Hage92]. 11

1.6 Surface of constant density ($\rho = 0.3\rho_0$) resulting from BUU calculations of 60 MeV/nucleon ^{93}Nb+^{93}Nb reactions at t=160 fm/c [Baue92]. 14

1.7 Surface of constant density ($\rho = 0.4\rho_0$) resulting from BL calculations of a 3 MeV system of 200 nucleons[Guar95]. The four panels show the reaction at times 0, 40, 80 and 120 fm/c, as labelled. 15

1.8 Density of test-particles in a BNV lattice resulting from calculations of 75 MeV/nucleon ^{90}Mo+^{90}Mo reactions[More92]. The two column groups show the calculation for two different nuclear matter compressibilities, and rows (a)-(d) show the collision at times 20, 60, 120 and 180 fm/c, respectively. 16

1.9 Mean distance from the CM-frame origin (Equation 1.8) in the BUU position lattice versus time for the ^{86}Kr+^{93}Nb system at 7 representative beam energies, as labelled. 19

1.10 Same as Figure 1.9, except using quadratic normalization (Equation 1.9). 20

2.1 Mechanical drawing of the frame of the main 4π ball, revealing the arrangement of the hexagonal and pentagonal faces. 23

2.2 Side view of a hexagonal 4π ball module, revealing three independent layers of plastic and gas detectors. 24

2.3 Arrangement of the forward array phoswiches at the time of data collection for the charge correlations analysis. 26

2.4 The High Rate Array, which consists of 45 close-packed phoswich telescopes. 27

2.5 The Maryland Forward Array, with the outline of the High Rate Array to show positioning. 28

2.6 ZDD High Voltage Circuits. (a) HV divider card. (b) PMT socket card. 31

2.7 The fractional energy loss of fragments ($2 \leq Z \leq 27$) in 0.67 mm scintillating plastic, revealing the "punch-in" energies. 33

2.8 Assembly diagram of the ZDD, showing location of PMTs and light guides. The beam enters from the lower right. 34

2.9 Mechanical drawing of the ZDD chamber. Above: Top view, with beam entering from the top of the page. Below: Rear view, looking upstream. This also shows the goniometer, used for positioning of the detector. 36

2.10 Energy deposited in the ΔE plastic versus time-of-flight for fragments (Z=2-27) in 0.67 mm scintillating plastic, for a 2.74 m flight path. . . 37

2.11 Frontal photograph of the Zero Degree Detector. 38

2.12 Raw experimental data recorded in one ZDD telescope for 45 and 65 MeV/nucleon ^{87}Kr incident on ^{93}Nb. 40

2.13 Calibration points measured in segment 2 of the ZDD. One atomic number (Z=17) and isotope ratio (N=Z) are labelled. 43

2.14 Response function minimization results, comparing Cebra and Birks parameterizations. (a) ΔL Measured vs. Calculated from Cebra parameterization. (b) ΔL Measured vs. Calculated from Birks parameterization. (c) L Measured vs. Calculated from Cebra parameterization. (d) L Measured vs. Calculated from Birks parameterization. . 45

3.1 A Dalitz triangle. For each event, the reduced charges (Z_i') are set equal to the distances to the three sides of the triangle. D_{cent} is the distance from each event entry to the center, and D_{edge} ($= Z_3$) is the distance to the nearest edge. Further features are explained in the text. 48

3.2 Charge Dalitz plots created for the reaction 43 MeV/nucleon Kr+Au [Biza93]. The four panels represent four different excitation energy bins, as labelled. Details of the figure are discussed in the text. . . . 50

3.3 The relative probabilities of populating the three regions in a Dalitz triangle for 43 MeV/nucleon Kr+Au collisions[Biza93]. Each of the three lines has been labelled according to the reaction decay mechanism leading the population of that region in the triangle. 52

3.4 Dalitz plots for central collisions of the the ^{129}Xe+^{139}La system. Beam energies are labelled in each frame. The color contours depict the logarithm of the counts in the histogram. 54

3.5 The average values of D_{cent} (with points) and D_{edge} (without points) in the central events versus the projectile energy. The solid lines depict the results for events selected by the two-dimensional cut on E_t and Z_{mr}, while the dashed (dot-dashed) lines correspond to events selected by a one-dimensional cut on $E_t(Z_{mr})$. 56

3.6 The average values of D_{edge} versus Z_{sum} in the central events for three representative beam energies in MeV/nucleon for each entrance channel, as labeled. The solid lines indicate the minimum and maximum values of D_{edge} that are possible for each value of Z_{sum} by definition. . 58

3.7 The average values of D_{cent} (with points) and D_{edge} (without points) versus the beam energy for specific gates on the quantity Z_{sum}: $6 \leq Z_{sum} \leq 17$ for the ^{20}Ne+^{27}Al and ^{87}Kr+^{93}Nb entrance channels, and $6 \leq Z_{sum} \leq 20$ for the ^{40}Ar+^{45}Sc and ^{129}Xe+^{139}La entrance channels. 61

3.8 The average values of Z_{sum} (upper left frame) and D_{cent} (upper right frame) obtained from eight samples of events, each generated at a specific excitation energy for central ^{40}Ar+^{45}Sc reactions using the Berlin code. Each sample is boosted from the CM frame to the laboratory, and then filtered, for beam energies from 25 to 105 MeV/nucleon. Some points in the upper frames have been offset for clarity by the amounts shown to the right. The lower frame compares the excitation energy dependence of the unfiltered Berlin events with the beam energy dependence of the filtered Berlin events, using BUU calculations to relate the beam and excitation energies for central ^{40}Ar+^{45}Sc reactions. . . 62

4.1 IMF multiplicity versus the total charged particle multiplicity resulting from percolation model calculations[Phai93]. The solid lines (both panels) show the values obtained from percolation of a compact spherical configuration, while the shaded regions show the values obtained from percolation of initial toroid (panel a) and bubble (panel b) geometries. The markers (both panels) show a comparison to an experimental data set. 65

4.2 Mean intermediate-mass fragment multiplicity versus the incident beam energy. 69

4.3 Energy dependance of estimated efficiency for IMF detection, extracted from filtered simulations. 71

4.4 Mean total charge of IMFs versus the incident beam energy. 72

4.5 Ordered Z distributions (markers) for all beam energies, as labelled. The solid line is a fit to the function $\langle Z_{ord}(i) \rangle \propto i^{-\alpha}$. 74

4.6 Power-law (α) values extracted from ordered charge distributions plotted versus the incident beam energy. 75

4.7 Center-of-momentum frame momentum profiles of spherical (top row), disk-like (middle row) and rod-like (bottom row) simulated events. . 78

4.8 Calculated behavior of all shape-variables for simulated spherical(solid lines), disklike (dashed lines) and rodlike (dotted lines) events, plotted versus IMF multiplicity. 80

4.9 Same as Figure 4.8, except plotted versus total charged particle multiplicity, allowing extended (asymptotic) multiplicity scale. 81

4.10 Mean values of sphericity extracted for spherical (dashed), disklike (dot-dashed) and rodlike (dotted) filtered simulations compared to those extracted from the experimental data (solid) for all beam energies, as labelled. 83

4.11 Measured values of the mean sphericity of IMF emission (markers) versus the incident beam energy for three representative IMF multiplicities, as labelled. The dotted (dot-dashed) lines in each case indicate the mean values obtained for filtered spherical (disk-like) simulations. Small offsets have been added for clarity. 84

4.12 Scaled values of all eight shape-variables (as labelled at right) for IMF multiplicity 5. This reveals the suppression or enhancement of the all shape variables at 60 MeV/nucleon. 86

4.13 Cosine values of the azimuthal angles (termed the "flow angles") of the three eigen-vectors of the kinetic energy tensor, plotted versus the incident beam energy. 88

B.1 Two centrality variable distributions for (a) E_t and (b) Z_{mr} (see text for definitions). The unshaded histogram shows the inclusive distribution for System-2 (see text) events, while the horizontally (vertically) shaded sections show the subsets selected by 10% cuts on Z_{mr} (E_t) alone. The intersection of these two subsets shows the portion of the inclusive data selected by simultaneous 10% cuts on both of these variables (roughly 7%). 95

B.2 RMS widths of the charge distributions of first, second and third largest fragments in central events in the ^{40}Ar+^{45}Sc system selected by 5% cuts on 5 centrality variables (as labelled). 98

B.3 Mean charge of the first, second and third largest fragments in central events in the ^{40}Ar+^{45}Sc system selected by 5% cuts on 5 centrality variables (as labelled). 99

C.1 Kinetic energy (per nucleon) spectra (histograms) for ^{7}Li fragments for each energy, as labelled. Each spectra has been fit with a Maxwell-Boltzmann distribution (solid line) in order to extract the emission source temperature. 102

C.2 Kinetic temperatures extracted from energy spectra for ^{7}Li fragments. 103

C.3 Comparison of charged particle multiplicity distributions (histograms) generated by the simulation (top panel) and measured for central events in the experiment (bottom panel). Gaussian distributions have been fit to the data (solid lines) and fit parameters are shown in the upper right corner of each panel. 105

C.4 Same as Figure C.3, except for charge distributions, fitted with exponential functions. 106

C.5 Same as Figure C.3, except for IMF multiplicity distributions. 107

Chapter 1

Introduction

1.1 Phase Transitions

Particular trends in the slopes and functional form of the charge distributions of fragments emitted following central heavy-ion collisions have been noted [Fish67, Baue88, Camp88, Stau79, Hirs84, Finn82] as strong signals for liquid-gas phase transitions in excited nuclei [Fish67, Good84, Pana84]. Many studies have been performed with the intention of providing signatures of these transitions.

One dominant characteristic of phase transitions is the divergence of conditional charge moments[Camp88]

$$m_k(n) = \sum z^k N(z,n)/Z_0 \tag{1.1}$$

where n is the reduced multiplicity, z is the size of the measured fragments, $N(z,n)$ is the number of fragments of charge z in events with reduced multiplicity n, and Z_0 is the largest possible charge (*i.e.* $Z_{targ} + Z_{proj}$). One example of these moments is shown in Figure 1.1. In this figure, the authors have plotted the second conditional moment m_2 versus the reduced multiplicity for three-dimensional bond percolation lattices of sizes 3^3, 5^3, 9^3 and 50^3. The second-order phase transition which occurs in percolation model calculations is clear from this figure. For the largest (effectively

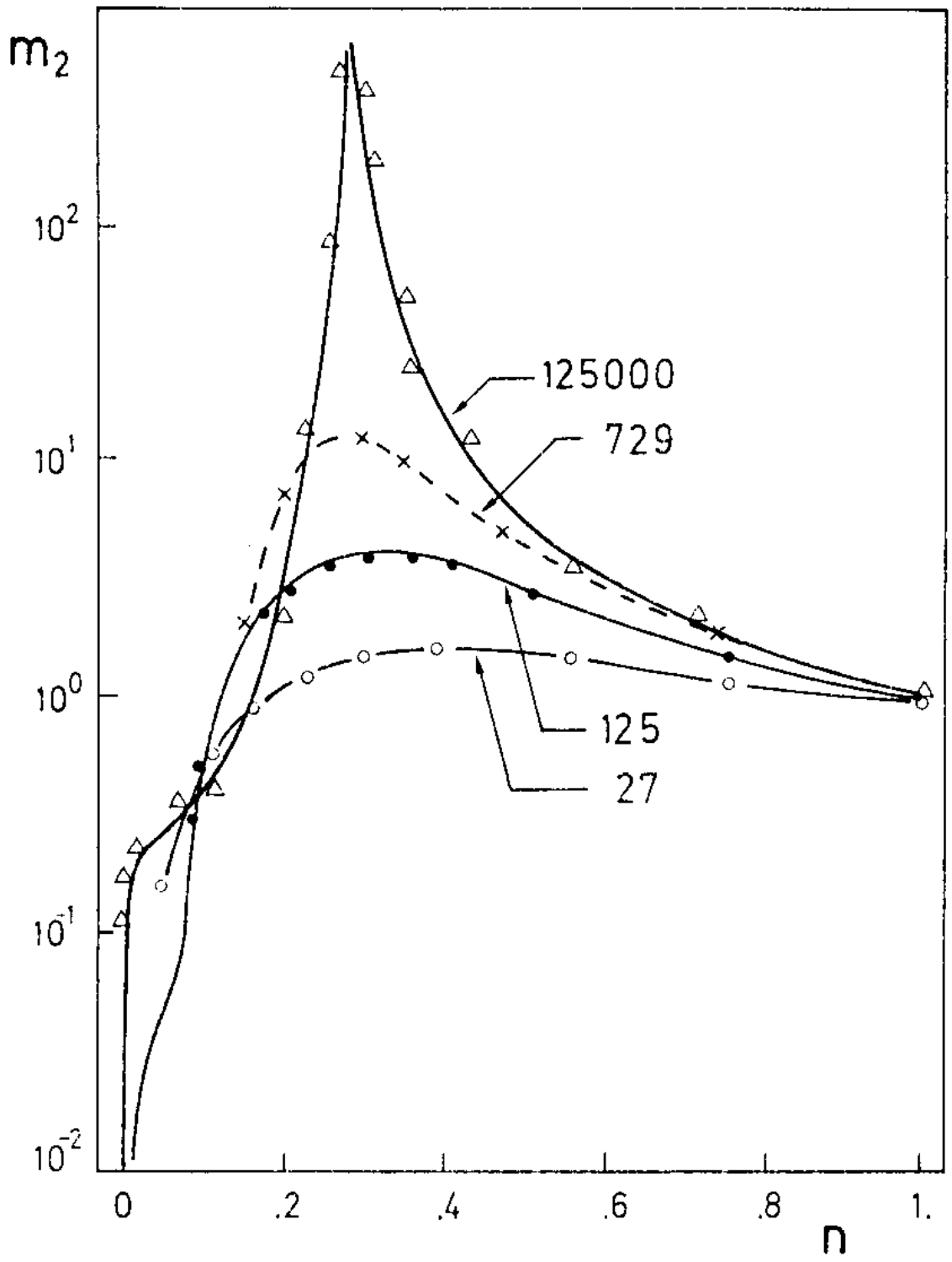

Figure 1.1: The second conditional moment m_2 (see Equation 1.1) plotted versus the reduced multiplicity n for three-dimensional bond percolation lattices. Four different system sizes, $Z_0 = 3^3$(open circles), 5^3(closed circles), 9^3(crosses), and 50^3(triangles), are shown[Camp88].

infinite) system, the singularity occurs at a reduced multiplicity of $n = 0.25$. In smaller (finite) systems, such singularities and other signatures for phase transitions are less prominent, and may be more difficult to extract.

Another example of a phase transition signature is that a relatively shallow power-law charge distribution for charges $1 \leq Z \lesssim 20$ is expected at the transitional excitation energy, as compared to steeper exponential distributions at energies both above and below[Stau79]. It is possible to perform power-law fits ($dP/dz \propto z^{-\tau}$) to experimentally measured charge distributions and search for a minimum in the parameter τ as a signal of the phase transition[Finn82]. This procedure has been followed by the authors of Reference [Pana84]. They have plotted the "apparent exponent" τ versus the extracted source temperature in Figure 1.2 for six experimental systems: p+Ag (0.21-4.9 GeV) (circles); p+U (4.5, 5.5 GeV) (crosses); p+Xe and p+Kr (80, 350 GeV) (squares); C+Ag and C+Au (180, 360 GeV) (triangles). By calling τ the "apparent exponent", the authors acknowledge that this power-law behavior of the fragment charge distributions may also result from averaging over impact parameters or excitation energies [Baue88, Aich88, Li93], imitating the expected signal of a liquid-gas phase transition. This figure shows a clear minimum in the extracted τ value, which is indicative of a phase transition[Stau79, Finn82, Baue88]. The value at this minimum is also consistent with those values extracted for liquid-gas systems[Stan71].

The authors of References [Elli94] and [Gilk94] have provided another indication of phase transitions in nuclear matter. Using the equations describing the decay of systems which display critical behavior [Camp88], they have extracted critical exponents from experimental data collected for 1.0 GeV/nucleon Au+C reactions. By comparing the extracted values to those obtained from actual liquid-gas systems, the authors have provided perhaps the most persuasive arguments to date concerning the liquid-gas -like nature of nuclear matter, although their conclusions

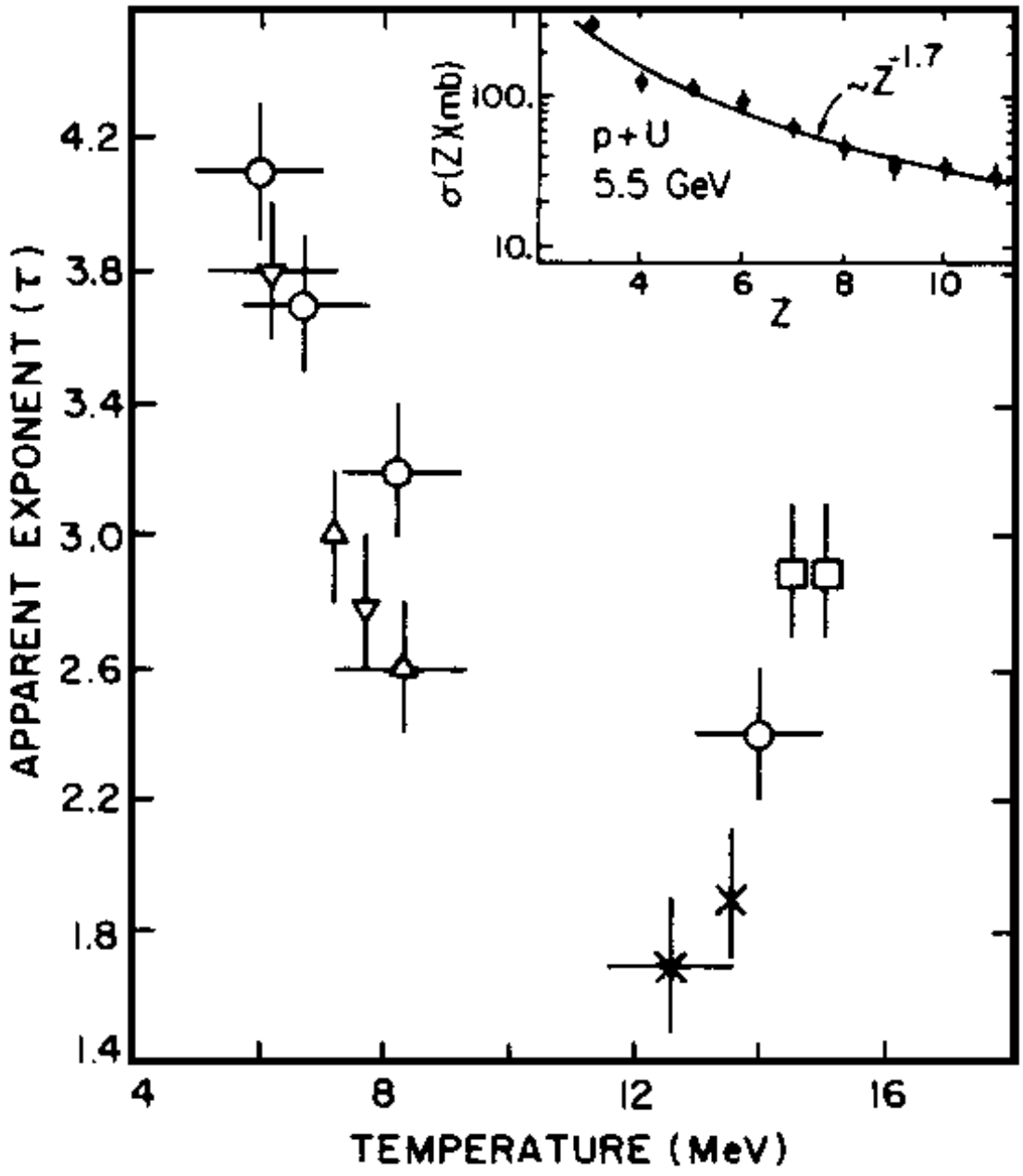

Figure 1.2: Extracted values of the power-law exponent τ versus the calculated temperature for six experimental systems: p+Ag (0.21-4.9 GeV) (circles); p+U (4.5, 5.5 GeV) (crosses); p+Xe and p+Kr (80, 350 GeV) (squares); C+Ag and C+Au (180, 360 GeV) (triangles)[Pana84]. The inset shows a charge distribution at the minimum in τ.

are contested in other works[Baue95]. The equations describing critical systems are as follows:[Camp88, Stau79, Elli94]

$$M_2 \propto |\epsilon|^{-\gamma} \tag{1.2}$$

$$Z_{max} \propto |\epsilon|^{\beta} \tag{1.3}$$

$$N(Z) \propto Z^{-\tau} \text{ (for } m = m_c) \tag{1.4}$$

$$M_3 \propto M_2^{S_{corr}} \tag{1.5}$$

$$\tau = \frac{3S_{corr} - 4}{S_{corr} - 1} \tag{1.6}$$

The exponents γ, β, and τ can all be constrained by the relation

$$\tau = 2 + \frac{\beta}{\beta + \gamma} \ . \tag{1.7}$$

In the above equations, M_2 and M_3 are the second and third conditional moments (see Equation 1.1), ϵ is a measure of the distance from the critical multiplicity (*i.e.* $\epsilon = m - m_c$), $N(Z)$ is the multiplicity of fragments with charge Z, S_{corr} is the slope of the correlation between M_3 and M_2, and γ, β and τ are three critical exponents. By plotting combinations of the conditional moments, Z_{max} and the multiplicity (m) corresponding to Equations 1.2 thru 1.6 (see Figure 1.3), the authors have extracted the values for these exponents listed in Table 1.1. The authors conclude by noting that the values obtained from the experimental data are closest to those observed in liquid-gas systems.

Discussions of transitions in nuclear disassembly can alternatively be phrased in terms of the predominant reaction decay mechanism[Gros93], as transitions in reaction decay mechanism have been observed on the same energy scale[Botv87, Hage92, Cebr90]. The goal of this chapter is to use charge correlations to determine which decay mode is dominant for an experimentally measured set of target-projectile-energy combinations.

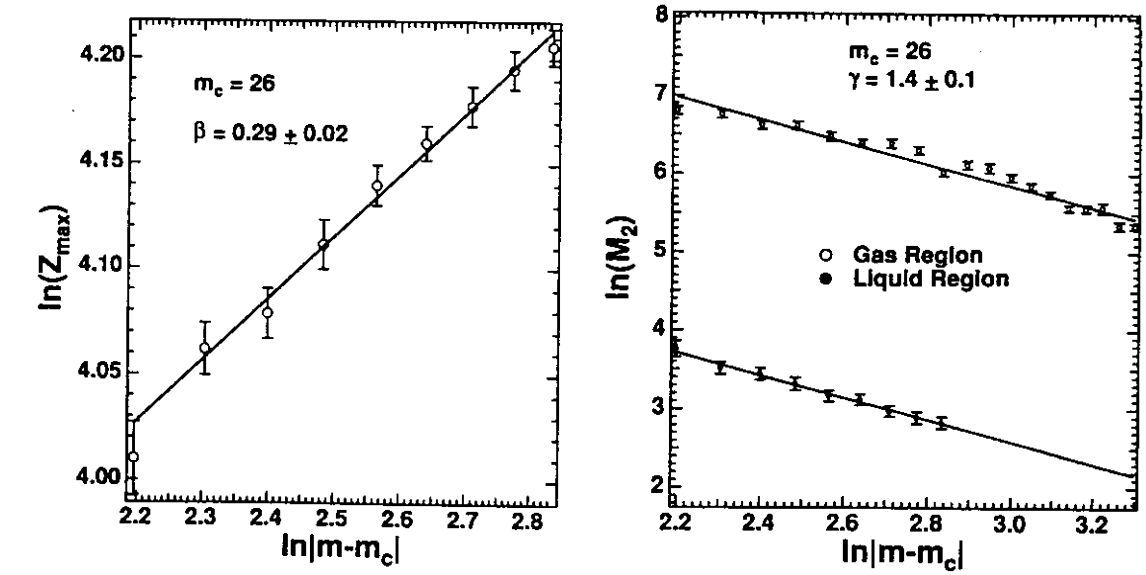

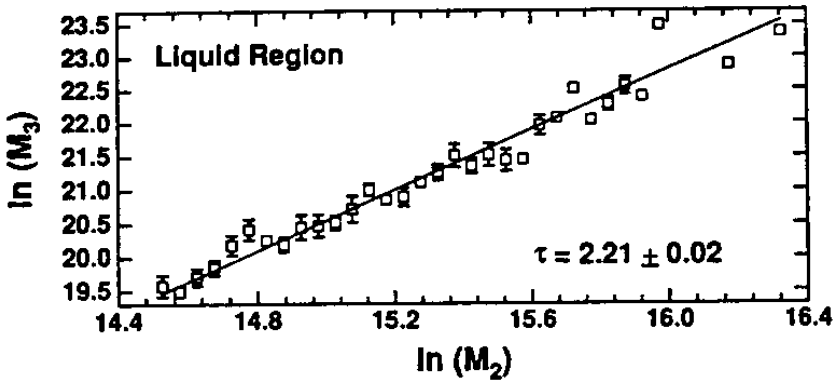

c)

Figure 1.3: Extraction of the critical exponents (a) β and (b) γ from experimental data [Gilk94] and (c) τ from a percolation calculation [Elli94]. Ordinate and abscissa values are the conditional moments defined in Equation 1.1.

Quantity	Experiment	Liquid-gas	Percolation	Liquid-gas mean field
m_c	26 ± 1			
γ	1.4 ± 0.1	1.23	1.8	1.0
β	0.29 ± 0.02	0.33	0.41	0.5
τ	2.14 ± 0.06	2.21	2.18	2.33

Table 1.1: Critical exponents extracted from charge moments analysis of 1.0 GeV/ nucleon Au+C listed with values derived from other critical systems [Gilk94].

1.2 Decay Mechanisms

We will evaluate the predominance of sequential binary (SB)[Barb86, Casi93, Dela86, Siwe93, Sowi86, Pühl77, More93] and multifragmentation (MF) [More93, Barz86, Botv87, Gros87] disassembly mechanisms in small impact parameter events for a range of entrance channel masses and incident beam energies. The observation of a transition from SB disassembly to MF for increasing beam energies would be suggestive of the transition from liquid to liquid-gas coexistence phases, i.e. the "cracking" transition, that has been predicted by several models [Barz86, Botv87, Gros87, Gros93]. We classify as sequential binary those disassembly mechanisms involving a cascade of two-body decay steps, in which each step is independent and may involve (a)symmetric binary fission [Barb86, Casi93, Dela86], (a)symmetric ternary fission [Siwe93, Sowi86], or evaporation [Barb86, Pühl77]. Over the course of a purely evaporative SB decay, the probability of emitting large fragments decreases due to the increasing importance of the Coulomb and angular momentum barriers. The three largest charges in final states produced in such SB decays would thus be expected to consist of one larger fragment and two smaller ones. A binary or ternary fission step in the SB decay cascade would result in the emission of two larger fragments and one smaller one. Disassembly leading to three similarly sized largest fragments has been noted as a signal for the process known as multifragmentation[More93, Barz86, Botv87, Gros87].

1.2.1 Relation to Charge Observables

Previous work has been done to investigate the effects of the decay mechanism upon the charges of the resulting fragments. In one study[Kreu93], the authors compared results from three different models to their data using quantitative measures of charge symmetry to determine the sensitivity of charge-based observables to different

methods of populating phase space in nuclear decay processes. Two of the models compared were hybrid combinations of dynamical and statistical calculations. The Boltzmann-Uehling-Uhlenbeck model (BUU)[Bert88], a dynamic transport model, was used to describe the first stage of the collision. The second stage of the collision was described by each of two statistical models. The first was the GEMINI model[Char88], a sequential binary decay model, and the second was the COPENHAGEN model[Bond85], a simultaneous multifragmentation model. The version of COPENHAGEN called CRACKER was used, which includes a specialized treatment of the evaporation stage. The third model compared was a 3-dimensional bond percolation model[Desb87, Baue88].

The authors of that study calculated two- and three- body asymmetries for the largest three fragments on an event-by-event basis. The two-body asymmetry is defined as $(Z_{max} - Z_2)/(Z_{max} + Z_2)$ and measures the asymmetry of the first and second largest charges. The three-body asymmetry is defined as

$$a_3 = \sqrt{(Z_{max} - \langle Z \rangle)^2 + (Z_2 - \langle Z \rangle)^2 + (Z_3 - \langle Z \rangle)^2}/\sqrt{6}\langle Z \rangle$$

where $\langle Z \rangle = \frac{1}{3}(Z_{max} + Z_2 + Z_3)$, and measures the asymmetry of the combination of the largest three charges. The mean values of these asymmetries are plotted in Figures 1.4(a) and 1.4(b) versus a centrality variable Z_{bound}. Z_{bound} is defined as the sum of the charges of all bound fragments ($Z \geq 2$). With this definition, central (peripheral) collisions should result in small (large) values of Z_{bound}.

The data shown in this figure were collected for 600 MeV/nucleon collisions of Au on C (circles), Al (triangles), Cu (squares) and Pb (stars). The mean asymmetry values found for these systems is similar for all values of Z_{bound}. Superimposed over this figure are the resulting mean values extracted from the sequential binary decay model GEMINI (dotted lines), the simultaneous multifragmentation model COPEN-

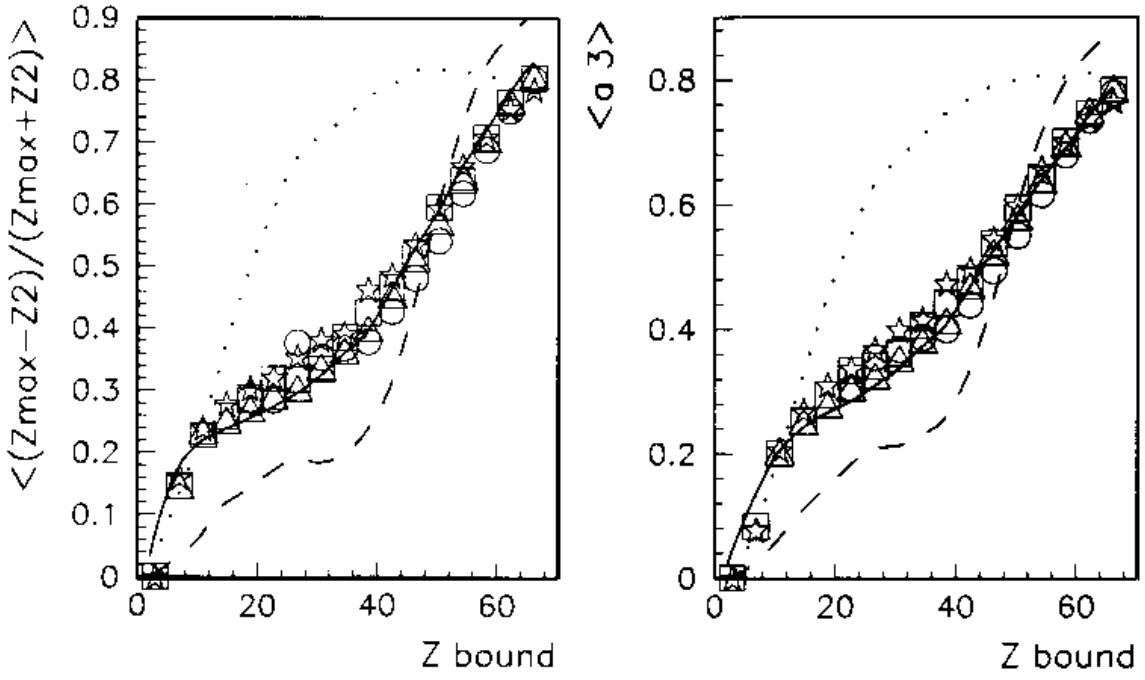

(a) (b)

Figure 1.4: (a) 2-Body and (b) 3-Body asymmetry (defined in the text) plotted versus the centrality variable Z_{bound}[Kreu93]. Markers are mean values extracted for 600 MeV/nucleon collisions of Au on C (circles), Al (triangles), Cu (squares) and Pb (stars). The dotted, dashed and solid lines represent values extracted from GEMINI, COPENHAGEN, and percolation calculations, respectively.

HAGEN (dashed lines) and the percolation model (solid line). While the percolation model has good agreement with the data for all Z_{bound}, for mid-peripheral events the GEMINI values are considerably higher than the data and the COPENHAGEN values considerably lower. The authors point out that some input parameters to these models could have been adjusted to improve the overall agreement with the data, and even that the point at which the BUU calculation was stopped (determining the input configuration for the statistical models) could have been changed. However, the authors' goal was not to show agreement or disagreement between their data and the models, but to explore the sensitivity of their experimental observables to the fundamentally different methods of populating phase space in the three models. These figures clearly illustrate the quantitative differences in charge symmetry which one may expect to observe due to the predominance of fundamentally different reaction decay mechanisms.

Another study also illustrates similar sensitivities of charge observables to the decay mechanism. The authors of this study[Hage92] also perform calculations using hybrid models. The first stage of these models was described by BUU calculations, which provided input parameters to each of three statistical models. The statistical models were: a simultaneous multifragmentation model by Sa and Gross[Sa85, Zhan87a, Zhan87b], the GEMINI sequential decay model[Char88], and another sequential decay model by Richert and Wagner[Rich90].

The experimental data used in the comparison were collected for collisions of 35 MeV/nucleon ^{40}Ca+^{40}Ca. The charge observables examined here were the largest detected charge (Z_{max}) and the normalized second moment of the charge distribution with the largest charge excluded:

$$S_2 = \frac{\sum_{i,Z\neq Z_{max}} Z_i^2 M(Z_i)}{\sum_{i,Z\neq Z_{max}} Z_i M(Z_i)}$$

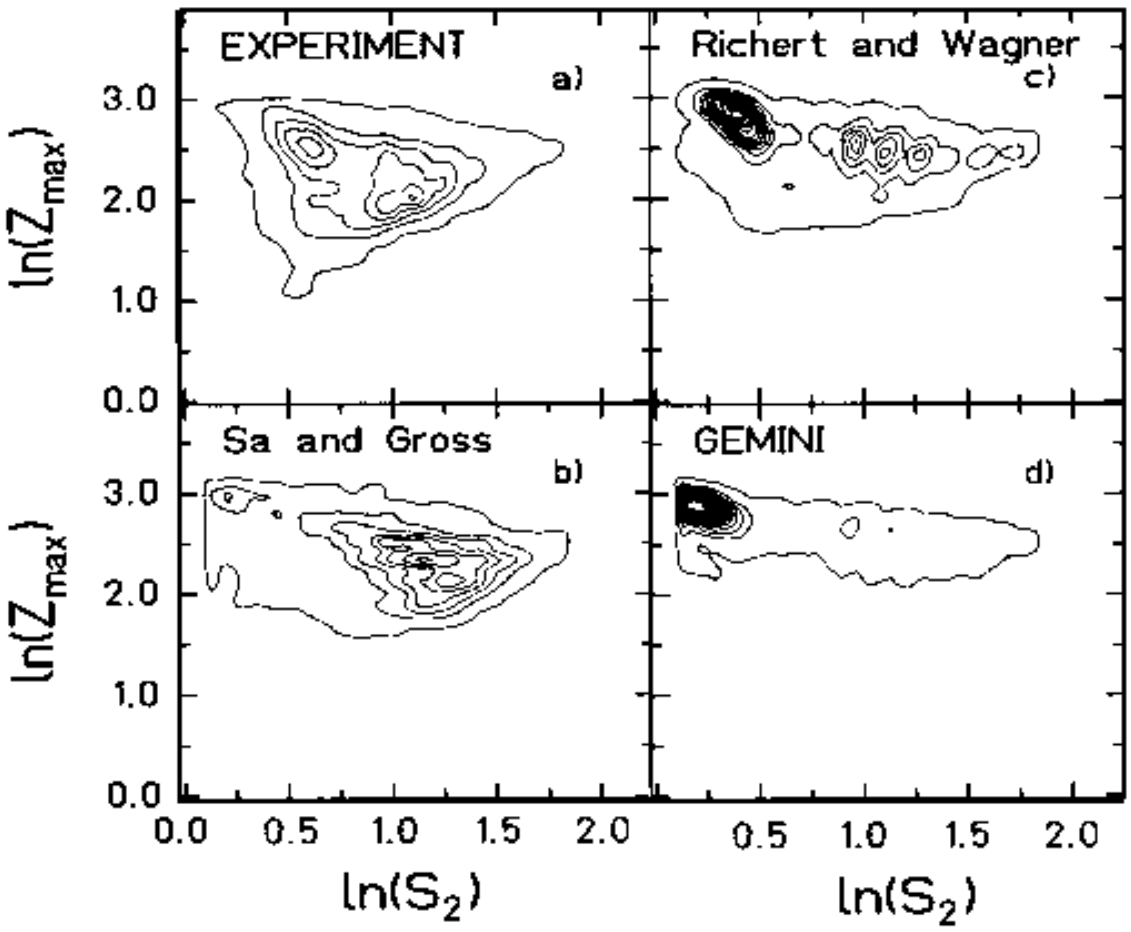

Figure 1.5: Logarithm of the largest charge versus logarithm of the normalized second charge moment (defined in the text) for (a) 35 MeV/nucleon ^{40}Ca+^{40}Ca data, (b) a multifragmentation model by Sa and Gross, (c) a sequential decay model by Richert and Wagner, (d) the GEMINI sequential decay model[Hage92].

where $M(Z_i)$ is the multiplicity of fragments with charge equal to Z_i. Figure 1.5 shows contour plots of $\ln(Z_{max})$ versus $\ln(S_2)$ for the experimental data (panel a), the multifragmentation model by Sa and Gross (panel b), and the sequential decay models by Richert and Wagner (panel c) and GEMINI (panel d). Two predominant peaks appear in the plot for the experimental data. The authors of that work attribute the population of the first peak (at $\ln(S_2) \approx 0.5$) to the sequential decay mechanism, and the population of the second peak (at $\ln(S_2) \approx 1.2$) to the multifragmentation mechanism. By comparing the relative strengths of these two peaks to those yielded

from the model calculations, it is clear that the pure multifragmentation model over-populates the second peak, while the sequential decay models over-populate the first peak. The authors continue by showing that sequential codes modified to include expansion[Frie88, Frie90] are better able to reproduce the admixture of charge symmetry with charge asymmetry.

For the purposes of this thesis, we concentrate on the commonality between these two studies, which is the establishment of the fact that purely sequential decay mechanisms generally yield asymmetrically charged reaction products while purely multifragmentation models yield symmetrically charged fragments. Since previous work has shown good agreement between experimental data and sequential model calculations for low energy nuclear collisions[Bada93, Barb86], and similar agreement between experimental data and simultaneous multifragmentation model calculations at higher energy collisions[Botv87, Hage92, Cebr90], it is reasonable to expect a transition in the predominant reaction decay mechanism at some intermediate beam energy. The two studies presented above have further shown a correspondence between the specific behavior of fragment charge observables and the predominant reaction decay mechanism.

1.3 Non-Compact Geometries

Recent theoretical calculations based on transport theories have predicted the occurrence of exotic break-up geometries at intermediate energies[More92, Baue92, Gros92, Xu93, Souz93, Guar95]. These geometries include bubbles and toroids, which are considered non-compact because of their hollow centers, as well as disks. In Figure 1.6 is shown a surface of constant density ($\rho = 0.3\rho_0$) resulting from Boltzmann-Uehling-Uehlenbeck (BUU)[Bert88] model calculations[Baue92]. The system was ^{93}Nb+^{93}Nb

at 60 MeV/nucleon incident energy, and this Figure depicts the density configuration for a single time at 160 fm/c. The toroidal ring in the density profile is quite clear in this figure.

Figure 1.7 shows another surface of constant density ($\rho = 0.4\rho_0$) resulting from Boltzmann-Langevin (BL)[Ayik90] model calculations[Guar95]. The system was prepared with 200 nucleons at a temperature of 3 MeV. This Figure illustrates the time-progression of the density configuration at times 0, 40, 80 and 120 fm/c. The emergence of a bubble occurs in these calculations roughly at 40 fm/c, after which point the shell decays into 5 large proto-fragments.

Figure 1.8 shows a time progression of a nuclear collision, illustrated by the density of points, resulting from Boltzmann-Nordheim-Vlasov (BNV)[Bona92] model calculations[More92]. The system was ^{90}Mo+^{90}Mo at 75 MeV/nucleon incident energy. Rows (a) thru (d) show density profiles for the times 20, 60, 120 and 180 fm/c, respectively, and the two column groups show the calculation for two different nuclear matter compressibilities (K). The profile of a disk can be seen in row (c) for the high compressibility case, while a toroid can be seen in row (d) for the low compressibility case. However, even these distinctions appear somewhat subjective in this figure.

What is common to each of these results is that there does not appear a simple ellipsoidal structure expanding outward from the origin. There appears in each case some exotic configuration. In this discussion, we now make one important distinction among these three examples. While the first two, the toroid and the bubble, have a hollow center, the disk does not. This quality is the origin of the term "non-compact" geometry, which we hereby qualitatively define to mean any position-space configuration of nuclear matter with a hollow center. This includes bubbles and toroids but excludes disks. While experimental predictions and discussions regarding such geome-

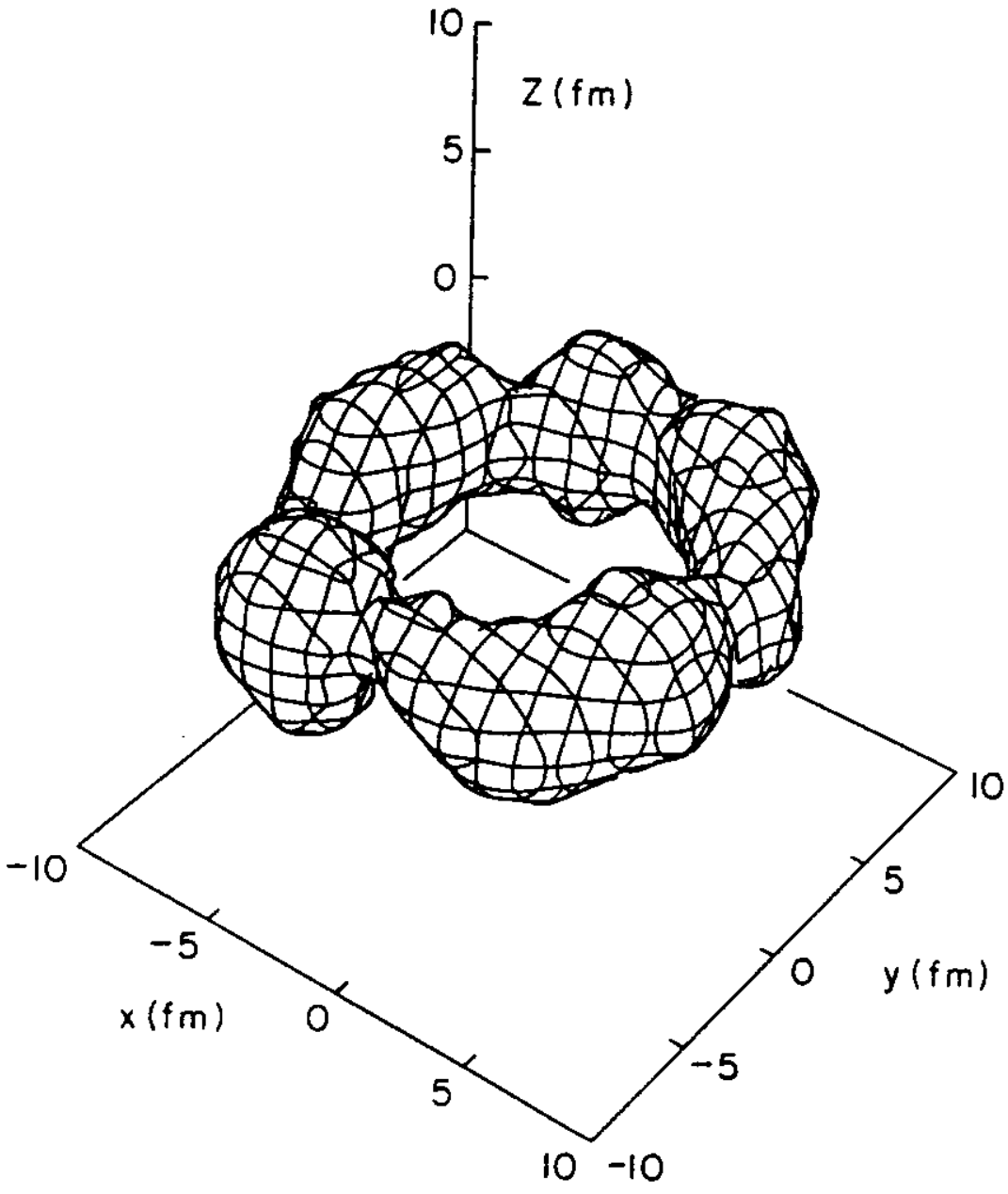

Figure 1.6: Surface of constant density ($\rho = 0.3\rho_0$) resulting from BUU calculations of 60 MeV/nucleon ^{93}Nb+^{93}Nb reactions at t=160 fm/c [Baue92].

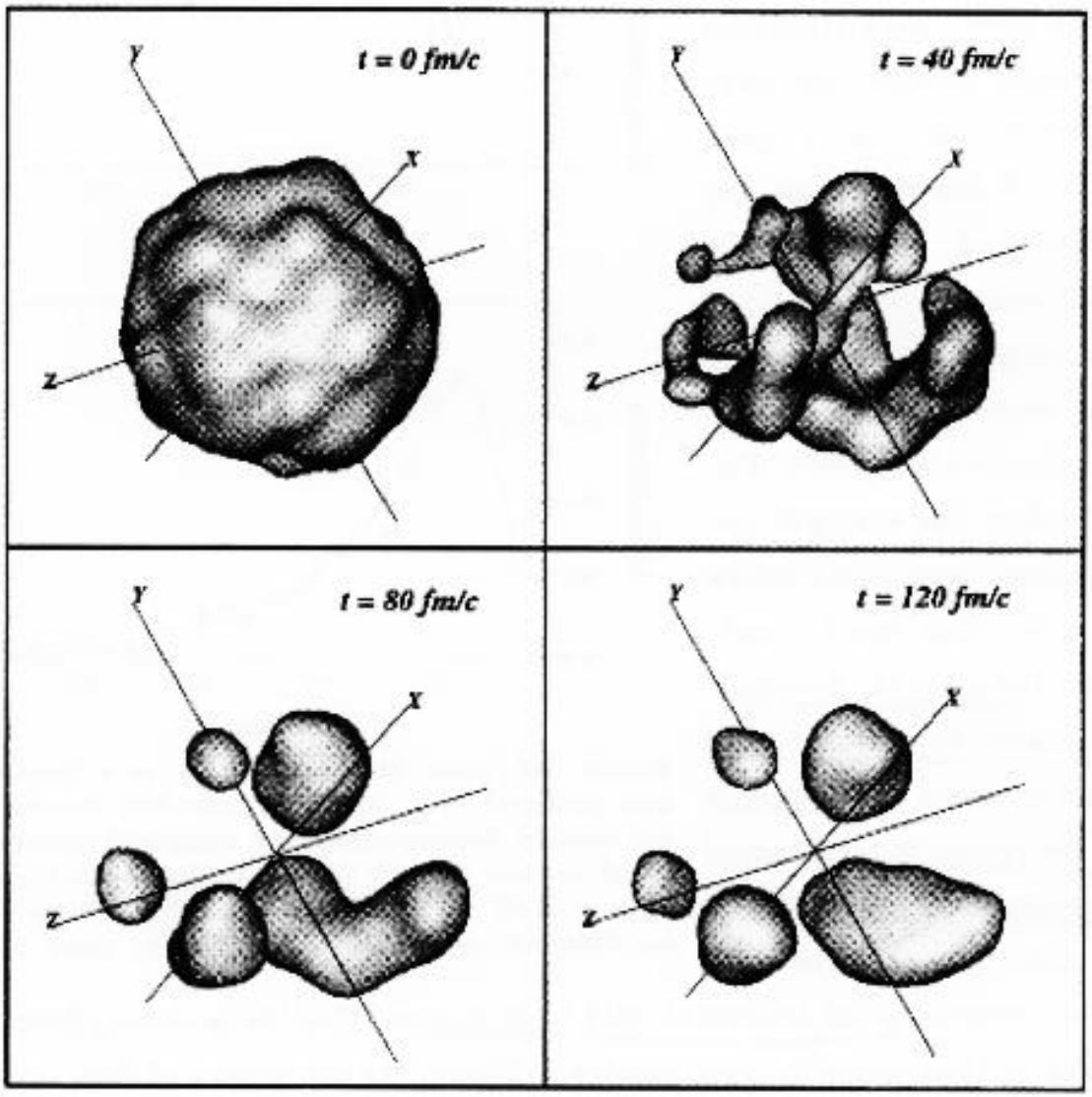

Figure 1.7: Surface of constant density ($\rho = 0.4\rho_0$) resulting from BL calculations of a 3 MeV system of 200 nucleons[Guar95]. The four panels show the reaction at times 0, 40, 80 and 120 fm/c, as labelled.

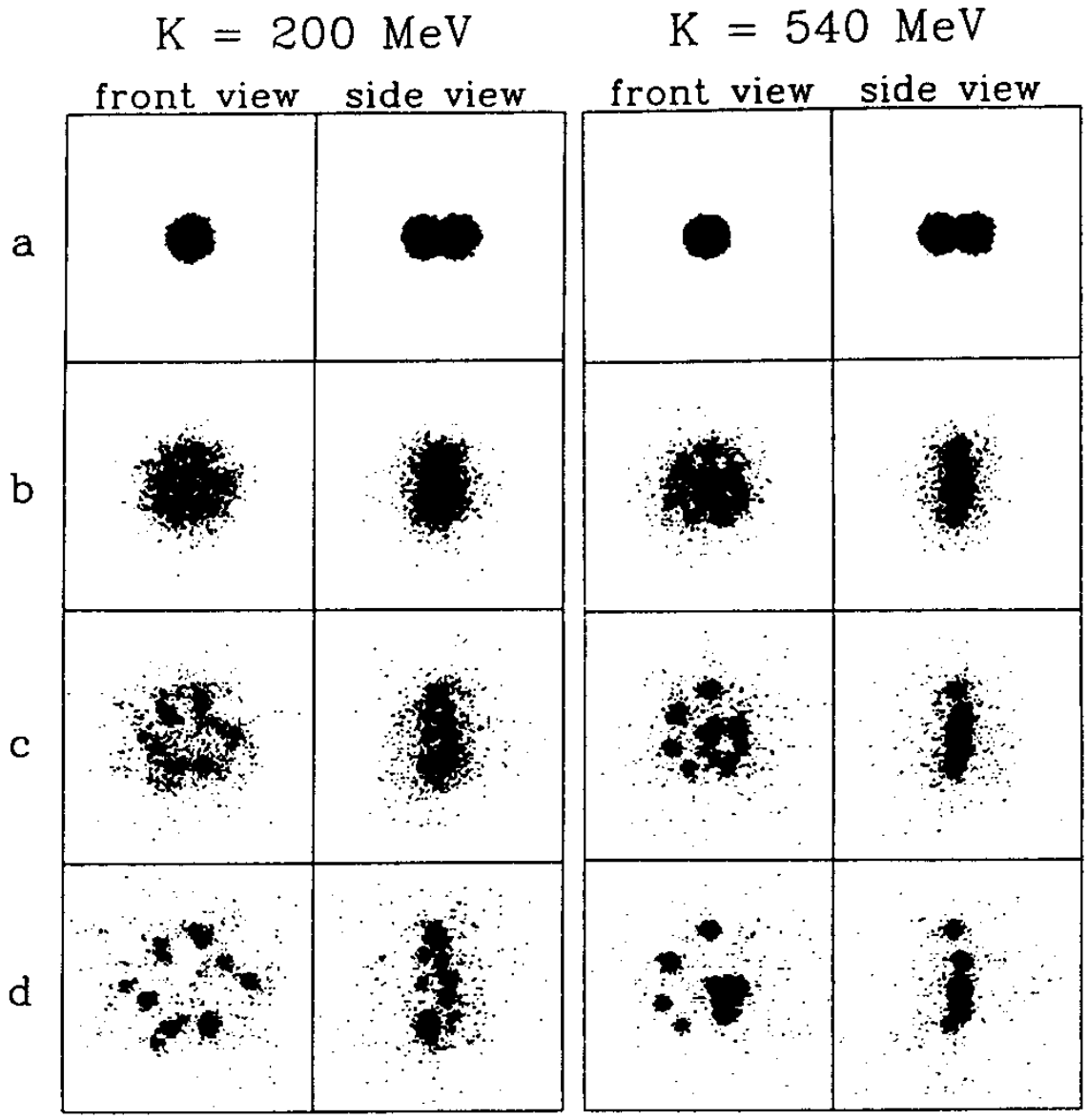

Figure 1.8: Density of test-particles in a BNV lattice resulting from calculations of 75 MeV/nucleon ^{90}Mo+^{90}Mo reactions[More92]. The two column groups show the calculation for two different nuclear matter compressibilities, and rows (a)-(d) show the collision at times 20, 60, 120 and 180 fm/c, respectively.

tries flourish, experimental searches to date have not been able to confirm predictions regarding the existence of non-compact geometries[Glas93, Phai93, More96]. One group, however, has shown an agreement between their data, for one system at one beam energy, and emission from a toroidal configuration as opposed to a single-source ellipsoidal configuration[Dura96].

It is a goal of this thesis (see Chapter 4) to provide experimental evidence which either confirms or refutes claims regarding the decay of nuclear matter from a non-compact geometries. In order to do this, we rely upon the predictions of theorists who have examined model calculations and have provided both qualitative and quantitative descriptions of observables sensitive to the formation/decay of these exotic geometries. These observables, termed signatures, provide criteria suitable for a confirmation of the appearance (and disappearance) of non-compact geometries in the early stages of nuclear interactions. We have performed a study of central collisions in the ^{86}Kr+^{93}Nb system at incident energies ranging from 35 to 95 MeV/nucleon. The results we present comprise the first systematic experimental results which both provide evidence for the decay of nuclear matter from a toroidal geometry and confine this occurrence to a finite range within the measured beam energies for this system.

One author has commented on the role of expansion, specifically a stall in the expansion of the combined system, in the formation of bubble and toroid structures.

> "When a compressed sphere expands radially, a rarefaction wave propagates from outside towards the center, leaving matter at normal density streaming outward. When the wave reaches the center, the outward streaming matter depletes the center, sending the density to a low value. At low energies the system slows down and recompresses the hole, but at higher energies, ..., the bubble grows."[Baue92]

As an illustrative example of this, we have run BUU model calculations for the ^{86}Kr+^{93}Nb system and have calculated a mean radial distance from the center of the position-space lattice for the ensemble averaged nuclear density:

$$\langle R_1 \rangle = \frac{\sum_{i,j,k} \rho(i,j,k) r(i,j,k)}{\sum_{i,j,k} \rho(i,j,k)} \tag{1.8}$$

In Figure 1.9, we plot this mean radial distance versus time for 7 beam energies. From this observable, it appears that nuclear matter streams outward for all energies, unchecked. In fact, this is the case for very light fragments, many of which are emitted as a blast of pre-equilibrium light-charged-particles. If, however, we modify the observable slightly so as to focus on higher density regions (by analogy, larger fragments), the picture is quite different. We thus define a quadratic mean radial distance

$$\langle R_2 \rangle = \frac{\sum_{i,j,k} \rho^2(i,j,k) r(i,j,k)}{\sum_{i,j,k} \rho^2(i,j,k)} \tag{1.9}$$

and plot this versus time for the same beam energies (Figure 1.10). In this case, we can identify the expansion and subsequent collapse at low energies, stalling at intermediate energies, and continued growth at higher energies mentioned in the above quote. Furthermore, the stall in the expansion does not persist even 5 MeV/nucleon away from 60 MeV/nucleon.

The above quote, supplemented by the preceeding example, implies an energy dependance of this phenomenon, as do other authors[More92]. The sensitive dependence upon initial conditions (*e.g.* initial compression) coupled with a basic dependence upon parameters such as system size and the nuclear equation of state, lead us to classify the formation of non-compact geometries as a transitional phenomenon. The results of Chapter 4 will also confirm the transitional nature of this occurrence.

The precise process by which non-compact geometries, whether toroids or bubbles, are formed and decay is a matter of great interest, but is outside the scope of this

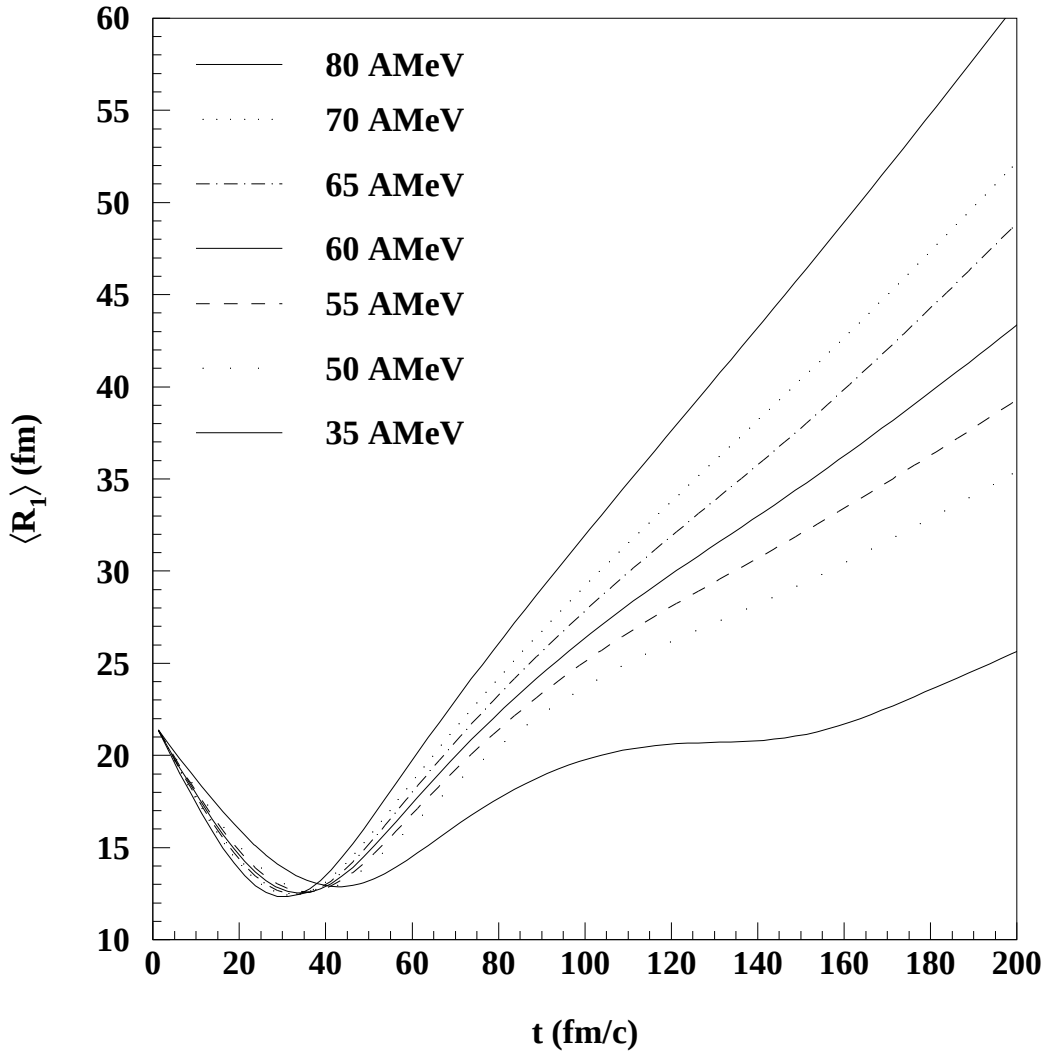

Figure 1.9: Mean distance from the CM-frame origin (Equation 1.8) in the BUU position lattice versus time for the ^{86}Kr+^{93}Nb system at 7 representative beam energies, as labelled.

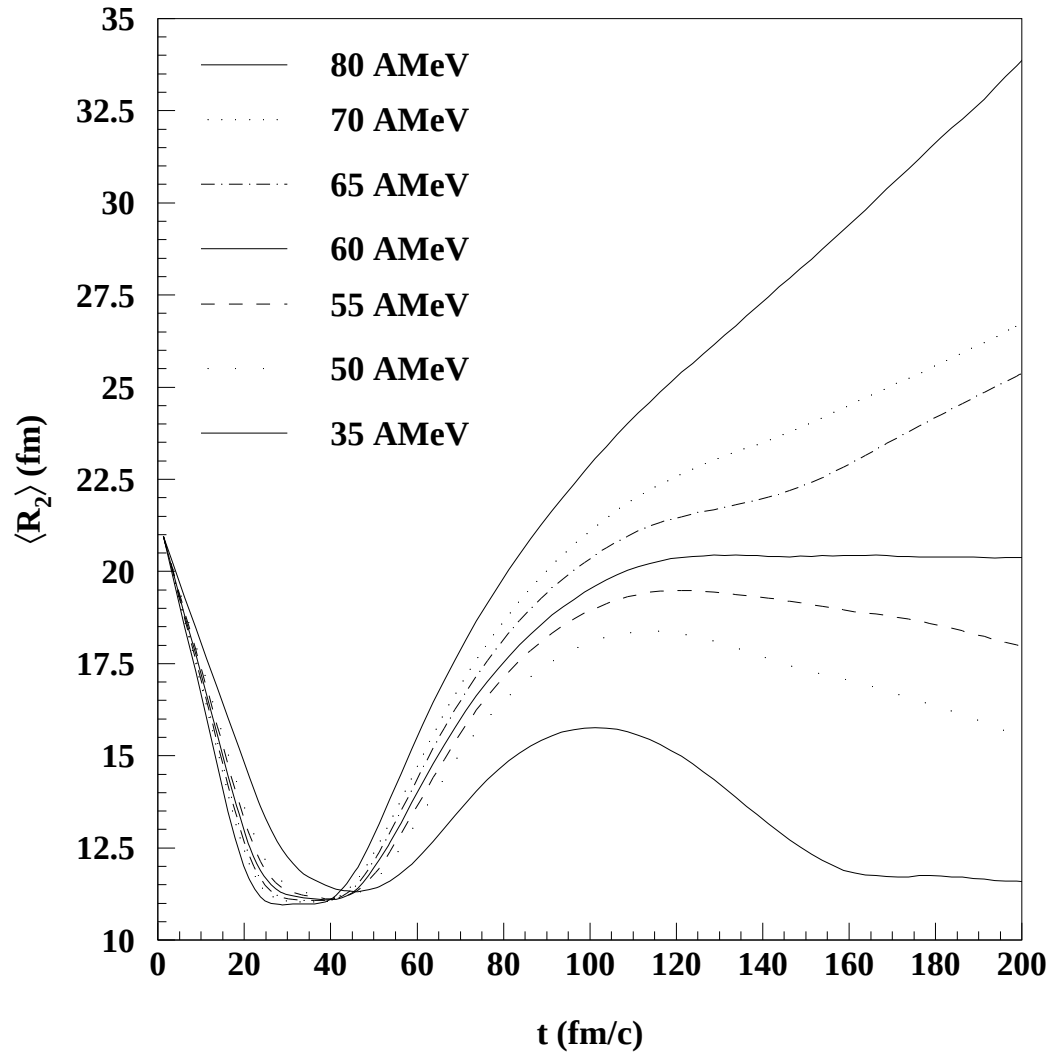

Figure 1.10: Same as Figure 1.9, except using quadratic normalization (Equation 1.9).

thesis. In Chapter 4, we will focus on experimental methods for determining whether or not these geometries are formed. Using two charge-based signatures, intermediate mass fragment multiplicities and power-law exponents of ordered charge distributions, we will establish that the system decays from a non-compact break-up geometry. With the use of event shape observables, we will then show that the decaying system is more coplanar in shape, thus implying that the geometry is toroidal. We find that the toroidal geometries are produced for beam energies between 60 and 75 MeV/nucleon.

Chapter 2

Experimental

2.1 The 4π Array

The 4π Array[West85, Cebr91, West93] is a close-packed detector array that has been operational for almost 10 years, and has yielded terabytes of data during that time. In shape, it is a truncated icosahedron, with 20 hexagonal and 12 pentagonal exterior faces, as shown in Figure 2.1. The 4π Array is an evolving system, so that it is necessary to delineate the components that were used to collect the data for this thesis. We shall describe the configuration first for the charge correlation analysis (Chapter 3), which was performed on an older data set, and then list the differences in the detector configuration used to collect the data for the non-compact geometries analysis (Chapter 4).

At the time of the charge correlation analysis, each of the hexagonal and pentagonal faces on the main ball, which excludes the entrance and exit pentagons, supported a module composed of several independent, layered detectors. One such hexagonal module is shown in Figure 2.2. Each hexagonal (pentagonal) ball module consists of 6 (5) truncated triangular phoswich detectors[West85] made from fast and slow scintillating plastic. These phoswich towers are preceeded by a Bragg Curve Counter (BCC), a single gas volume with a cathode window at the front and a conductive

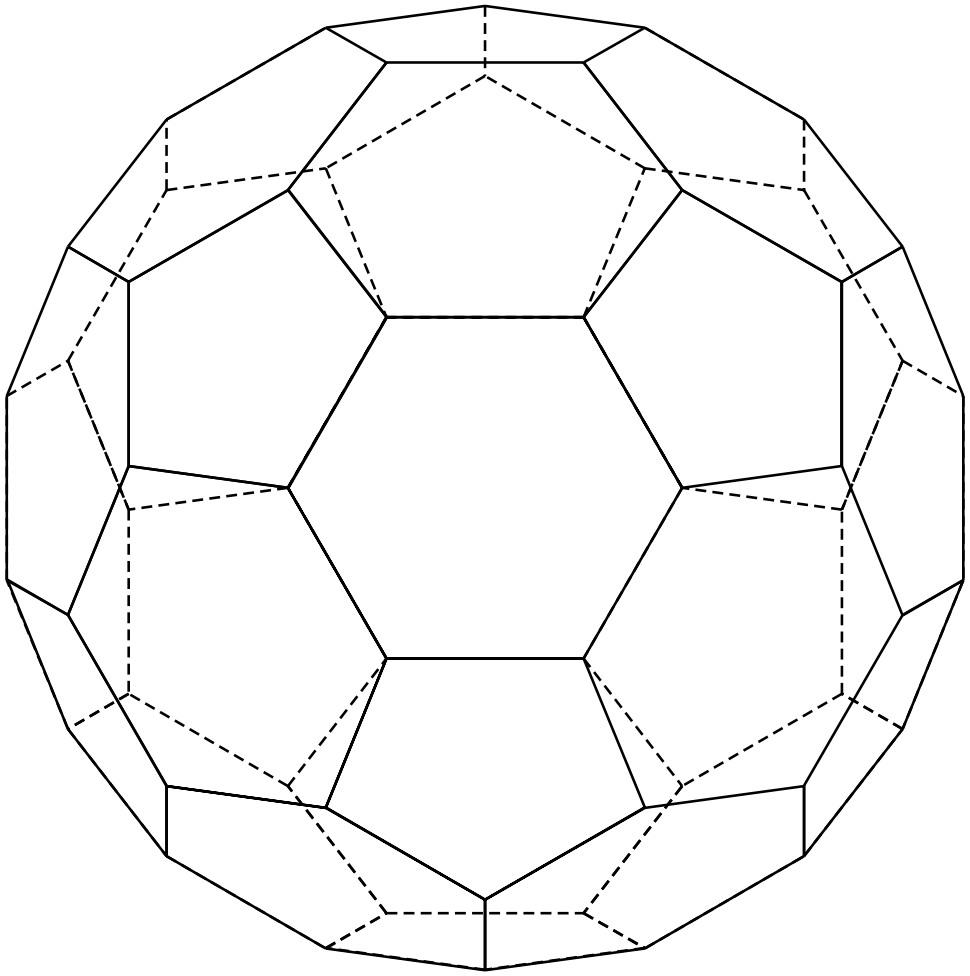

Figure 2.1: Mechanical drawing of the frame of the main 4π ball, revealing the arrangement of the hexagonal and pentagonal faces.

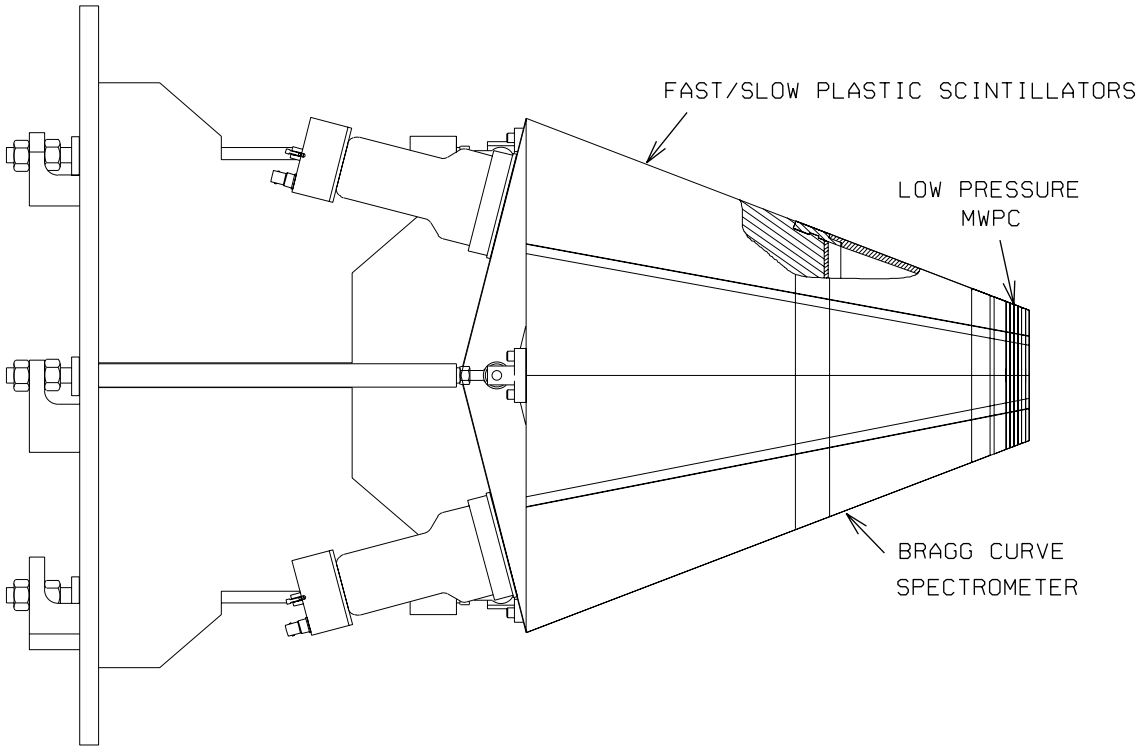

Figure 2.2: Side view of a hexagonal 4π ball module, revealing three independent layers of plastic and gas detectors.

coating which serves as an anode at the back; the anodes are evaporated onto the front of the thin fast plastic. The five forward hexagonal ball modules which surround the forward array pentagon have segmented anodes, providing a greater granularity in those modules while still using a single gas volume. Although low-pressure multi-wire proportional counters (MWPCs) are also shown in this figure, these were not instrumented at the time these data were collected. At a pressure of 125 Torr of C_2F_6, this BCC/Phoswich detector combination has a lower energy threshold of approximately 3 MeV/nucleon for ^{7}Li fragments.

The forward array consisted of 15 square and 30 cylindrical elements, a total of 45 fast and slow plastic phoswiches distributed evenly across the forward pentagon, covering roughly $5° < \theta < 18°$. (see Figure 2.3) Detectors in this array had a lower energy threshold of approximately 14 MeV/nucleon for ^{7}Li fragments. It was with this forward array and the phoswiches and BCCs of the main ball that the charge correlations data for Chapter 3 were taken. It is clear from this figure that there is uncovered solid angle in the forward direction ($0° < \theta < 18°$), a significant portion of the center-of-momentum frame solid angle. The improvements in detector coverage which took place between the charge correlation analysis and the non-compact geometries analysis all took place within this forward pentagon, in order to improve the forward coverage.

The first major upgrade was the addition of the High Rate Array [Pak92, Pak93, Pak96], shown in Figure 2.4. It consisted of 45 close-packed fast and slow plastic phoswich telescopes which covered the lab polar angles $3° < \theta < 18°$, thus replacing the forward array shown in in Figure 2.3. It was built at the NSCL, where the project was led by Robert Pak. Detectors in this array had a lower energy threshold of approximately 14 MeV/nucleon for ^{7}Li fragments.

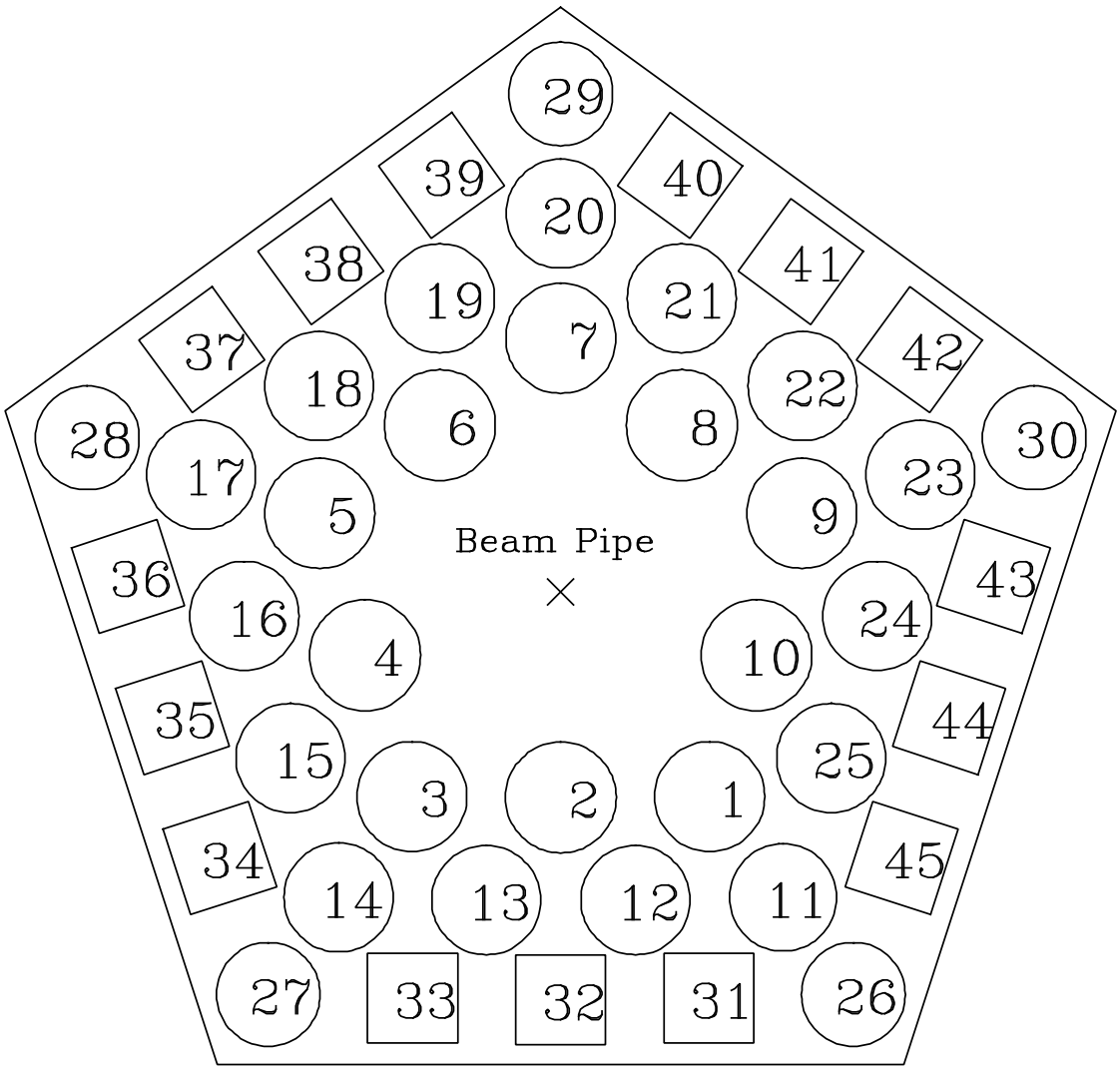

Figure 2.3: Arrangement of the forward array phoswiches at the time of data collection for the charge correlations analysis.

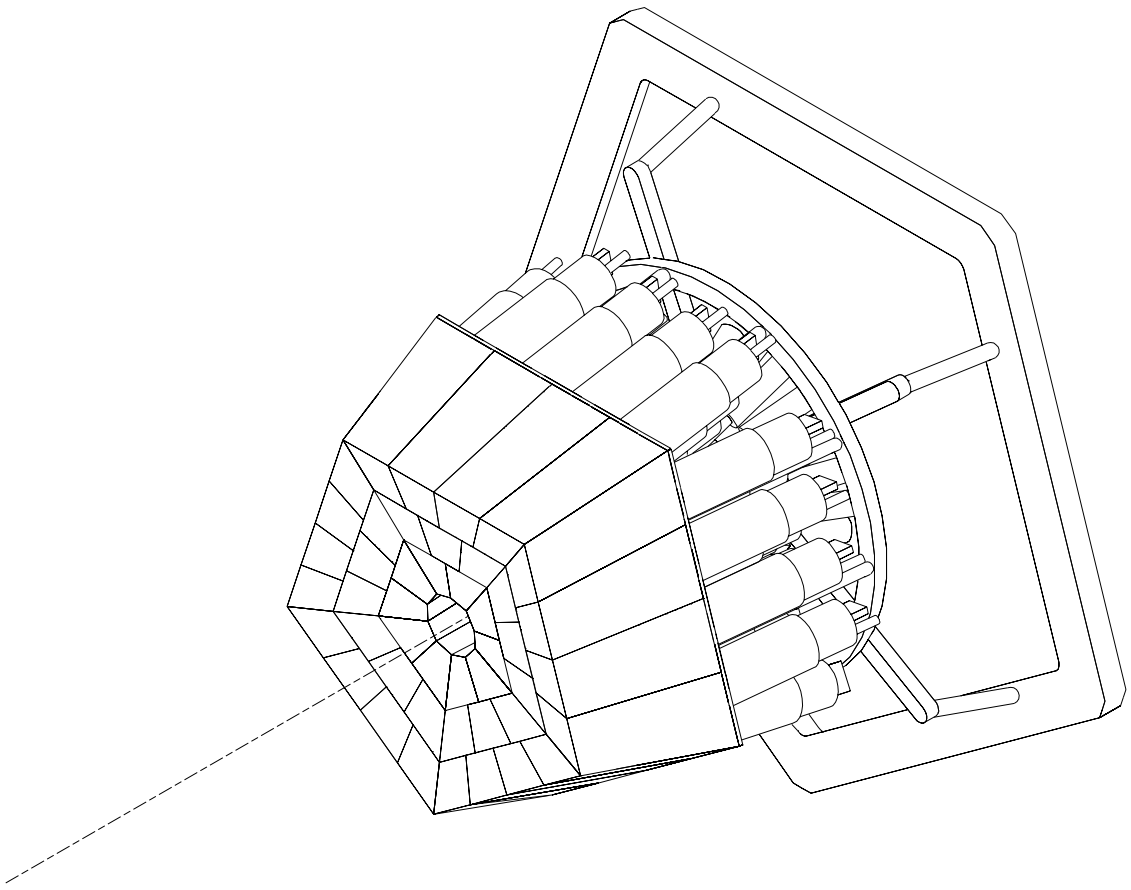

Figure 2.4: The High Rate Array, which consists of 45 close-packed phoswich telescopes.

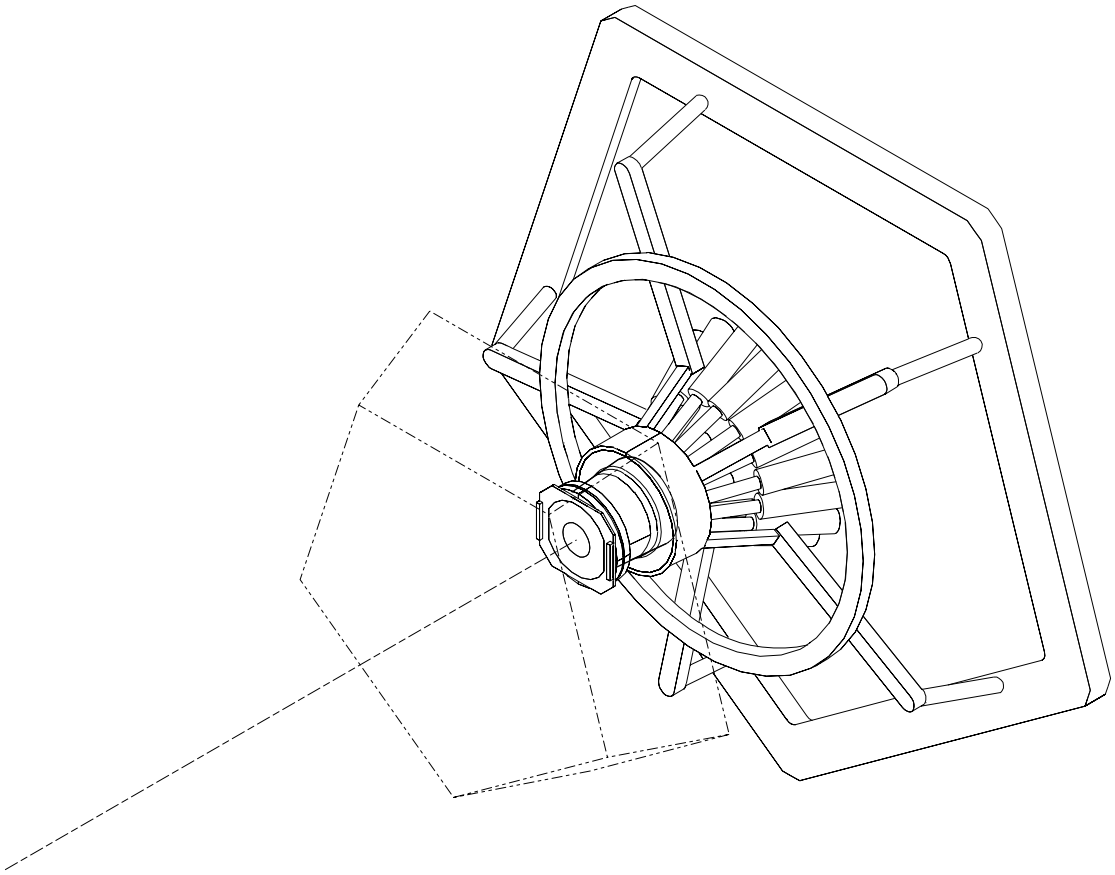

Figure 2.5: The Maryland Forward Array, with the outline of the High Rate Array to show positioning.

The second upgrade was the addition of the Maryland Forward Array[Llop92], shown in Figure 2.5. This array consisted of 16 fast and slow plastic phoswiches, preceeded by a multi-segmented annular silicon detector. It covered the angles $1.5° < \theta < 3°$, and was built by Bicron Corporation at the request of collaborators in the University of Maryland Department of Chemistry. The Maryland Forward Array is positioned inside the High Rate Array, as indicated in Figure 2.5. Detectors in this array had a lower energy threshold of approximately 10 MeV/nucleon for ^{7}Li fragments.

2.2 The Zero Degree Detector

Following these upgrades, another detector now called the Zero Degree Detector (ZDD) was added[Ston93, Ston94]. Such a detector was proposed both to further improve forward solid angle coverage and to enhance existing methods of experimental determination of the impact parameter of detected events. Simulations were performed in which the impact parameter was related to observable quantities derived from fragments detected within the remaining forward solid angle ($0° < \theta < 1.5°$).

2.2.1 Design

Once the need for the ZDD was established, we performed a series of calculations in order to optimize the exact configuration of the detector. Although typical rates for event-by-event fragment population in this detector can be obtained from detailed simulations, the greatest rate limitations arise from the scattering of non-interacting beam particles into the detector; such scattering rates can be calculated directly from the Rutherford scattering equation. One other factor contributing to this direct-beam rate is the divergence of the beam itself, measured in terms of beam emittance. The beam emittance is the product of the size of the beam spot and the resulting angular divergence of the beam, with an additional constant factor of π. It has been empirically measured to be as high as 5π (10π) mm·mr in the x (y) direction. Given a 1 mm beam spot in the 4π experimental vault (worst case), the divergence of the beam was estimated to be 10 mr (0.6°). Based on the typical beam currents used in previous 4π experiments, divergence of beam particles, and the typical fragment particle population in this detector, the total count rate was projected to reach as high as one million particles per second, with eight-fold segmentation and a small hole in the center, to minimize hits from non-interacting beam particles. With such high

rates projected, a concerted effort was mandated to facilitate high speed processing of the signals emitted from both the ΔE and E scintillating plastic layers. This effort resulted in the following detector and signal processing features:

1. Fast scintillating plastic for both ΔE and E layers
2. Separated read-out of both layers
3. Adiabatic light-guides for the ΔE readout
4. High-Speed Photo-Multiplier Tubes (PMTs)
5. Negative High Voltage bias for the PMT
6. Specialized high-power voltage dividers to drive the PMTs

First, the ZDD could not be made from fast and slow scintillating plastic, as is the majority of the 4π array. Typical slow plastic light emission times are on the order of hundreds of nanoseconds. Both the ΔE and E layers were made of equally fast scintillating plastic (NE 104, τ = 1.9 nS) to avoid the overlap of light signals from separate events. Second, once the choice is made to use ΔE and E layers with equally fast plastic, the signals can not be resolved if they are read out through the same PMT, as is done with a phoswich. Thus each layer was given a dedicated PMT, resulting in 16 PMTs for the eight-fold segmented array. Third, the light emitted from the ΔE plastic must be collected from its edge, requiring adiabatic light-guides to couple the thin plastic to the PMTs. Fourth, fast PMTs (XP2262B) were chosen for optimal signal transit time (31 nS) and minimal time spread (3.5 nS). Fifth, the PMTs were operated in the negative HV bias mode to avoid the capacitive coupling inherent in positive HV bias designs. And finally, we designed, prototyped, and constructed specialized high-voltage dividers for these PMTs to allow processing of

near 1 volt output signals at a rate of up to 500 kHz. The design goal of 1MHz processing was deemed infeasible given the findings of the prototype testing. The final circuit designs for both the high voltage dividers and the PMT sockets used are shown in Figure 2.6. Corresponding lists of components are tabulated in Appendix A.

We then chose the optimal thickness of the ΔE and E layers of the detector. Of primary consideration were the transmission of heavy fragments, signal-to-noise ratio in the ΔE layer, and the stopping power of the E layer. We have calculated the fractional energy loss in a 0.67 mm thick scintillating plastic layer and plotted that versus the incident energy per nucleon for all fragments with $2 \leq Z \leq 27$, the charges successfully resolved in experimental conditions, in Figure 2.7. From this figure, the "punch-in" energies, those at which the particle is no longer stopped in the ΔE layer, can be clearly seen. At this thickness, all fragments of interest having an incident energy of roughly 25 MeV/nucleon or more are transmitted to the E layer, and can be identified via ΔE vs. E techniques. The actual lower energy thresholds are listed in table 2.1. Similar calculations were performed which showed that a 30.0 cm plastic layer would stop all particles with incident energies (KE/A) $<$ 220 MeV.

The final assembly design of the ZDD is shown in Figure 2.8. From this figure, all of the relevant mechanical design features can be seen: the eight-fold segmentation, the small hole in the center, the separated readout of ΔE and E layers, and the light-guides used to collect the light from the thin ΔE layers.

A dedicated chamber was also designed for the ZDD, since there was insufficient space for an additional detector in the existing 4π ball. This chamber was given the added feature that the ZDD could be moved inside the chamber without breaking vacuum, through the use of a goniometer. This was deemed necessary due to the

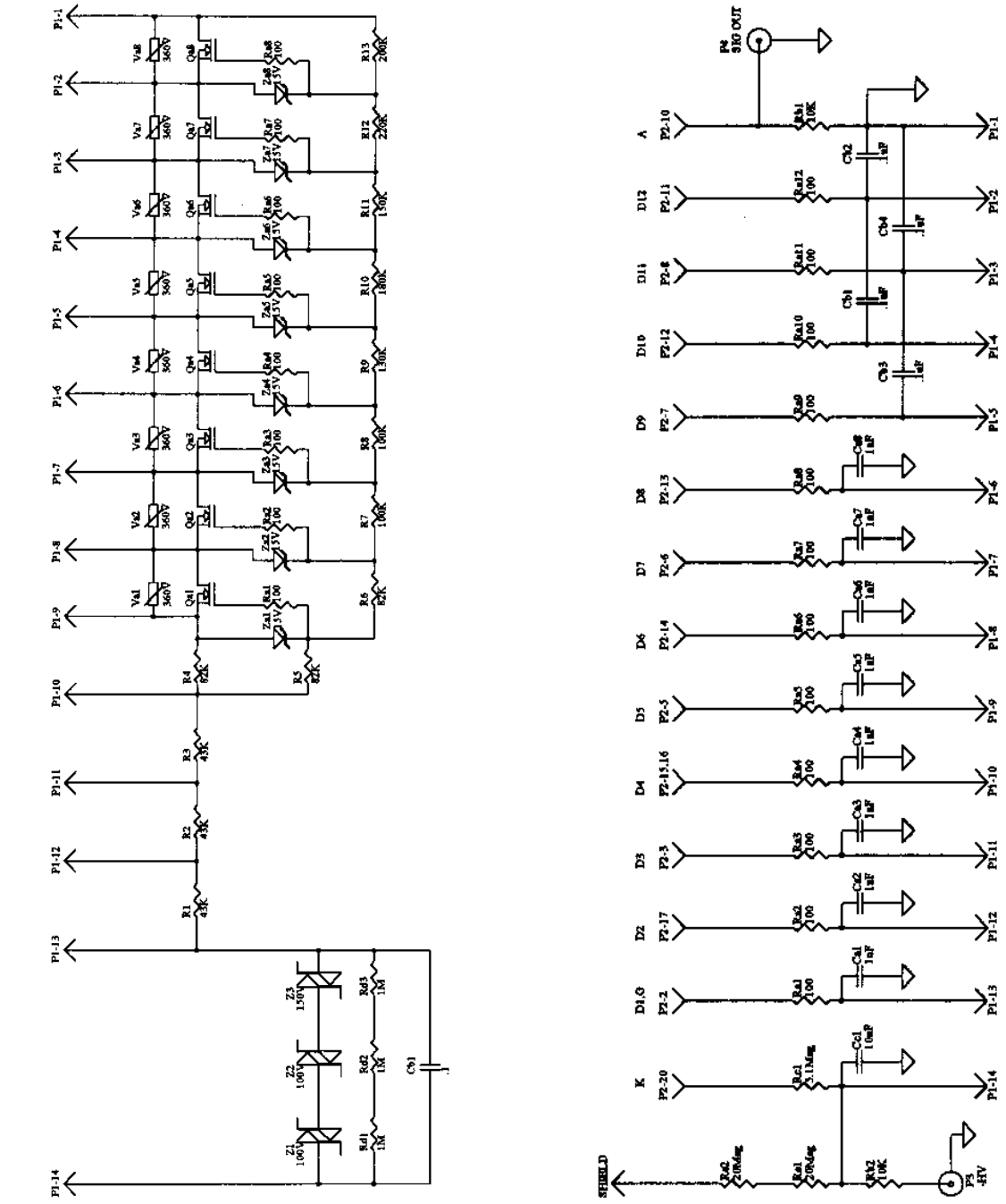

(a) (b)

Figure 2.6: ZDD High Voltage Circuits. (a) HV divider card. (b) PMT socket card.

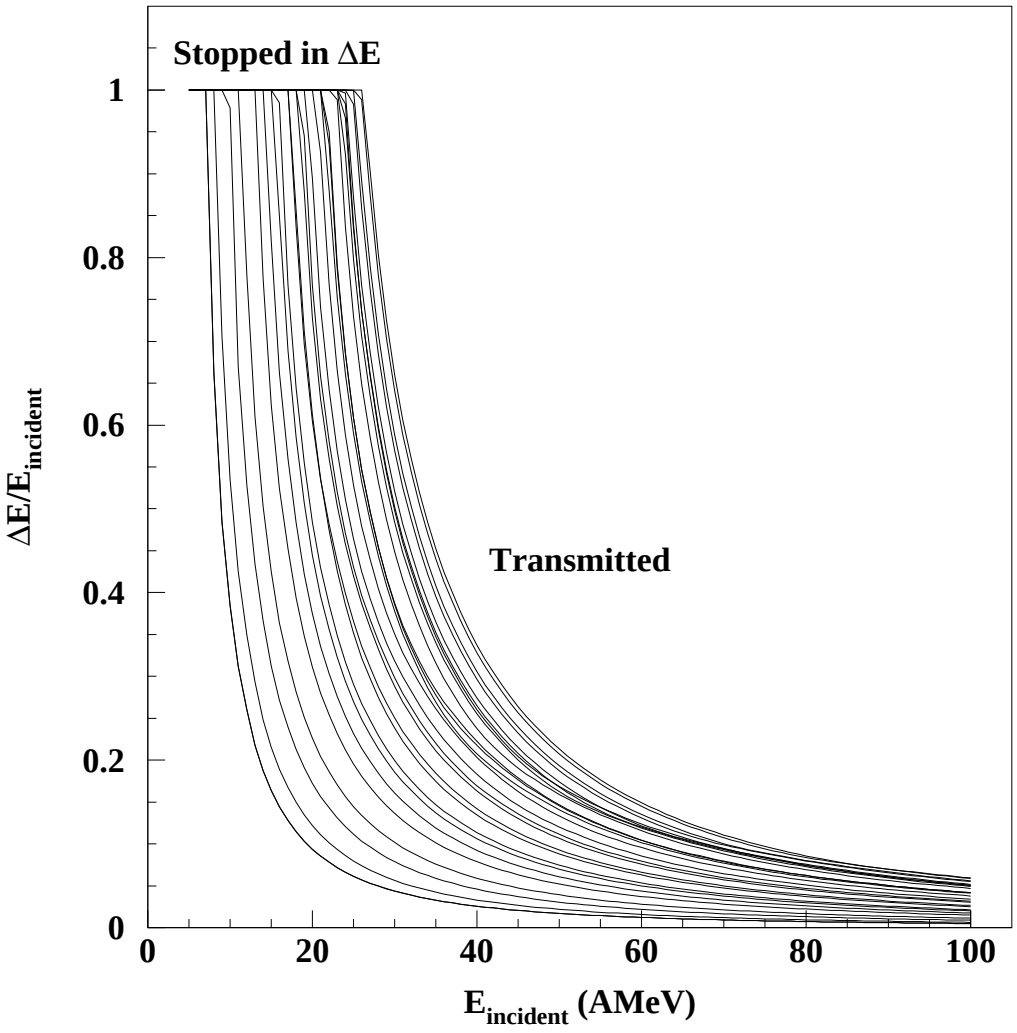

Figure 2.7: The fractional energy loss of fragments ($2 \leq Z \leq 27$) in 0.67 mm scintillating plastic, revealing the "punch-in" energies.

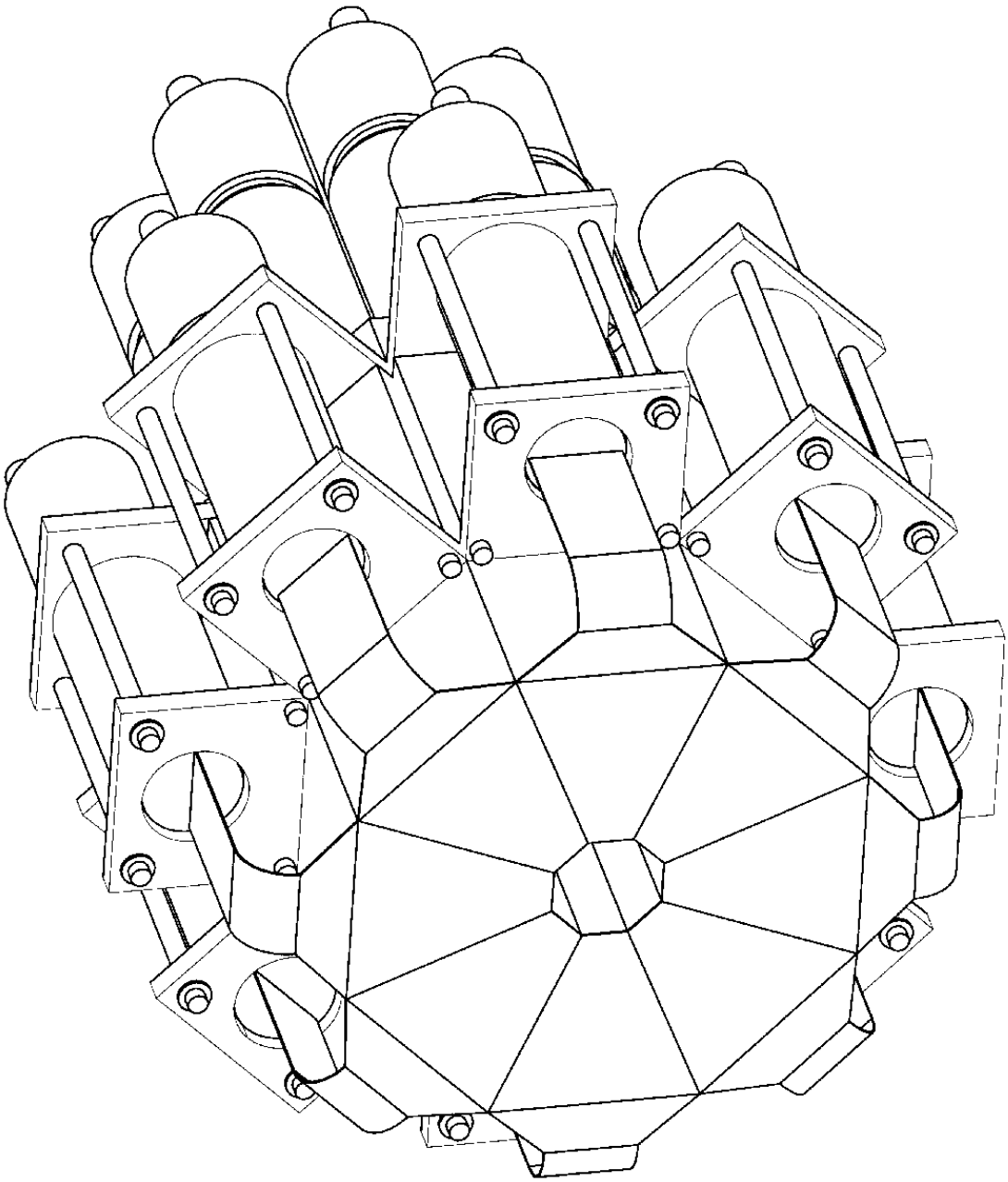

Figure 2.8: Assembly diagram of the ZDD, showing location of PMTs and light guides. The beam enters from the lower right.

Z	Punchin energy (MeV) / (AMeV)	Z	Punchin energy (MeV) / (AMeV)	Z	Punchin energy (MeV) / (AMeV)
1 (p)	7.2 / 7.2	13	504 / 18.7	25	1375 / 25.0
2	29.5 / 7.4	14	555 / 19.8	26	1450 / 25.9
3	57.5 / 8.2	15	625 / 20.2	27	1535 / 26.0
4	90 / 10.0	16	685 / 21.4	28	1590 / 27.4
5	119 / 11.8	17	756 / 21.6	29	1695 / 26.9
6	158 / 13.2	18	845 / 21.1	30	1770 / 27.6
7	201 / 14.4	19	895 / 22.9	31	1880 / 27.2
8	248 / 15.5	20	952 / 23.8	32	1995 / 27.0
9	304 / 16.0	21	1055 / 23.4	33	2075 / 27.7
10	347 / 17.3	22	1135 / 23.6	34	2190 / 27.4
11	396 / 17.2	23	1220 / 23.9	35	2250 / 28.5
12	440 / 18.3	24	1290 / 24.8	36	2360 / 28.1

Table 2.1: Punchin energies for the ZDD, based on 0.67mm thick scintillating plastic.

potential misalignment of the incident beam, which could strike an individual detector with a rate surpassing its maximum count rate. The mechanical drawing of this chamber is shown in Figure 2.9. By placing this chamber sufficiently far from the target, time-of-flight (TOF) measurements could also be made, allowing the identification of particles which stop in the ΔE layer. Given the space constraints of the 4π experimental vault, the maximum separation between the ZDD and the target was 2.74 m. We performed additional TOF calculations for particles with a range of incident energies (5 - 100 MeV/nucleon) and plotted the energy deposited in the ΔE layer versus the time of flight for all particles $2 \leq Z \leq 27$ in Figure 2.10. From this figure, we extract the difference in time-of-flight for particles that leave the same energy in the ΔE plastic, between 1 and 3 nS. This small time difference provided further incentive to choose high-speed plastics and PMTs. A calibration of the TOF response of the ZDD is not included in the data shown in the chapters which follow. However, this feature is available for future use.

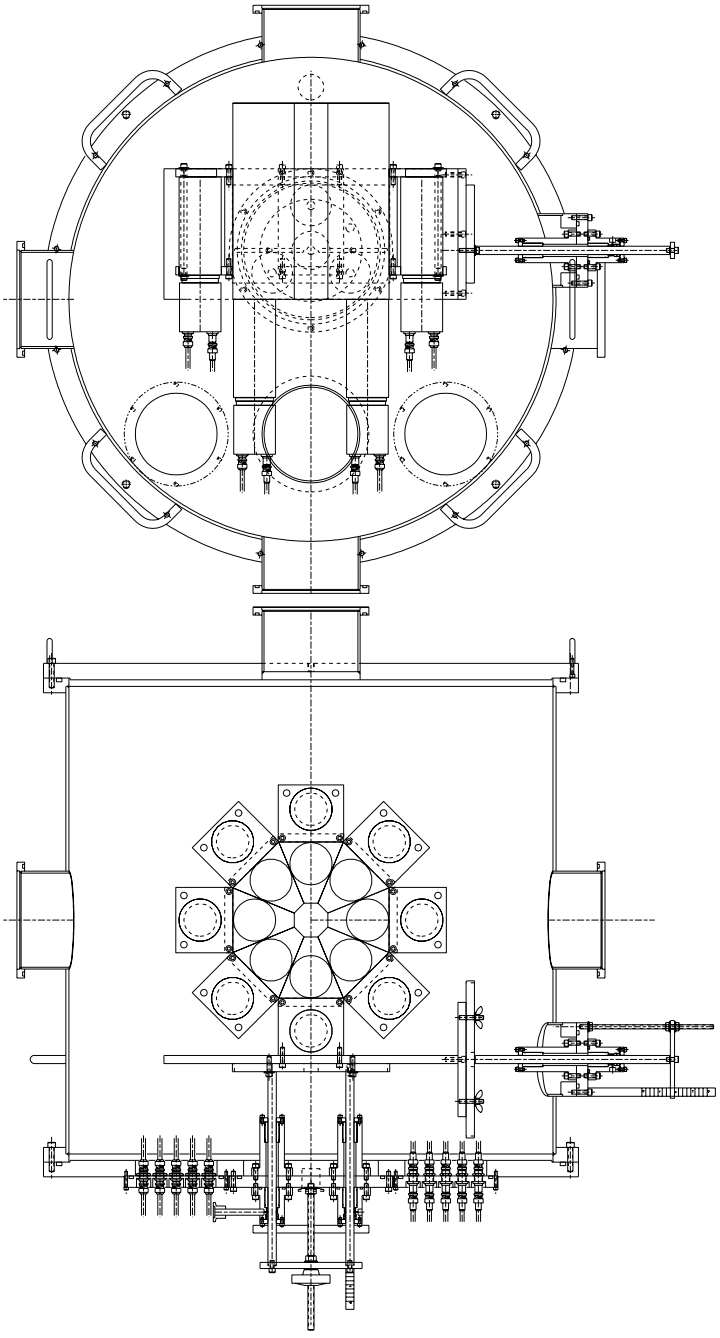

Figure 2.9: Mechanical drawing of the ZDD chamber. Above: Top view, with beam entering from the top of the page. Below: Rear view, looking upstream. This also shows the goniometer, used for positioning of the detector.

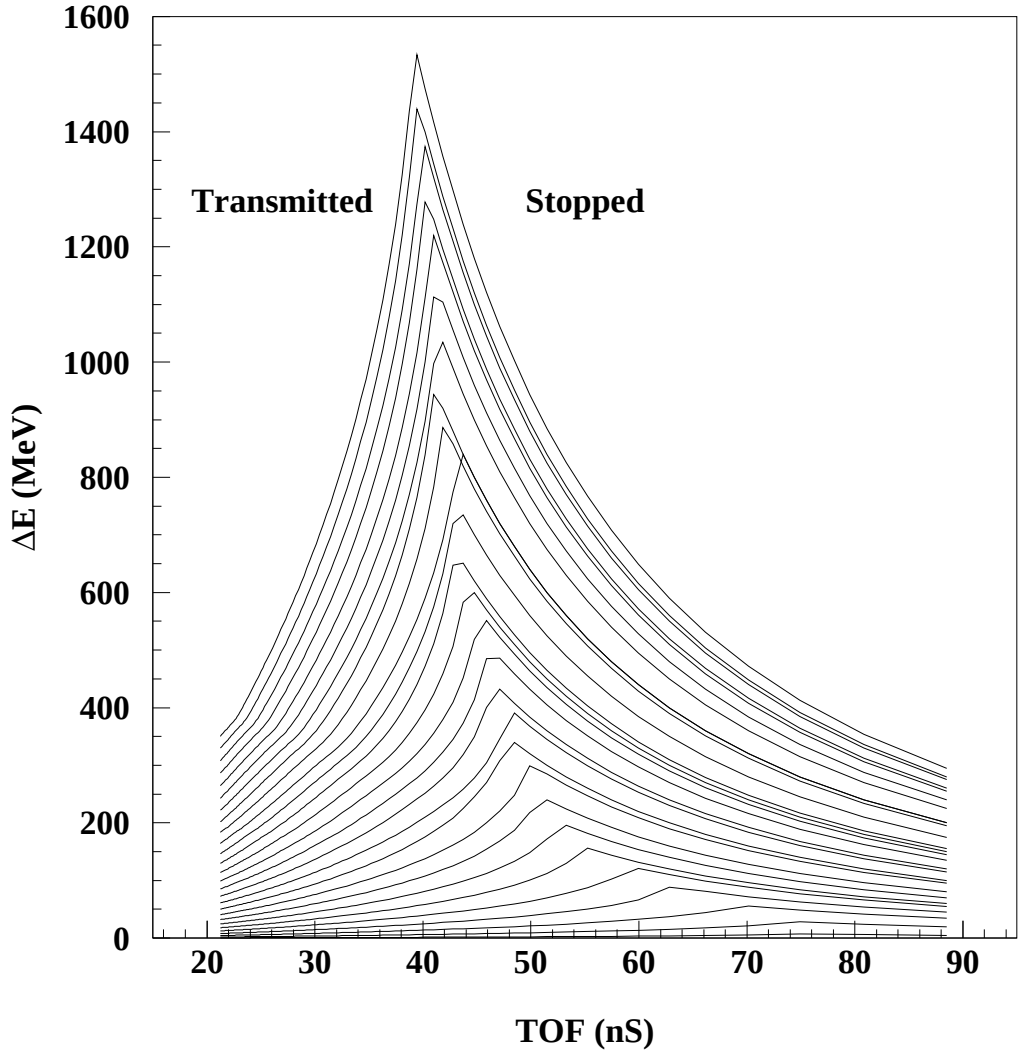

Figure 2.10: Energy deposited in the ΔE plastic versus time-of-flight for fragments (Z=2-27) in 0.67 mm scintillating plastic, for a 2.74 m flight path.

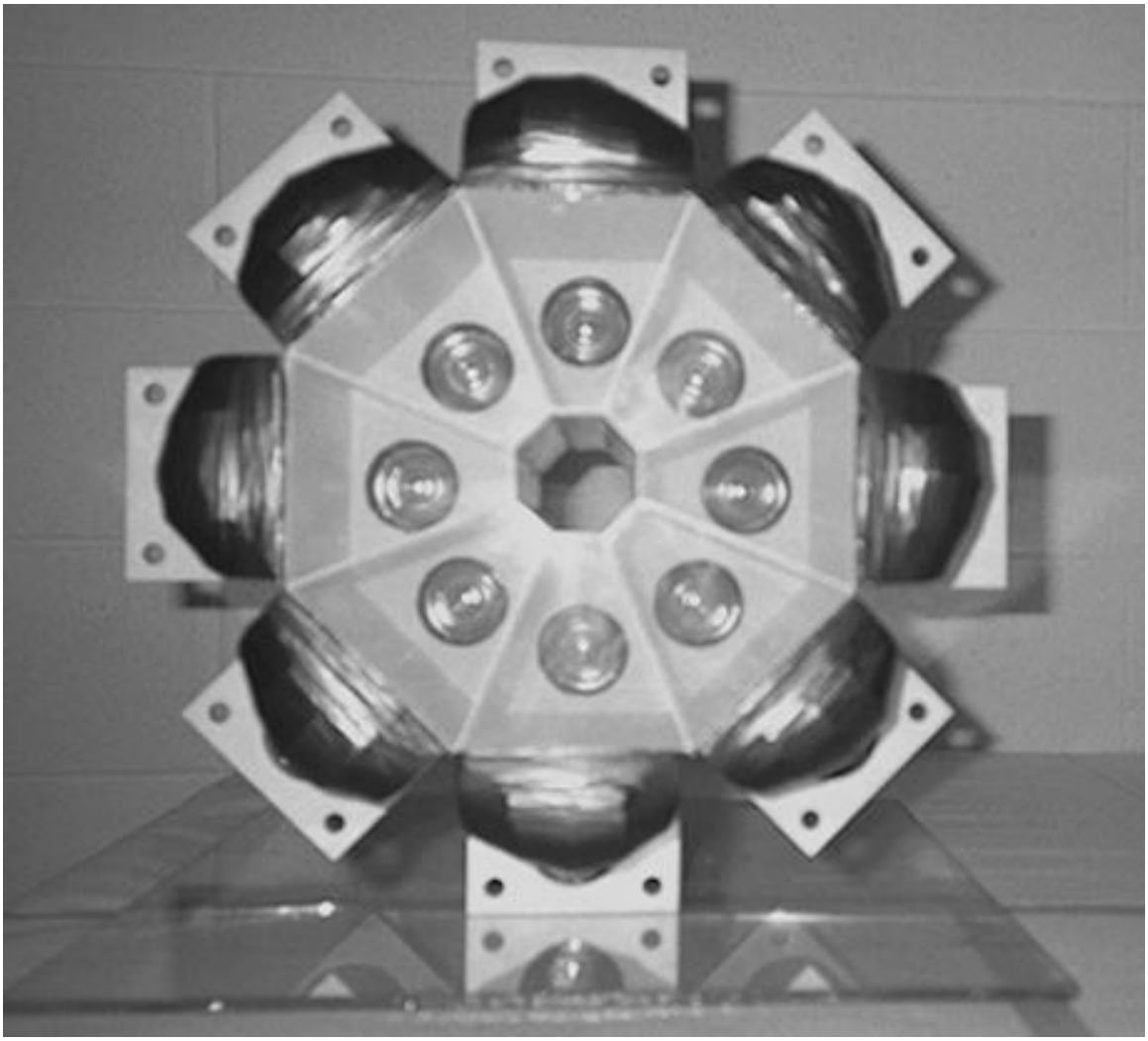

Figure 2.11: Frontal photograph of the Zero Degree Detector.

2.2.2 Construction

The Zero Degree Detector was built at the NSCL, where the project was led by Nathan Stone. It was built according to the specifications described in Section 2.2.1. Construction was completed in November 1994, and the ZDD has been used in many experiments since that time. Figure 2.11 is a photograph of the ZDD as it appeared before the evaporation of aluminum onto the face of the E plastic layers for optical decoupling.

After its installation into the ZDD chamber, it was precisely aligned to the cham-

Detector	ϕ	Detector	ϕ
1	338.3	5	158.3
2	293.3	6	113.3
3	248.3	7	68.3
4	203.3	8	23.3

Table 2.2: Azimuthal angles for the ZDD. (Note: Since the ZDD chamber is separate from the 4π ball, if the ball is rotated, these angles will change accordingly. These angles are reported assuming a 3.7° tilt (clockwise, looking down the beampipe) of the 4π ball.)

ber, and the relative orientations of the 4π ball and ZDD chamber were measured. The geometric centers of each telescope were also measured. Each ZDD telescope has its geometric center at a laboratory polar angle of 1.1° , and the azimuthal angles are listed in Table 2.2 (relative to the conventional azimuthal origin of the 4π ball).

2.2.3 Detector Response

Following the installation of the ZDD, we performed a calibration in which we bombarded a 1 mg/cm^2 ^{93}Nb target with a ^{87}Kr beam with incident energies ranging from 35 to 95 MeV/nucleon. The ZDD performed well for this experiment, providing spectra with charge resolution up to Z=27. We plot the measured light output spectrum (ΔL versus L) in Figure 2.12. From this spectrum the qualitative response of the detector (*i.e.* energy resolution, ΔL versus L line shape, and detected charges) can be seen. To extract quantitative information from these ΔL/L spectra regarding the actual energies of fragments, we performed a detailed energy calibration for the ZDD.

We derive the light response equation by beginning with the basic relation between specific energy loss and light production, as reported in a study on the performance

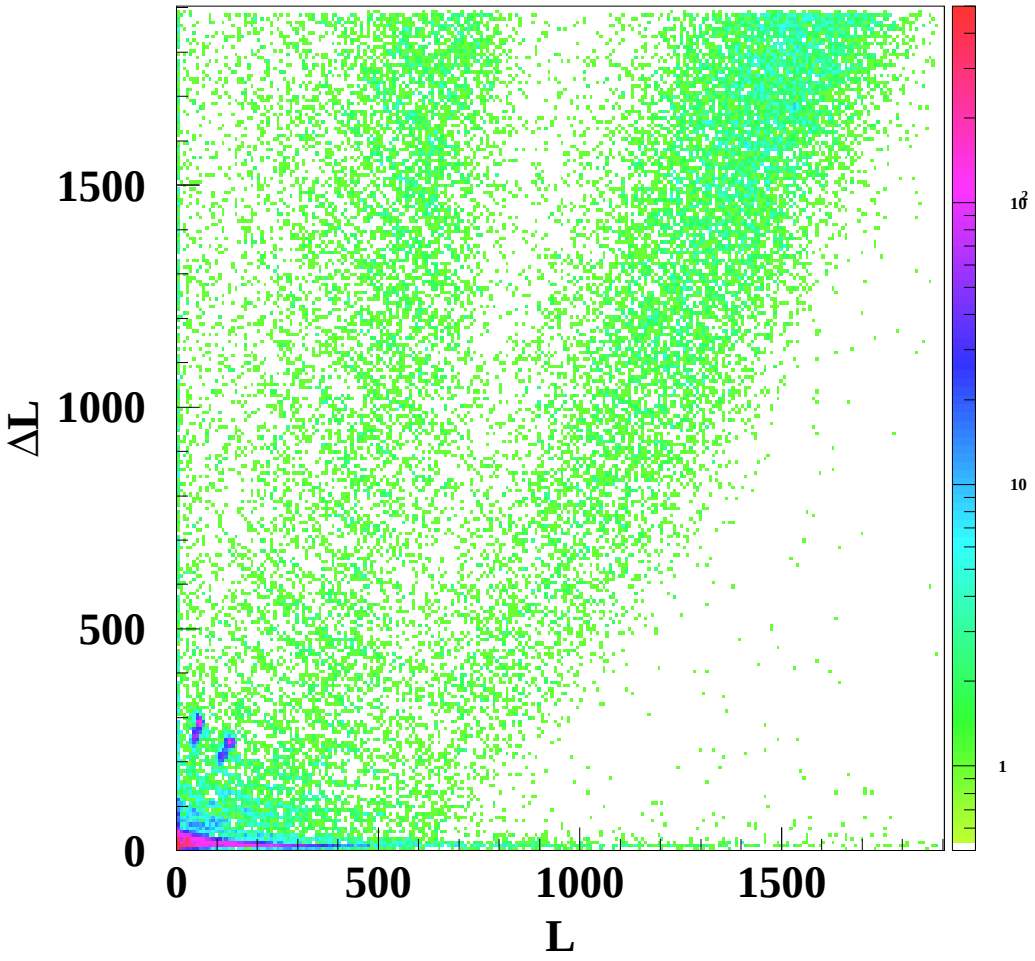

Figure 2.12: Raw experimental data recorded in one ZDD telescope for 45 and 65 MeV/nucleon ^{87}Kr incident on ^{93}Nb.

of phoswich detector performance:[Past83]

$$\frac{dL}{dx} = \frac{-S\left|\frac{dE}{dx}\right|}{1 + kB\left|\frac{dE}{dx}\right|}$$

where S is the absolute scintillation efficiency, k the quenching parameter, and B a constant relating density of ionized and excited molecules to dE/dx. We can then substitute the formula for specific energy loss, as reported by Birks in his text on scintillation detectors:[Birk64]

$$\frac{dE}{dx} = \frac{4\pi e^4 Z^2}{m_e v^2} N_D Z_D \left[\ln\left(\frac{2m_e v^2}{I}\right) - \ln\left(1-\beta^2\right) - \beta^2\right]$$

where Z is the atomic number of the incident particle, and N_D and Z_D are the density and atomic number of the atoms in the detecting medium. Now, if we let $\beta \ll 1$ then we can substitute $v^2 = \frac{2E}{m_n A}$. We also make the following assignments:

$$\alpha = 2\pi e^2 N_D Z_D \frac{m_n}{m_e}$$

$$C = kB\alpha A Z^2 \ln\left(\frac{\beta E}{A}\right)$$

If we make the additional assumption that the term $\ln\left(\frac{\beta E}{A}\right)$ is slowly varying in the range of interest, then we can write the differential light output as

$$\frac{dL}{dE} = \frac{-S}{1 + \frac{C}{E}}$$

This relation can be integrated directly between the incident (E_0) and punch-out (E_1) energies, yielding the total light output for a given medium

$$\Delta L = S\left[\Delta E - C\ln\left(\frac{C+E_0}{C+E_1}\right)\right]$$

It can be shown that the constant kB itself has an approximately inverse relationship to Z, and that the logarithm which was previously assumed to be constant (or

slowly varying) has a slight Z and A dependance as well. So we make the following replacement:

$$C = \gamma A^a Z^z$$

in which γ is a constant, and a and z are the strengths of the A and Z dependencies contained in the constant C. The final response equations between ΔL, L, ΔE, and E are thus

$$\Delta L = S\left[\Delta E - C_{dl}\ln\left(\frac{C_{dl}+(\Delta E+E)}{C_{dl}+E}\right)\right] \tag{2.1}$$

and

$$\mathrm{L} = S\left[E - C_l \ln\left(1+\frac{E}{C_l}\right)\right] \tag{2.2}$$

where $C_x = \gamma A^a Z^z$ (x = dl,l) and ΔL, L, ΔE, and E, in these last two equations now represent the light and energy loss in the transmission and stopping media, respectively.

These relations can be approximated by the two following equations:[Cebr92]

$$\Delta L = G_{dl}\Delta E^{e_{dl}} Z^{z_{dl}} A^{a_{dl}} \tag{2.3}$$

and

$$L = G_l E^{e_l} Z^{z_l} A^{a_l} \tag{2.4}$$

where G_x (x = dl,l) is a simple gain factor, and e_x, z_x, and a_x are the strengths of the ΔE (or E), Z and A dependencies, respectively.

To determine which of these two sets of functions best reproduces the actual light response of the ZDD, we measured a set of calibration points, each of known energy and isotopic identity, and compared the calculated light output from each of these relations to the measured light output, adjusting the free parameters with a χ^2 minimization routine. The calibration points were drawn from three sources: a secondary fragmentation beam from the NSCL A1200 reaction particle spectrometer, ΔE energy values extracted from punchin points on the raw spectra, and 95 MeV/nucleon

points also extracted from the raw spectra. The raw calibration points from the fragmentation beam are shown in Figure 2.13. The isotopic identity of the points were identified by locating the ^{8}Be vacancy, since ^{8}Be is particle unstable. One atomic number (Z=17) and isotope ratio (N=Z) have been labelled, for clarity.

The ΔL and L values of each of the calibration points drawn from the sources described above can be calculated from the known ΔE, E, Z, and A values in each case via the response equations (Equations 2.1-2.4) derived above. A minimization was performed for each of these equations to determine the parameters that best match the data. Below are the final equations (with calculated parameters) which best fit the data in each case, which compare favorably with our previous work and standard parameterizations.

Cebra:

$$\Delta L = 0.880 \Delta E^{0.519} Z^{0.279} A^{0.488} \tag{2.5}$$

$$L = 0.243 E^{1.118} Z^{0.105} A^{-0.596} \tag{2.6}$$

Birks:

$$\Delta L = 0.959 \left[\Delta E - C_{dl} \ln \left(\frac{C_{dl} + (\Delta E + E)}{C_{dl} + E} \right) \right] \tag{2.7}$$

where

$$C_{dl} = 6.679 A^{0.0} Z^{1.444}$$

and

$$\mathrm{L} = 0.281 \left[E - C_l \ln \left(1 + \frac{E}{C_l} \right) \right] \tag{2.8}$$

where

$$C_l = 13.563 A^{0.0} Z^{1.559}$$

We have plotted the measured values of ΔL (panels a and b) and L (panels c and d) versus the calculated values from both the Cebra (panels a and c) and Birks

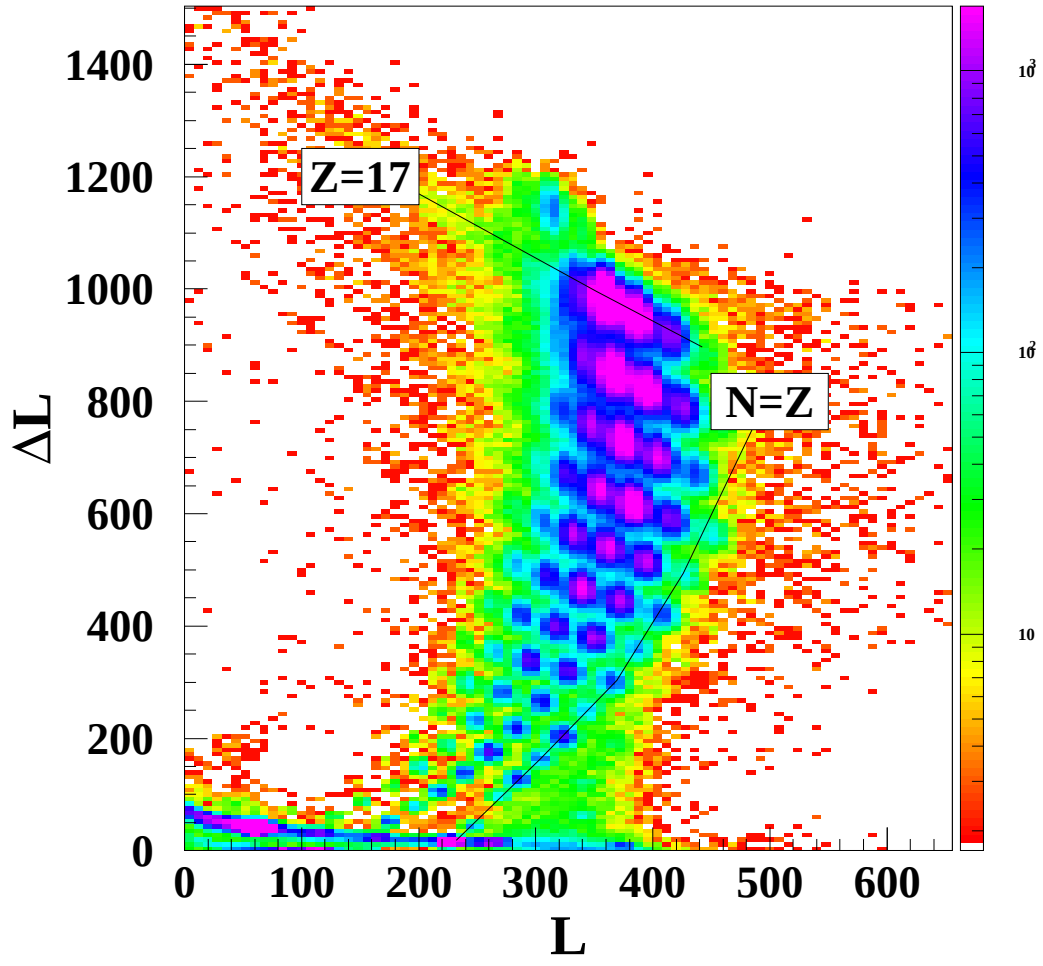

Figure 2.13: Calibration points measured in segment 2 of the ZDD. One atomic number (Z=17) and isotope ratio (N=Z) are labelled.

(panels b and d) parameterizations, in Figure 2.14. Because, in the case of a perfect fit, these lines should be straight lines with slope equal to 1.0, any deviation from a straight line is an indication of an imperfection in the fit. Thus, one can gain a qualitative measure of the fit from the line shape. In addition, the χ^2 per degree of freedom values are written on each panel as well. From a visual inspection of the fits, it appears that the Cebra parameterization yields a better fit to the data, and the χ^2 values are less than half those found with the Birks parameterization. For this reason, the Cebra parameterization was used in the final calibration of the detector.

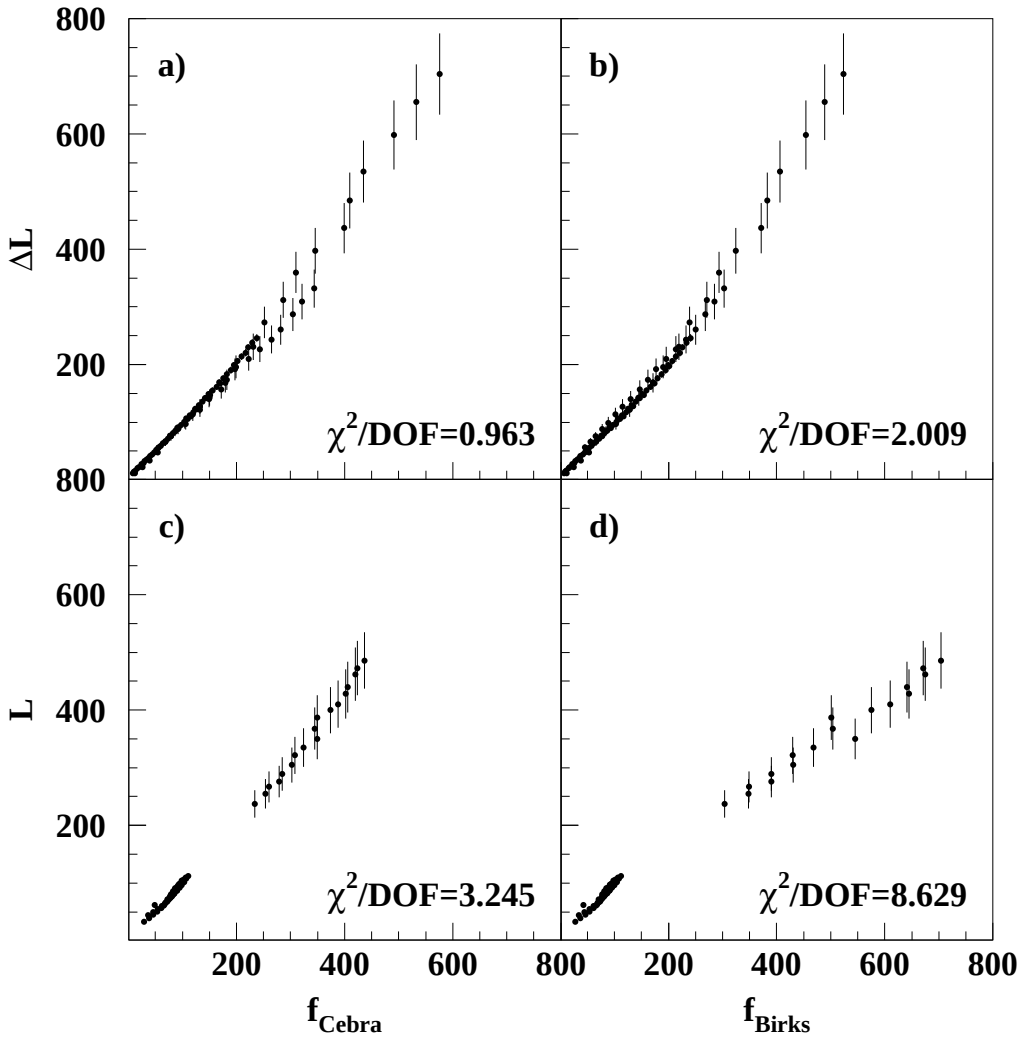

Figure 2.14: Response function minimization results, comparing Cebra and Birks parameterizations. (a) ΔL Measured vs. Calculated from Cebra parameterization. (b) ΔL Measured vs. Calculated from Birks parameterization. (c) L Measured vs. Calculated from Cebra parameterization. (d) L Measured vs. Calculated from Birks parameterization.

Chapter 3

Transitions in Decay Mechanism

3.1 Dalitz Triangles

In this chapter, we concentrate on quantitative information extracted from one type of charge correlation called the charge-Dalitz plot[Kreu93, Biza93, Rous93]. To construct a Dalitz plot, we use only the charges of the three largest fragments in an event ($Z_1 > Z_2 > Z_3 > \cdots$). We normalize these charges by dividing by their sum ($Z_i' = Z_i / \sum_{j=1,3} Z_j$). A Dalitz plot is then created by setting these three reduced charges equal to the distances to the three sides of an equilateral triangle of unit altitude (see Figure 3.1). This method uniquely defines one pair of coordinates for each event, given by the following equations:

$$x = Z_i' \tan(30°) + \frac{Z_j'}{\cos(30°)}$$

and

$$y = Z_i'$$

where the indices (i,j) are non-duplicating pairs of 1, 2, and 3 (*e.g.* 1,2 ; 2,3 ; 1,3 ; 2,1 ; $\cdots$). This latter definition brings to light the fact that a Dalitz triangle in fact contains 6 symmetrized copies of one unique triangle, outlined in Figure 3.1 with the dashed line.

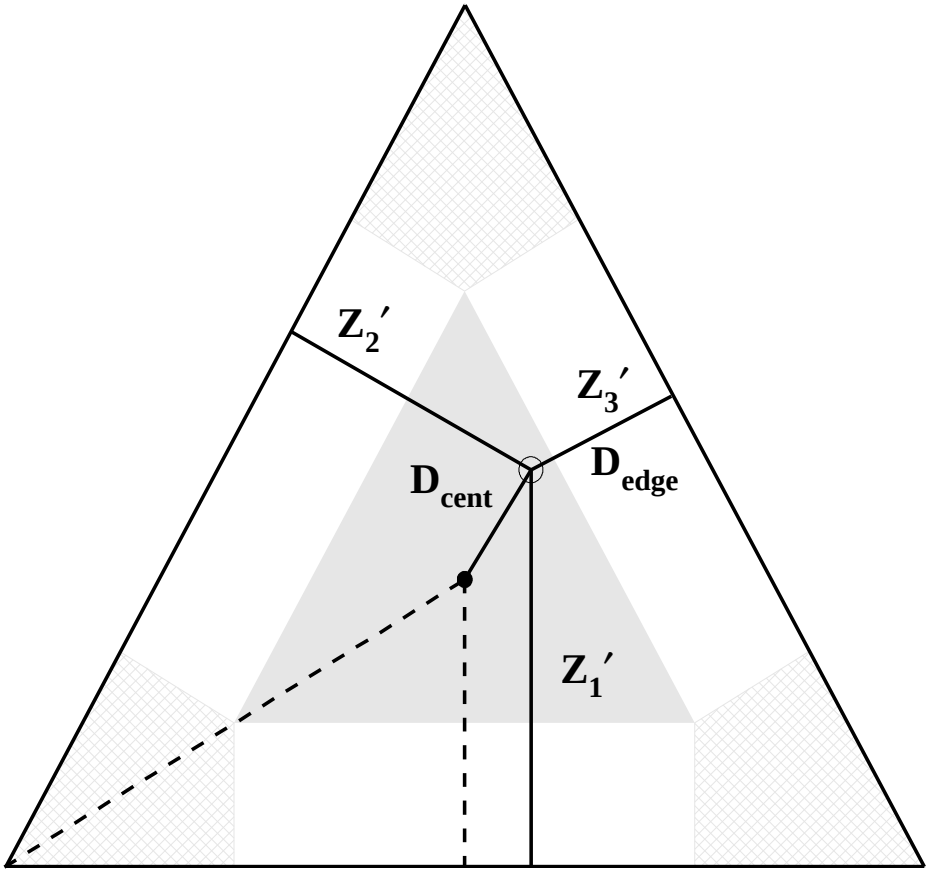

Figure 3.1: A Dalitz triangle. For each event, the reduced charges (Z_i') are set equal to the distances to the three sides of the triangle. D_{cent} is the distance from each event entry to the center, and D_{edge} ($= Z_3$) is the distance to the nearest edge. Further features are explained in the text.

As noted, this technique has been used in many other analyses to illustrate qualitative trends in experimental data[Rous93, Kreu93], but it has been used to extract quantitative information as well. The authors of Reference [Biza93] have classified the relative abundance of three decay mechanisms in their data by recording the relative population of events in different regions of the Dalitz triangle. The experimental system they studied was Kr+Au at 43 MeV/nucleon. The authors of that study divided the observed range of excitation energies into four bins, and generated a Dalitz plot for each corresponding bin (Figure 3.2).

By construction, the region in the middle of each side of the triangle (Figure 3.1, unshaded) is populated by events which have, as their three largest fragments, two relatively large fragments and one relatively small fragment. The region at each of the corners (Figure 3.1, hatched) is populated by events with one large fragment and two smaller fragments. And the region in the center of the triangle (Figure 3.1, shaded) is populated by events with three equally sized fragments. Since the triangle is filled according to the reduced charges, as opposed to the actual magnitudes, the total charge of the three largest fragments ($Z_{sum} = \sum_{i=1,3} Z_i$) is a free parameter (*i.e.* events having three largest charges equal to 2:2:2 would fall in the center of the Dalitz plot, as well as those with charges 20:20:20). We shall examine this degree of freedom in more detail later in this chapter. It is for this reason that the authors of Reference [Biza93] have included the mean total charge of events plotted in each panel ($\langle Z_{frag} \rangle$).

One final detail we note is that the authors have drawn around the data in each panel the limiting edges of the Dalitz triangle. The outer lines drawn depict the boundaries of the Dalitz triangle itself. The inner lines, however, show the maximum extent possible for their experimental data set. This boundary arises from the fact that their detector apparatus had an inherent efficiency problem limiting the size

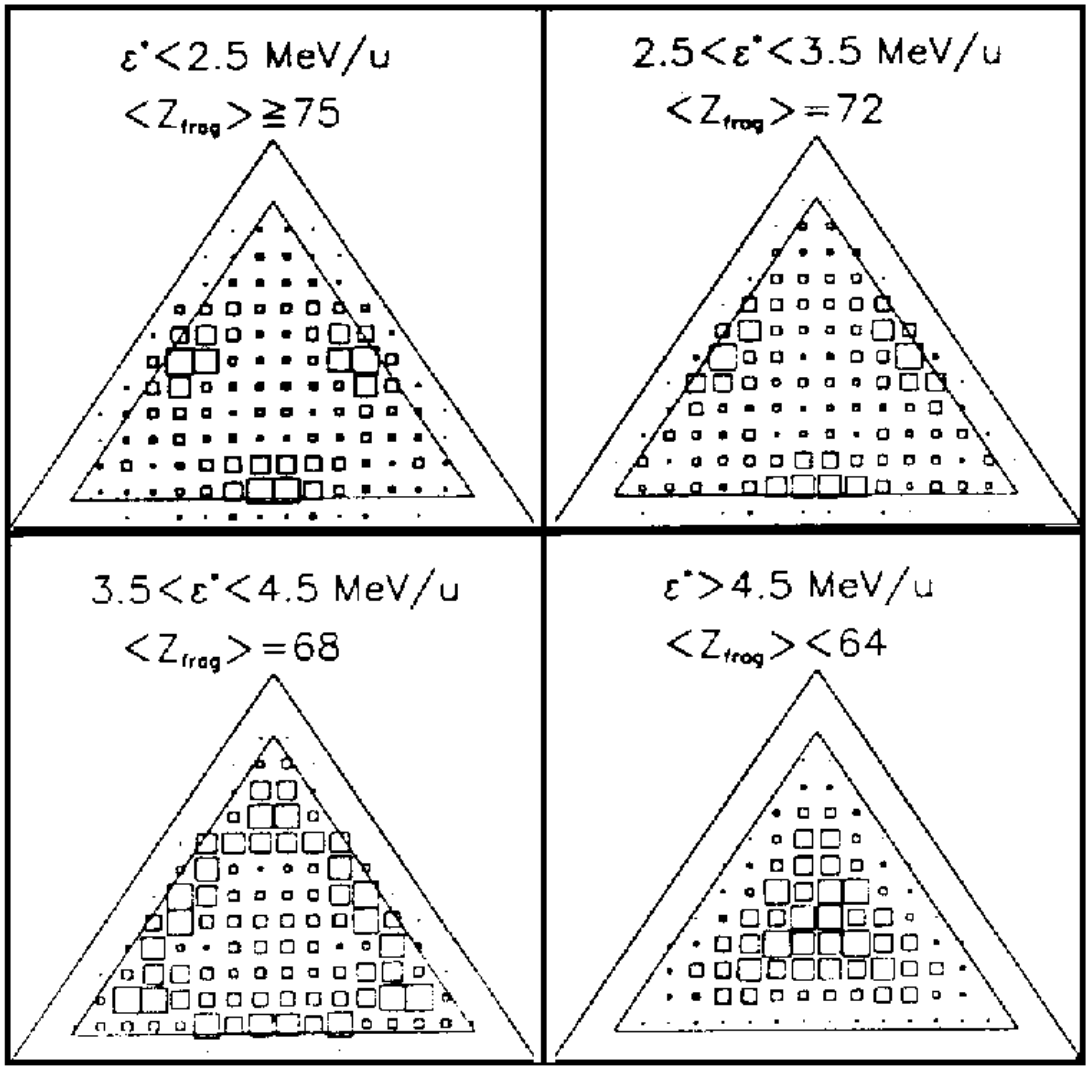

Figure 3.2: Charge Dalitz plots created for the reaction 43 MeV/nucleon Kr+Au [Biza93]. The four panels represent four different excitation energy bins, as labelled. Details of the figure are discussed in the text.

of detectable charges to $Z \geq 8$. Because the distance from the edges of the Dalitz triangle are based on the relative charges, the nearest distance to any edge is therefore $Z'_{min} = 8/(Z_{targ} + Z_{proj})$. We shall examine this boundary in more detail later in this chapter.

An examination of the experimental data in Figure 3.2 reveals that, for low excitation energies in this system ($\epsilon^* < 2.5$ MeV/nucleon) the regions at the centers of the sides are predominantly populated. The authors ascribe the occurrence of such events to the predominance of symmetric fission at these excitation energies, in which two massive fragments are emitted in conjunction with an IMF. At high excitation energies ($\epsilon^* > 4.5$ MeV/nucleon) the central region is predominantly populated. The authors attribute this to the predominance of symmetric ternary fragmentation. They then proceed to quantify these trends by counting the percentage of events which fall into the three regions of the Dalitz triangle (shaded, unshaded, and hatched regions in Figure 3.1). The relative probabilities for populating these three regions has been plotted in Figure 3.3 versus the excitation energy. This figure shows the decline in fission processes and subsequent rise in symmetric fragmentation processes with increasing beam energy. The authors proceed by locating the energy at which the probability for symmetric fragmentation becomes greater than that for fission and labelling that as point at which a transition occurs between those two decay mechanisms.

In this chapter, we choose to quantify the predominant population in Dalitz triangles via two distances D_{cent} and D_{edge}. These quantities are the distance from the coordinates of each event entry to the center of the Dalitz triangle, and the distance from the coordinates of each entry to the nearest edge, as labelled in Figure 3.1. Events with three or more nearly equally sized largest fragments will populate the center of the triangle ($D_{cent}<D_{edge}$), while those with one large fragment and two

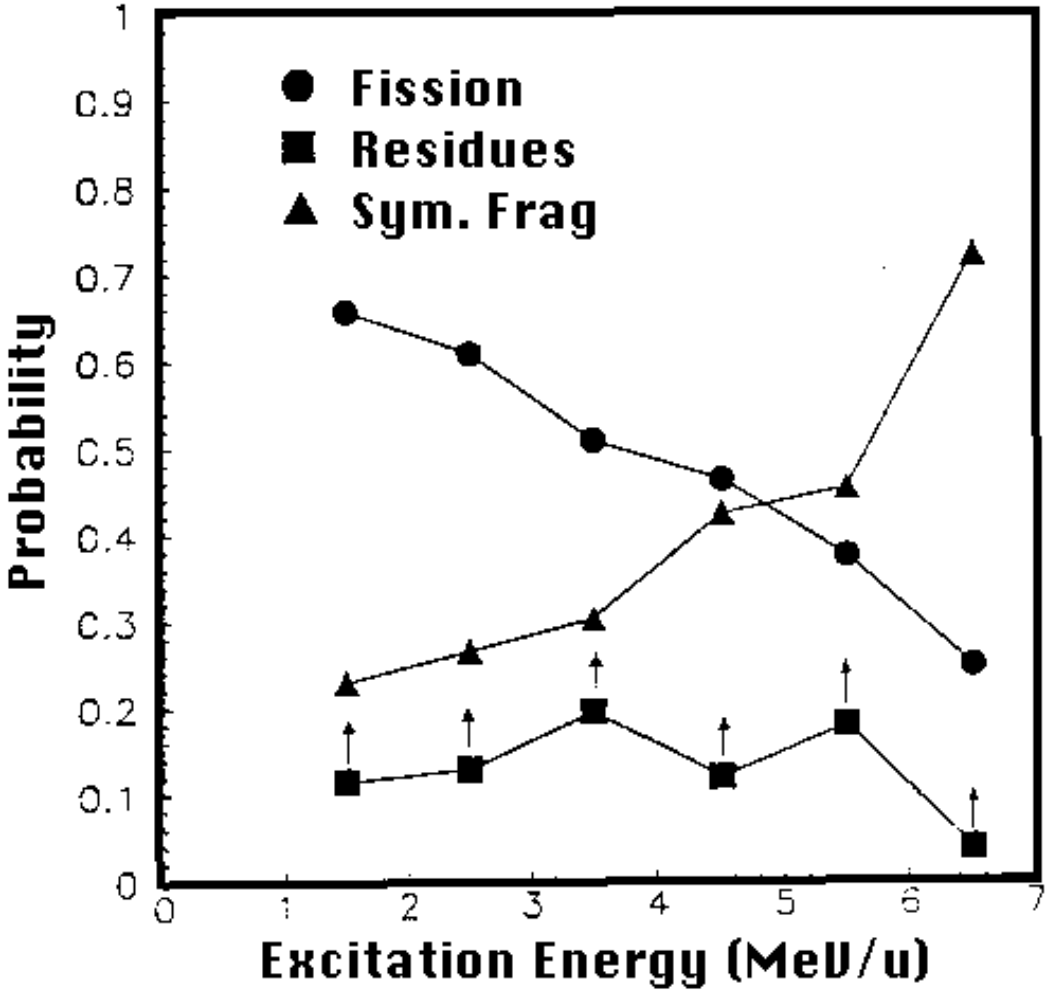

Figure 3.3: The relative probabilities of populating the three regions in a Dalitz triangle for 43 MeV/nucleon Kr+Au collisions[Biza93]. Each of the three lines has been labelled according to the reaction decay mechanism leading the population of that region in the triangle.

smaller, or two large fragments and one smaller, will populate the corners or sides of the triangle, respectively ($D_{cent}>D_{edge}$). In this way we can calculate an average value for this quantity and determine whether the measured events have an overall charge symmetry or asymmetry. Based on the above studies, we make the association of $\langle D_{cent}\rangle<\langle D_{edge}\rangle$ with multifragmentation events, and of $\langle D_{cent}\rangle>\langle D_{edge}\rangle$ with sequential binary or symmetric fission events[Kreu93, Colo92].

3.2 Experimental Measurements

The reactions studied in this chapter were ^{20}Ne+^{27}Al at beam energies of 55, 75, 95, 105, 115, 125, 135, and 140 MeV/nucleon; ^{40}Ar+^{45}Sc at 15, 25, 35, 45, 65, 75, 85, 95, 105, and 115 MeV/nucleon; ^{87}Kr+^{93}Nb at 35, 45, 55, 65, and 75 MeV/nucleon; and ^{129}Xe+^{139}La at 25, 30, 35, 40, 45, 50, 55, and 60 MeV/nucleon. The beams were obtained from the K1200 cyclotron at the National Superconducting Cyclotron Laboratory, and all of the data were collected using the MSU 4π Array (see Sec. 2.1) with a minimum bias trigger requiring two hits in any detectors of the Array. The fragment charges were well resolved over the range $1\leq Z\leq 15$ in the ^{20}Ne+^{27}Al and ^{87}Kr+^{93}Nb entrance channels, and $1\leq Z\leq 18$ in the ^{40}Ar+^{45}Sc and ^{129}Xe+^{139}La entrance channels. The distortions to the present results that are caused by the inefficiencies in experimental measurement were studied using events generated by model codes and a software replica of the detection system. These are discussed as appropriate below. The total mass and excitation energy of the excited systems formed for each reaction are constrained via the selection of central collisions, which is discussed in Appendix B. A method for avoiding autocorrelations in this selection process is also discussed there.

Sample Dalitz plots are shown for the ^{129}Xe+^{139}La system for all beam energies in

Figure 3.4. From this figure, we can identify a qualitative transition with increasing beam energy. At higher energies (E_{proj} >40 MeV/nucleon), population of the triangle is confined mainly to the center, and events having coordinates near the edges of the triangle are rare; this indicates MF decay. At low energies (25 MeV/nucleon $\leq E_{proj} \lesssim$35 MeV/nucleon), the Dalitz triangle is populated even at the edges. Furthermore, the events populating the center of the triangle lie mainly along the lines joining the center of the triangle to the corners (the counts axis is logarithmic). Since we have attributed population of the corners of Dalitz triangles with sequential binary decay, our data indicate SB decay at these low energies. This is in contrast to what we see *e.g.* in Figure 3.2, in which the authors examined an asymmetric entrance channel (Kr+Au). In each of the two cases (Figure 3.4 and Figure 3.2), multifragment decay is indicated at high energies. However, we have stated that the symmetric (asymmetric) system indicates sequential binary decay (symmetric fission) at low energies.

3.2.1 Mean Distances: D_{cent} and D_{edge}

In order to become more quantitative in our description, we will now focus on the distance observables (D_{cent} and D_{edge}) defined earlier. The average values of D_{cent} (with points) and D_{edge} (without points) in the selected central events are plotted in Figure 3.5 for all reactions. The solid lines depict these average distances for the events selected by the two-dimensional small impact parameter cut on E_t and Z_{mr}, while the dashed (dot-dashed) lines correspond to the events passing one-dimensional cuts on $E_t(Z_{mr})$ alone. For the lowest beam energies in both the ^{40}Ar+^{45}Sc and ^{129}Xe+^{139}La systems, $\langle D_{cent}\rangle > \langle D_{edge}\rangle$ in the central events. This implies an overall asymmetry in the charges of the largest three fragments in these events, and is thus consistent with a SB disassembly mechanism. These events are predominantly

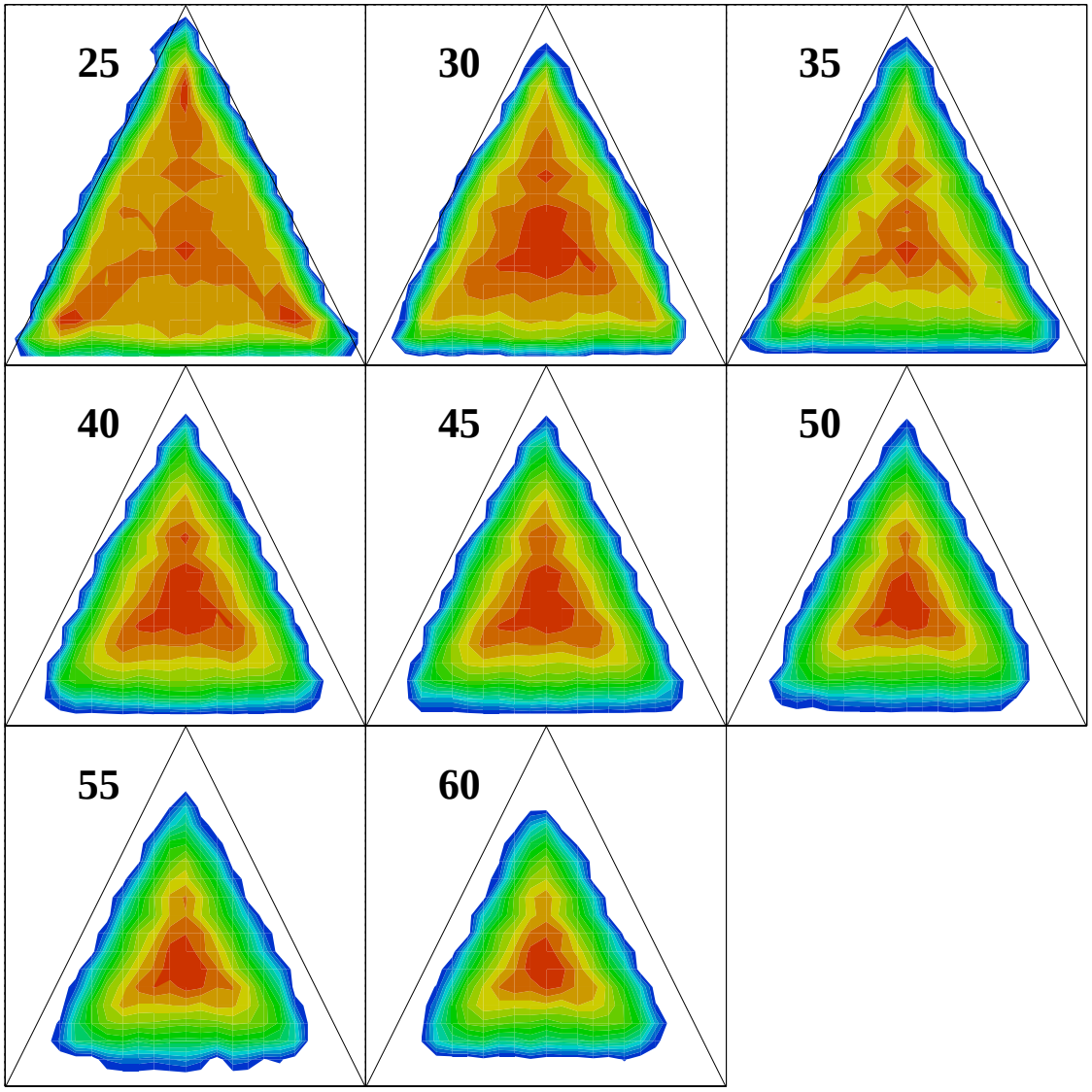

Figure 3.4: Dalitz plots for central collisions of the the ^{129}Xe+^{139}La system. Beam energies are labelled in each frame. The color contours depict the logarithm of the counts in the histogram.

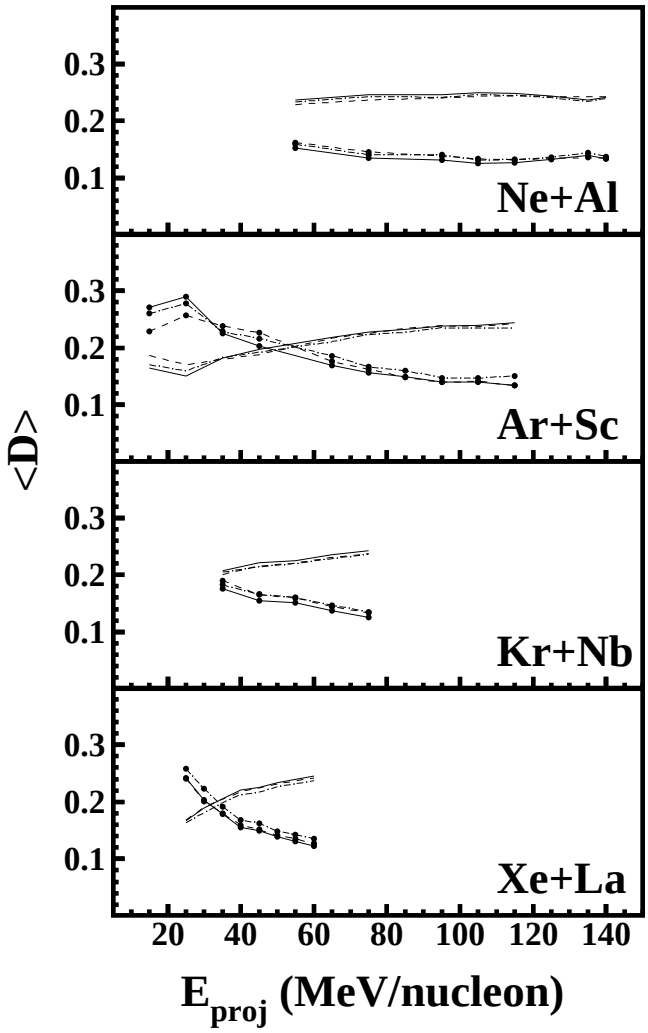

Figure 3.5: The average values of D_{cent} (with points) and D_{edge} (without points) in the central events versus the projectile energy. The solid lines depict the results for events selected by the two-dimensional cut on E_t and Z_{mr}, while the dashed (dot-dashed) lines correspond to events selected by a one-dimensional cut on $E_t(Z_{mr})$.

near the corners of the charge Dalitz triangles, implying that asymmetric fission or sequential evaporation decays are more common than those involving a symmetric binary or ternary fission. For higher beam energies in these entrance channels, as well as for all of the beam energies in the ^{20}Ne+^{27}Al and ^{87}Kr+^{93}Nb entrance channels, $\langle D_{cent} \rangle < \langle D_{edge} \rangle$. The largest three fragments in the final state are thus similarly sized, implying multifragmentation.

A beam energy that is transitional between SB and MF disassembly is defined at the crossing of the lines interpolated from the points shown in Figure 3.5. The transitional beam energies extracted from this figure for the central ^{40}Ar+^{45}Sc and ^{129}Xe+^{139}La reactions are ~50 and ~33 MeV/nucleon, respectively. The results for the central ^{87}Kr+^{93}Nb reactions are similar to those for the central ^{129}Xe+^{139}La reactions, implying a transitional beam energy somewhere in the range of 30-35 MeV/nucleon for this system. The transitional beam energies are 3-5 MeV/nucleon higher in the samples of events from the two one-dimensional cuts (dashed and dot-dashed lines) than those obtained following the two-dimensional cut (solid lines). The values of $\langle D_{cent} \rangle$ and $\langle D_{edge} \rangle$ appear to reach asymptotic values within a few tens of MeV/nucleon above the transitional beam energies.

3.2.2 Constraints

There are hidden constraints on the present method. For example, events characterized by a low value of Z_{sum} cannot, by definition, populate the extreme corners or sides of the Dalitz triangles. Indeed, there are well-defined maximum and minimum possible values of D_{cent} and D_{edge} for each value of Z_{sum}. These extrema are shown for D_{edge} in Figure 3.6 as the solid lines (analogous limits apply for D_{cent}). As Z_{sum} is decreased, the range of possible values of D_{edge} decreases, and this range tends towards larger values of D_{edge}. It is therefore possible that the crossings noted in

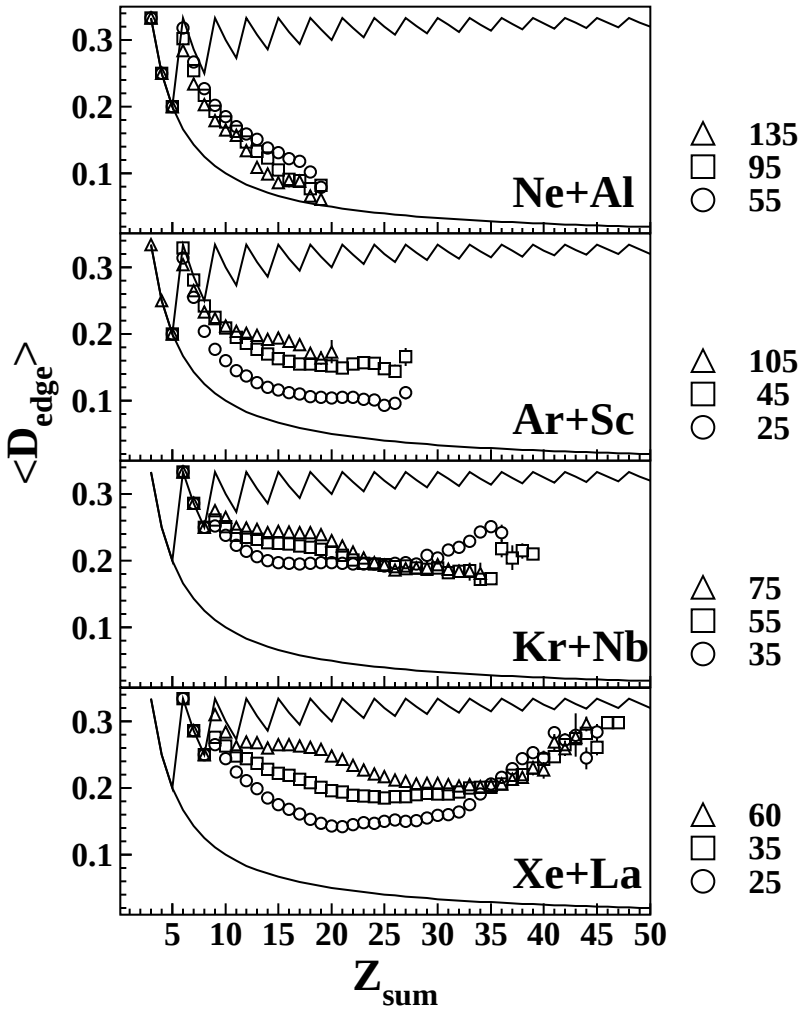

Figure 3.6: The average values of D_{edge} versus Z_{sum} in the central events for three representative beam energies in MeV/nucleon for each entrance channel, as labeled. The solid lines indicate the minimum and maximum values of D_{edge} that are possible for each value of Z_{sum} by definition.

Figure 3.5 are simply an artifact of similarly beam energy dependent decreases in the average values of Z_{sum}. The values of Z_{sum} averaged over beam energies in each entrance channel are 6.7, 9.9, 15.7, and 19.0, for the ^{20}Ne+^{27}Al through ^{129}Xe+^{139}La systems, which correspond to 29%, 25%, 20%, and 17% of the total entrance channel charge. The percentage standard deviations about these average values over the different beam energies in each entrance channel are 8%, 12%, 3%, and 7%. Thus, $\langle Z_{sum} \rangle$ is only weakly dependent on the beam energy in each entrance channel, so that the transitions noted in Figure 3.5 cannot simply be an artifact of decreases in $\langle Z_{sum} \rangle$ for increasing beam energies. The average values of D_{edge} are also plotted in this figure for three representative beam energies in each entrance channel. These reveal a dependence of D_{edge} (and D_{cent}) on Z_{sum} that generally follows the shape of the region allowed by definition. For $3 \leq Z_{sum} \leq 5$, there is only one allowed value of D_{edge} (and D_{cent}). While no relative charge information can be extracted for $3 \leq Z_{sum} \leq 5$, central events with relatively small values of Z_{sum} are nonetheless interesting, as they indicate the presence of events in which no large fragments were observed, implying the rather complete vaporization of the system.

It is important to consider also the constraints on the present observables that are imposed by the inefficiencies of the detection system. The most obvious constraint of this kind results from the maximum charge that could be detected, which was $\sim$15 for the ^{20}Ne+^{27}Al and ^{87}Kr+^{93}Nb reactions, and $\sim$18 for the ^{40}Ar+^{45}Sc and ^{129}Xe+^{139}La reactions. The effect of this limit is to decrease the sensitivity of the present observables for large values of Z_{sum}. Specifically, as the values of Z_1 and Z_2 approach the maximum detectable charge, the number of possible permutations of Z_1, Z_2, and Z_3 having the same measured Z_{sum} decreases. This leads to a situation similar to that for $3 \leq Z_{sum} \leq 5$, where the limited range of possible values for D_{cent} and D_{edge} reduces their sensitivity. In Figure 3.6, the values of $\langle D_{edge} \rangle$ manifest fairly

abrupt changes at roughly the maximum detected charge plus two, and twice that maximum plus one, corresponding to the detection of such large charges in coincidence with protons.

The values of $\langle D_{cent} \rangle$ and $\langle D_{edge} \rangle$ for the central events with $6 \leq Z_{sum} \leq 17$ for the ^{20}Ne+^{27}Al and ^{87}Kr+^{93}Nb entrance channels, and $6 \leq Z_{sum} \leq 20$, for the ^{40}Ar+^{45}Sc and ^{129}Xe+^{139}La entrance channels, are depicted in Figure 3.7. This gate on Z_{sum} allows those central events for which the present charge observables are not affected by the limiting maximum detectable charge. These curves indicate the same transitional behavior as shown in Figure 3.5, although at slightly lower beam energies: ~47 and ~29 MeV/nucleon for the ^{40}Ar+^{45}Sc and ^{129}Xe+^{139}La entrance channels, respectively.

3.2.3 Acceptance Effects

A more complete investigation of the effects of the experimental acceptance involves the generation of software events, and the comparison of the present relative charge observables in these events with and without filtering by a software replica of the apparatus. The filter code includes a complete description of effects such as detector geometry and kinetic energy thresholds (see Appendix C). Separate samples of events were generated with the Berlin code [Zhan87b], each at a specified excitation energy, in a system expected to be common in the present central ^{40}Ar+^{45}Sc reactions (Z~31, A~68). The upper two frames in Figure 3.8 depict $\langle Z_{sum} \rangle$ and $\langle D_{cent} \rangle$ after each of these samples of events is boosted from the center of momentum frame into the laboratory, and then filtered, for beam energies in the range of 25 to 105 MeV/nucleon. The events were generated at excitation energies of 2 (solid squares), 4, 6, 8, 10, 12, 16, and 20 (open crosses) MeV/nucleon. The filtered $\langle Z_{sum} \rangle$ and $\langle D_{cent} \rangle$ show only a very weak dependence on the magnitude of the boost into the laboratory for all of the samples of generated events. The crossings noted in Figures 3.5 and 3.7 are therefore

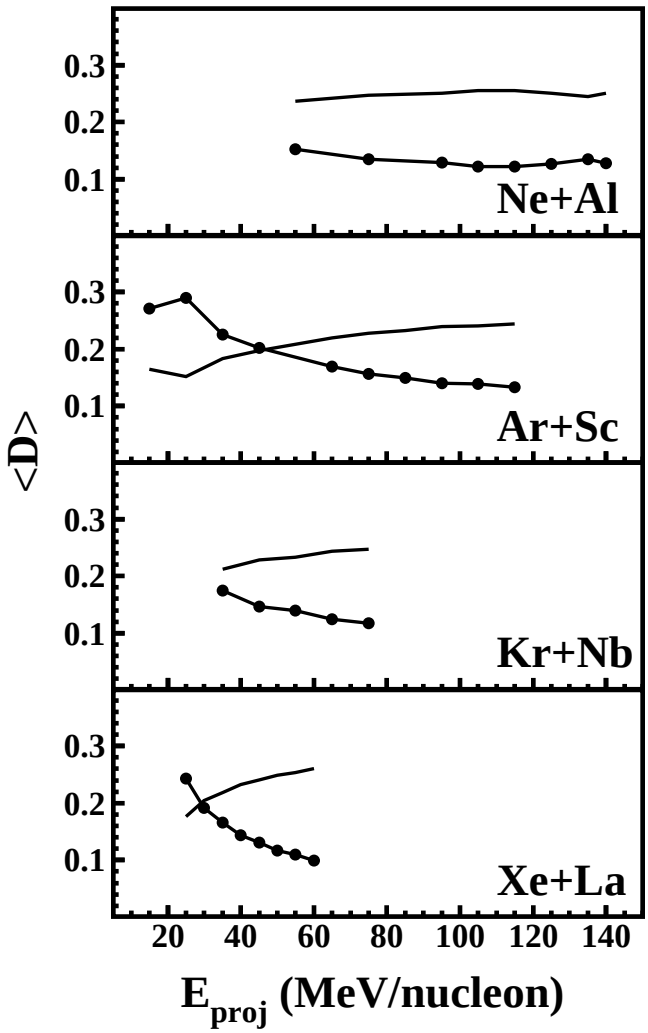

Figure 3.7: The average values of D_{cent} (with points) and D_{edge} (without points) versus the beam energy for specific gates on the quantity Z_{sum}: $6 \leq Z_{sum} \leq 17$ for the ^{20}Ne+^{27}Al and ^{87}Kr+^{93}Nb entrance channels, and $6 \leq Z_{sum} \leq 20$ for the ^{40}Ar+^{45}Sc and ^{129}Xe+^{139}La entrance channels.

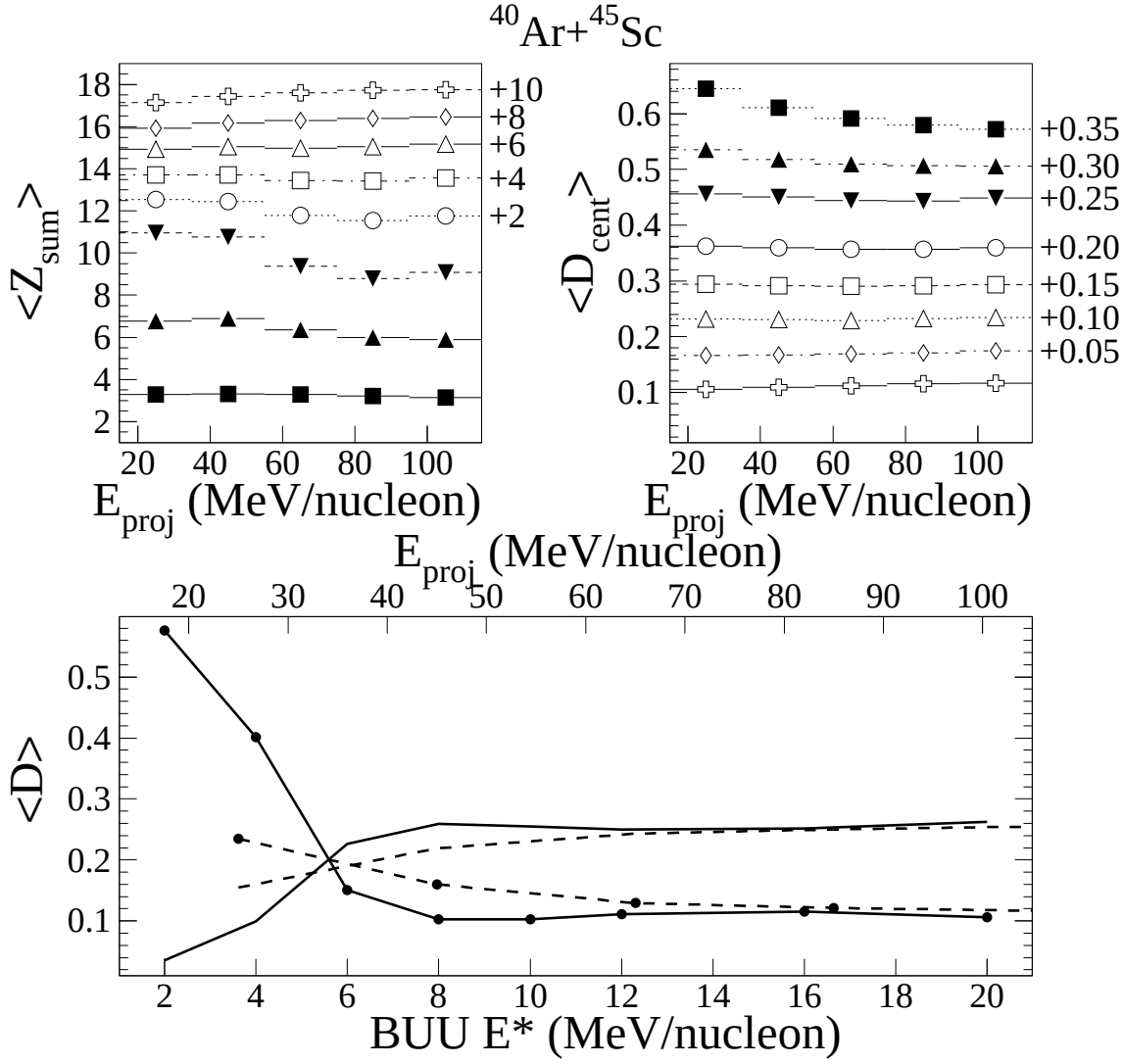

Figure 3.8: The average values of Z_{sum} (upper left frame) and D_{cent} (upper right frame) obtained from eight samples of events, each generated at a specific excitation energy for central ^{40}Ar+^{45}Sc reactions using the Berlin code. Each sample is boosted from the CM frame to the laboratory, and then filtered, for beam energies from 25 to 105 MeV/nucleon. Some points in the upper frames have been offset for clarity by the amounts shown to the right. The lower frame compares the excitation energy dependence of the unfiltered Berlin events with the beam energy dependence of the filtered Berlin events, using BUU calculations to relate the beam and excitation energies for central ^{40}Ar+^{45}Sc reactions.

not the result of a strong beam energy dependence of the experimental acceptance.

The solid curves in the lower frame in Figure 3.8 depict the excitation energy dependence of $\langle D_{cent} \rangle$ (with points) and $\langle D_{edge} \rangle$ (without points) for the unfiltered Berlin events. The unfiltered Berlin events evolve from the corners to the center of the charge Dalitz triangles, and exhibit a crossing excitation energy near 6 MeV/nucleon. Boltzmann-Uehling-Uehlenbeck (BUU) calculations are one means of specifying the relationship between the beam energy and the average excitation energy for central collisions. These calculations were performed as described in Reference [Made93, Bowm92], and the predicted relationship between the beam and excitation energies is visible by comparing the upper and lower abscissa in this lower frame. The dotted lines in this frame depict the values of $\langle D_{cent} \rangle$ and $\langle D_{edge} \rangle$ following the boosting and filtering of the generated events assuming this relationship. The apparent crossing (beam) energy is only weakly affected by the imposition of the experimental inefficiencies via the software filter. The major effect is to reduce the apparent asymmetry of the three largest charges for asymmetric events, i.e. those in the SB region.

Chapter 4

Observation of Non-Compact Geometries

4.1 Signatures

In this chapter we will examine experimental observables, termed signatures, predicted to show sensitivity to the formation of non-compact geometries. Examples of these signatures include the following observables:

- IMF Multiplicity
- Charge Similarity
- Fragment Charge Correlation Functions
- Event Shapes
- Multipolarity Coefficients
- Fragment Velocity Correlation Functions
- Kinetic Energy Spectra

Each of these observables has been proposed for use in identifying the occurrence of exotic geometries. We examine them each in the following.

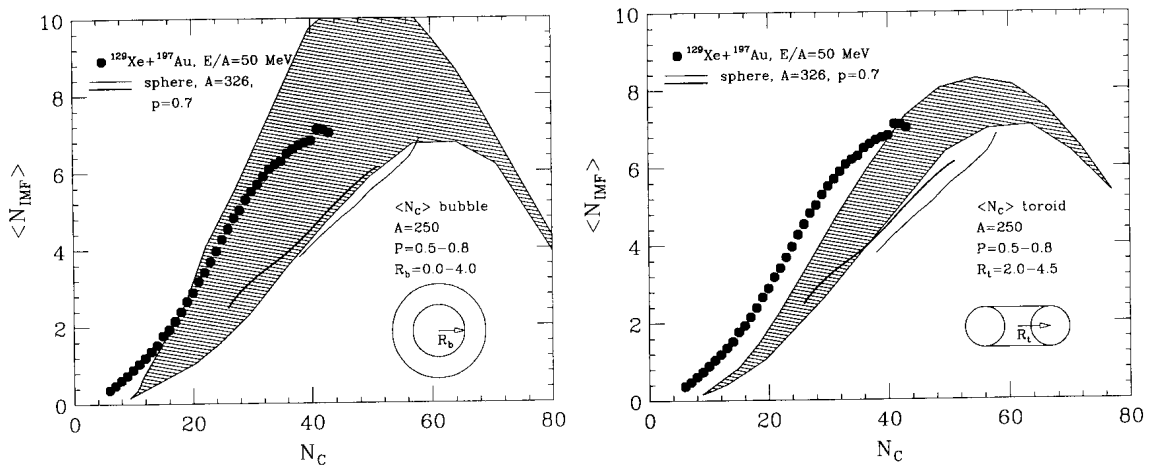

(a) (b)

Figure 4.1: IMF multiplicity versus the total charged particle multiplicity resulting from percolation model calculations[Phai93]. The solid lines (both panels) show the values obtained from percolation of a compact spherical configuration, while the shaded regions show the values obtained from percolation of initial toroid (panel a) and bubble (panel b) geometries. The markers (both panels) show a comparison to an experimental data set.

IMF Multiplicity

An enhancement in the IMF multiplicity (N_{imf}) has been proposed by several authors [Baue92, Xu93] as a consequence of the formation of a non-compact geometry. The authors of Reference [Phai93] have performed percolation model calculations to quantitatively demonstrate that decay from non-compact geometries (toroids and bubbles) will result in emission of more IMFs than would be observed in the decay of a compact spherical geometry (see Figure 4.1). In this figure, IMF multiplicity values resulting from percolation of compact spherical distributions are depicted by the solid lines. The shaded regions show the range of multiplicity values that result from a range of parameters defining a bubble (panel a) and a toroid (panel b). Specifically, values near the bottom of the shaded region will result when the interior radius of the configuration (R_b, R_t, defined in the inset) goes to zero. As the radius parameter is increased, observed multiplicity values move toward the upper limits of the shaded

regions. Thus, in both cases, we see that percolation from non-compact geometries results in IMF multiplicities that are higher than those found from the percolation of a compact spherical configuration.

Charge Similarity / Charge Correlation Functions

Several authors have predicted that the formation of non-compact geometries will result in the emission of large fragments with nearly equal sizes[More92, Guar95]. They motivate this effect by comparing toroid and bubble formation to the formation of a tube or sheet. If such a tube (sheet) forms, then the nuclear matter in that tube (sheet) will tend to coalesce into fragments with diameters similar to the thickness of the tube (sheet). If then the tube (sheet) has a uniform thickness, then such a mechanism would yield fragments with similar diameters (*i.e.* masses). The authors of Reference [Xu93] have also quantified the sizes and multiplicities of similarly sized fragments. The authors of Reference [More96] have proposed looking for this charge similarity with Charge Correlation Functions, and have demonstrated some success at quantifying even small admixtures of events having similar charges.

Event Shapes / Multipolarity Coefficients

Event shape observables, so called because of their ability to assign a quantitative measure to the shape of an event in momentum space, have been used widely used to characterize the shapes of nucleus-nucleus events[Gyul82, Fai83, Lópe89, Cugn83]. It is their sensitivity to the dimensionality of fragment emission which has led to the anticipation that these variables should also show sensitivity to the breakup geometry[Xu93]. Specifically, if the combined system were coplanar (*e.g.* toroid or disk) as opposed to spherical (*e.g* bubble or compact sphere), one might expect emission angles of fragments to lie predominantly within the plane defined by the

initial configuration.

The use of multipolarity coefficients was proposed by the authors of Reference [Souz94] as a means of quantifying angular distributions of fragments. The concept is essentially one of a fourier transform of the angular distribution in terms of the spherical harmonics ($Y_{l,m}(\theta, \phi)$). By examining these coefficients, the authors propose another way of quantifying the shape of the event via angles alone as opposed to momenta (angles and energy). However, the authors of this study issue a strong caution due to the sensitivity of this type of analysis to slight non-centrality in event selection.

Fragment Velocity Correlation Functions / Kinetic Energy Spectra

The sensitivity of velocity correlation functions to the formation of non-compact geometries relies upon the suppression of the Coulomb acceleration of emitted fragments. Specifically, fragments distributed within a compact sphere are closer together than they would be in a non-compact configuration. Since the relative Coulomb acceleration between two particles is inversely proportional to their initial separation, fragments emitted from non-compact geometries should experience lower Coulomb boosts. Examining velocity correlation functions was proposed by the authors of Reference [Glas93], however the observed effect was small, even for their simulation calculations. Since relative coulomb boosts between fragments are expected to be suppressed for non-compact configurations, there should also arise a number of fragments with lower kinetic energies than would be otherwise observed. However, this enhancement at low kinetic energies (less than 1 MeV/nucleon for large fragments) is a difficult signature to pursue due to considerations of detector energy thresholds.

The analysis presented in this chapter will focus on a subset from the signa-

tures described above. We will present data pertaining to IMF multiplicities, charge similarity and event shapes, in lieu of the others listed which suffer from distinct shortcomings, as noted.

4.2 Experimental Measurements

The experimental data for this study were collected for the ^{86}Kr+^{93}Nb system for the beam energies 35, 45, 50, 55, 60, 65, 75, 85, and 95 MeV/nucleon. Our study includes only central events from this data set because the formation of non-compact geometries is predicted for central events[Baue92, Xu93]. We selected central events from our data with the well-established method of imposing cuts on global observables called centrality variables[Cava90, Phai92] (see Appendix B). In order to avoid autocorrelations between the centrality variables and the experimental signatures we present (see Appendix B), we have used two different centrality variables: the total transverse kinetic energy (E_t) and the total charge of detected fragments traveling at mid-rapidity (Z_{mr}). To ensure the centrality of the data sample we applied cuts on E_t accepting only the 5% most central events when dealing with charge-based signatures, and similar 5% cuts on Z_{mr} when dealing with the event shape signature.

4.2.1 IMF Multiplicity

The first experimental signature we present is an anomalous increase in the number of intermediate-mass fragments (IMFs). We have measured the multiplicity of IMFs in central events selected via cuts on E_t and plotted the mean values versus the incident beam energy per nucleon in Figure 4.2. Statistical error bars are smaller than the marker size. Two features are clear in this figure. The first is a general trend in which this multiplicity increases with increasing beam energy. This trend in IMF emission has been documented in previous experimental studies[Peas94, Llop95a]. The second

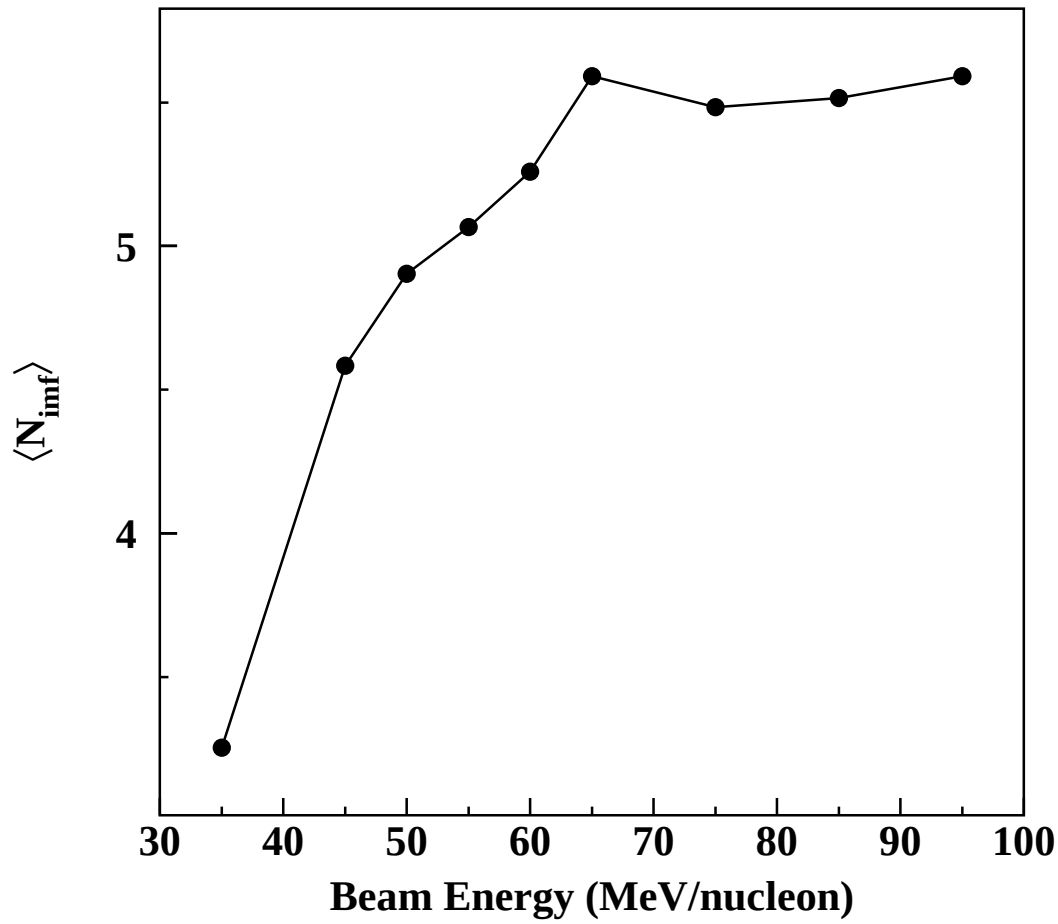

Figure 4.2: Mean intermediate-mass fragment multiplicity versus the incident beam energy.

feature is an increase in the mean IMF multiplicity, deviating from the more basic trend, at a beam energy of 65 MeV/nucleon.

This multiplicity enhancement is not caused by systematic effects of our detector acceptance. To support this claim, we have performed detailed simulations in which we generated realistic events which we passed through a software replica of our detector (see Appendix C). In so doing, we are able to extract the efficiency for detecting IMFs as a function of the incident beam energy. The extracted efficiencies are shown in Figure 4.3. Clearly, the IMF detection efficiency increases smoothly over the range of energies shown in this Chapter. The enhancement in IMF production observed in the experimental data is consistent with the increase in IMF emission predicted to accompany the formation of non-compact geometries[Baue92, Xu93, Phai93].

To further elucidate the character of these events, we have also calculated the total charge of detected IMFs (Z_{imf}) in these same events. The mean values of the this quantity are shown in Figure 4.4. From this figure, it is apparent that not only does the number of IMFs increase at 65 MeV/nucleon, but the amount of the combined system being converted to IMFs also increases.

4.2.2 Ordered Charges

The second signature we present is an enhanced similarity in the charges of larger fragments. Some theoretical models have quantitatively predicted that the formation of non-compact geometries will also result in increased cross sections for the emission of fragments with nearly equal masses[Xu93]. To quantify this for our data, we have calculated the power-law exponents for ordered Z distributions. This calculation begins with the ordering of the charges of the detected fragments, from largest to smallest, on an event-by-event basis. In this way, each fragment is assigned an index from 1 to N_c, the total number of charged particles. We then calculate the mean

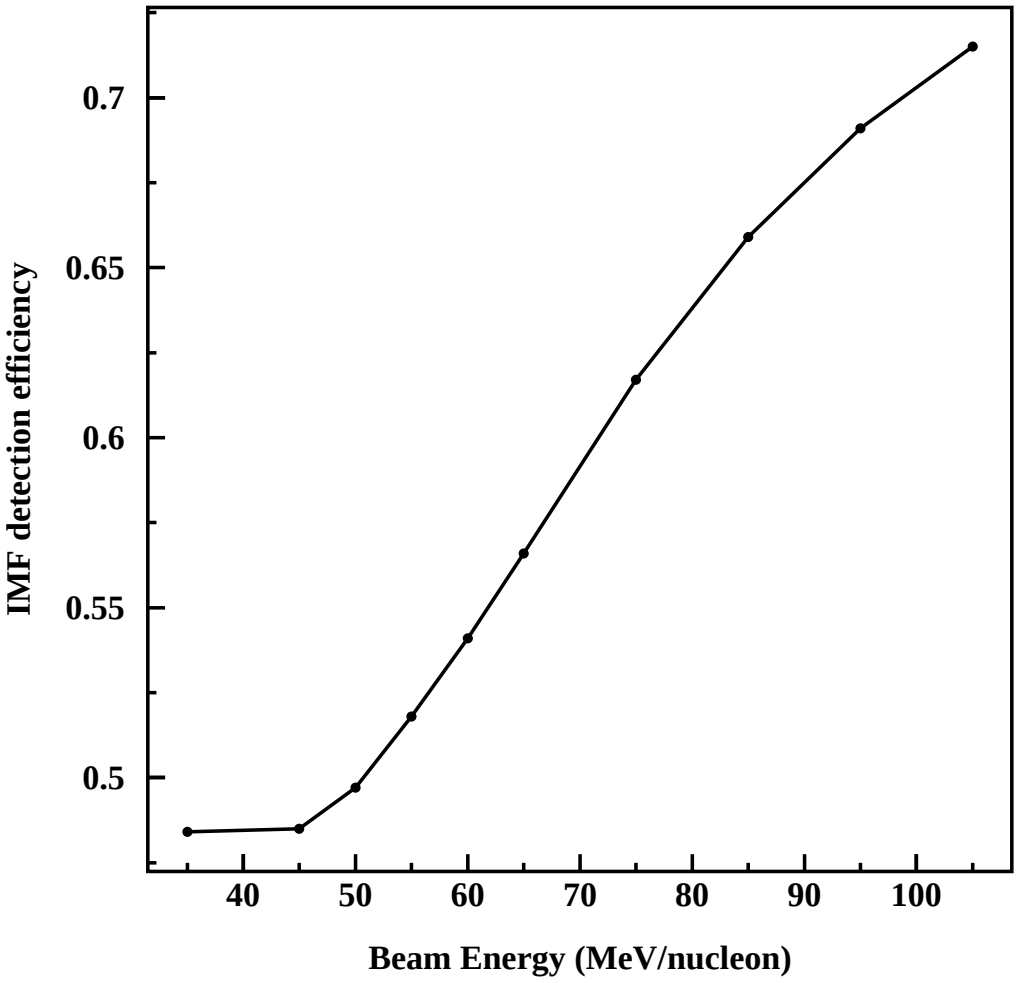

Figure 4.3: Energy dependance of estimated efficiency for IMF detection, extracted from filtered simulations.

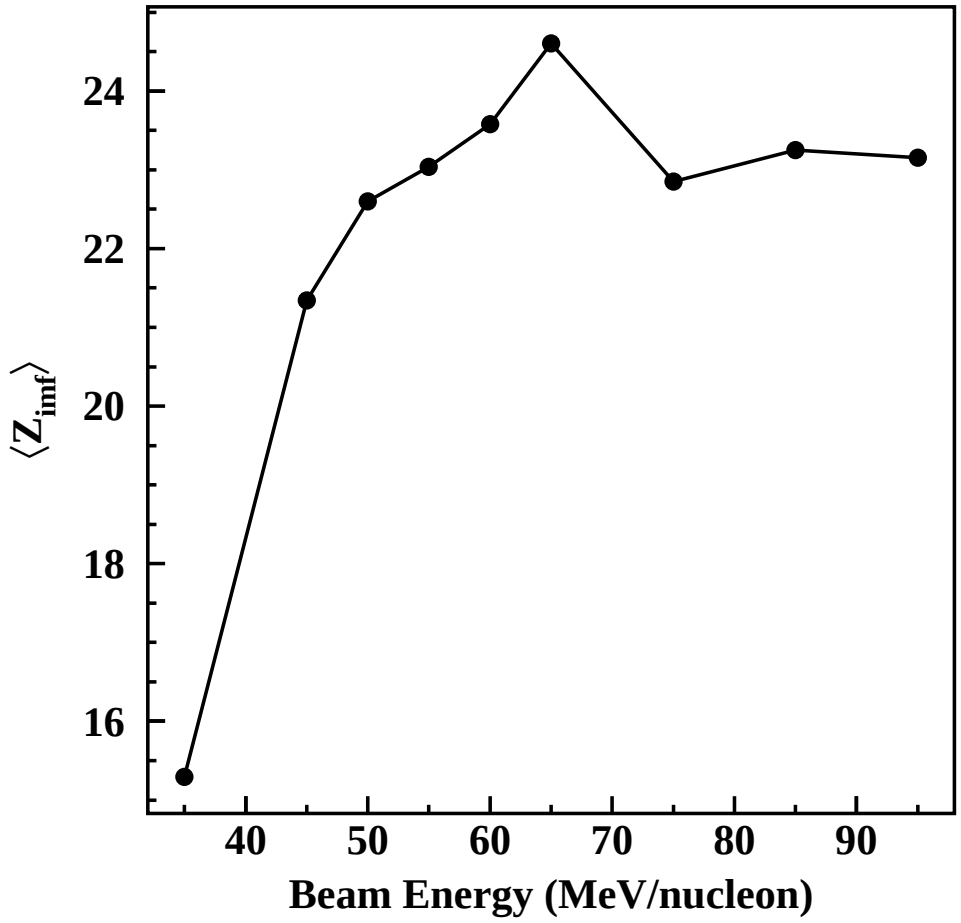

Figure 4.4: Mean total charge of IMFs versus the incident beam energy.

for each of these indexed charges over all events in our sample. The ordered charge distributions measured for central events are shown in Figure 4.5 (markers) for all beam energies. We have observed empirically that these ordered Z distributions are best reproduced by a power-law (*i.e.* $\langle Z_{ord}(i) \rangle \propto i^{-\alpha}$), although the qualitative features of the signature we present below are relatively insensitive to the fit type. Sample power-law fits are also shown in Figure 4.5 (lines). It follows that the fit parameter α for these distributions would be large for events which contain very differently charged fragments and small for events which contain similarly charged fragments. Thus, the presence of a non-compact break-up geometry, giving rise to more similarly charged large fragments, should be accompanied by a suppressed value of this exponent.

We have extracted the power-law exponent α for central events selected via cuts on E_t and plotted them versus the beam energy in Figure 4.6. Statistical errors are smaller than the markers, and systematic fitting errors are plotted. We observe an overall smooth trend in α, decreasing nearly linearly with increasing beam energy. It is clear that this observable, like the IMF multiplicity, also undergoes a departure from the overall smooth trend, and at similar beam energies. The extracted α values at 65 and 75 MeV/nucleon are suppressed so that they lie below the values consistent with a smooth trend. This suppression in α is an indication of more equally sized large fragments and is predicted to accompany the formation of non-compact geometries[Xu93].

Based on the aforementioned quantitative and qualitative predictions, the two charge-based observables shown above demonstrate trends that are well explained by the decay of non-compact geometries. However, to differentiate between the possibilities of toroid and bubble formation an additional signature is required. The use of event shape observables to make precisely this distinction was proposed by the

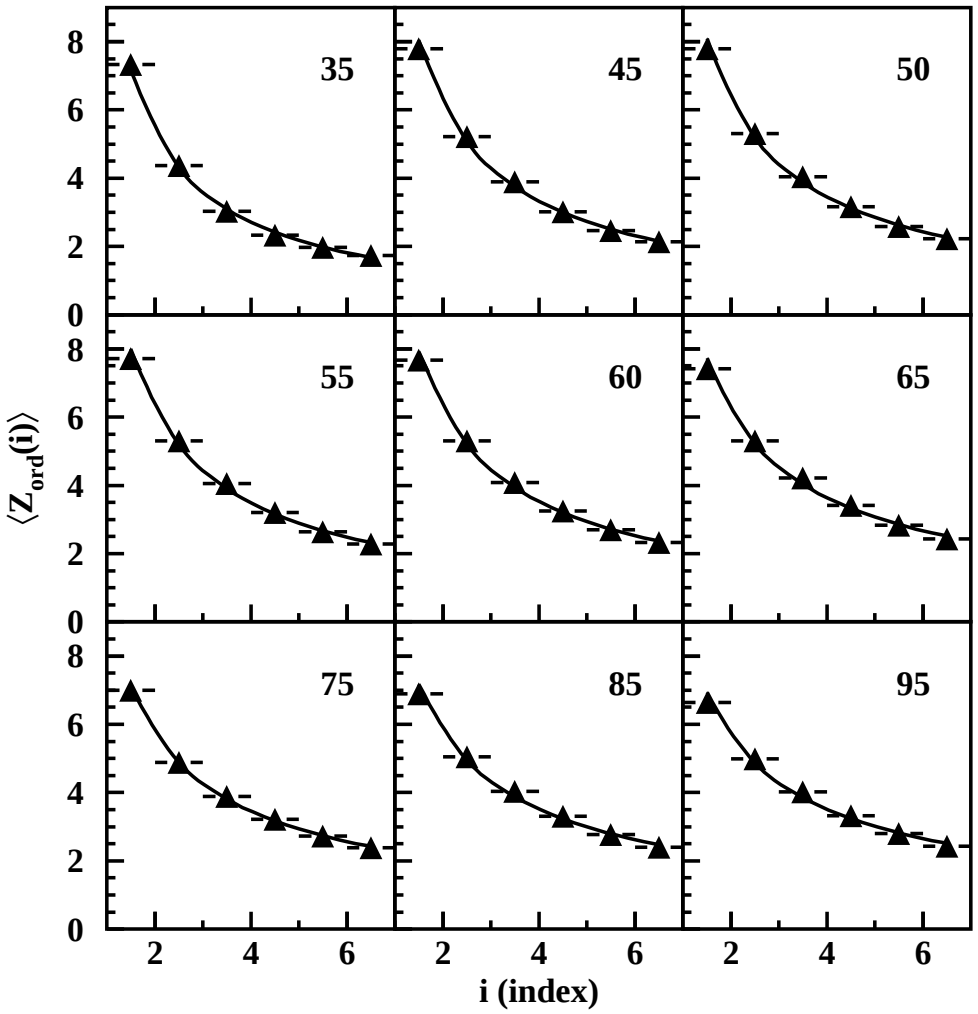

Figure 4.5: Ordered Z distributions (markers) for all beam energies, as labelled. The solid line is a fit to the function $\langle Z_{ord}(i)\rangle \propto i^{-\alpha}$.

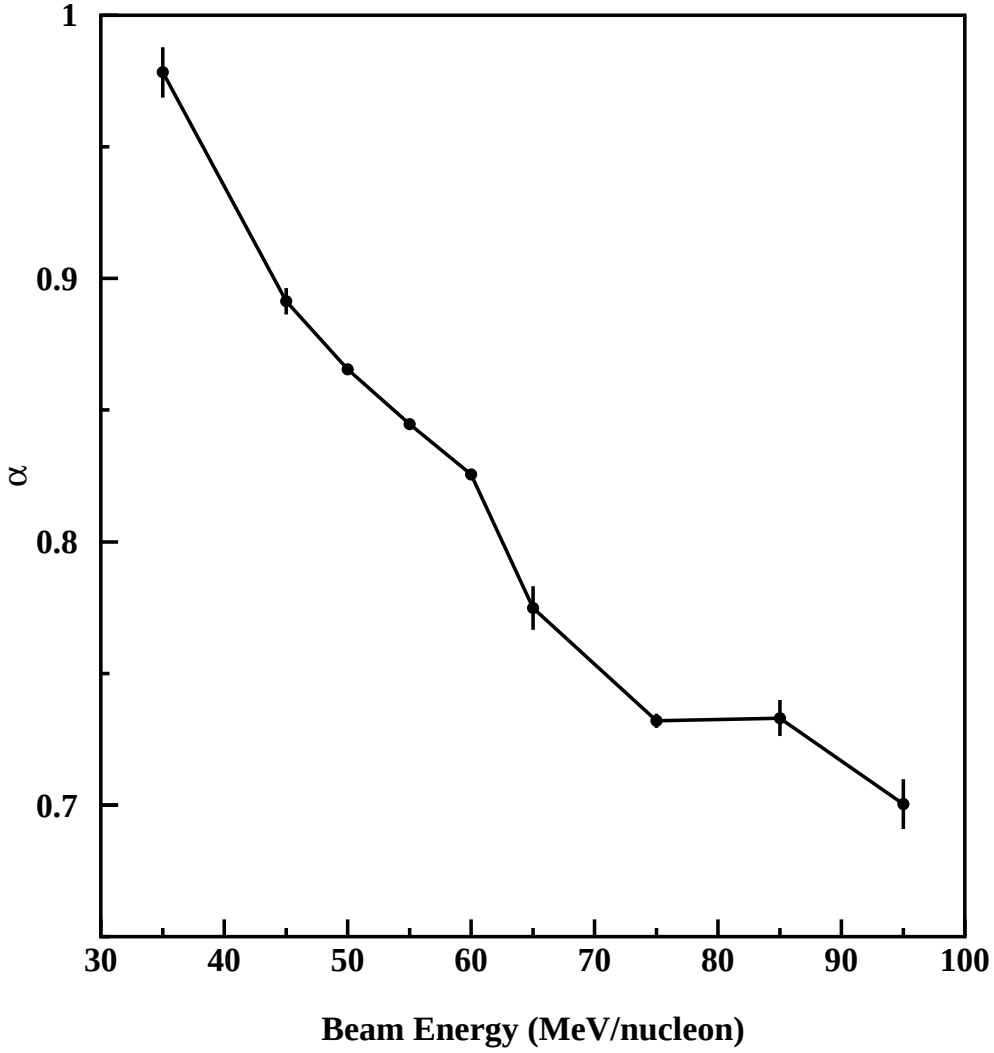

Figure 4.6: Power-law (α) values extracted from ordered charge distributions plotted versus the incident beam energy.

authors of Reference [Xu93].

4.2.3 Event Shapes

The third signature we present is a suppressed sphericity in the emission of heavy fragments. It is derived from the sphericity of particle emission in momentum space, and it ascribes a quantitative measure to the dimensionality of the break-up geometry. Such an observable includes all of the information measured for each fragment (*i.e.* mass, energy, emission angles), and thus provides a good balance to observables based on charges alone. Sphericity is defined[Fai83] by first generating the kinetic energy tensor[Gyul82] such that

$$T_{ij} = \sum_{n=1}^{N_{imf}} \frac{p_{i,n} p_{j,n}}{2m_n} \tag{4.1}$$

where N_{imf} is the number of IMFs in each event, and $p_{i,n}$ and m_n are the i^{th} component of the momentum and the mass of each IMF, respectively. Next, the eigenvalues (λ_i) of this tensor are calculated, which correspond to the sizes of the axes of the ellipsoid in momentum space. These eigenvalues are then ordered ($\lambda_1 > \lambda_2 > \lambda_3$) and normalized ($q_i = \lambda_i / \sum_{j=1}^{3} \lambda_j$). All of the event shape variables that we will show are defined in terms of these normalized eigenvalues. Their definitions, complete with limiting values, are listed in Table 4.1. We have defined all of the shape variables that we have found discussed in the literature[Fai83, Lópe89, Cugn83], although we will highlight the Sphericity later in this chapter. Given these definitions, events with isotropic emission of IMFs will have a high value of sphericity, while those with coplanar or otherwise non-spherical emission will have lower values. The values of the event shape variables are affected not only by the overall shape of the event, but also by the multiplicity of particles (N_{imf}) in the tensor sum. The range of allowed values of these variables is a limitation we must treat explicitly. To account for this we will compare events having the same IMF multiplicities, as in Reference [Llop95b].

q Name	Symbol	Definition	Limiting Values		
			Sphere	Disk	Rod
Sphericity	S	$\frac{3}{2}(q_2+q_3)$	1	$\frac{3}{4}$	0
Coplanarity	C	$\frac{\sqrt{3}}{2}(q_2-q_3)$	0	$\frac{\sqrt{3}}{4}$	0
Jettiness	j	q_1-q_2	0	0	1
Prolateness	ϕ	$\frac{q_2-q_3}{q_1-q_3}$	Undef.	1	0
Eccentricity	ϵ	$q_s-\frac{1}{2}(q_2+q_r)$ $q_s=q_1$, $q_r=q_3$ (prolate) $q_s=q_3$, $q_r=q_1$ (oblate)	0	-1	1

Table 4.1: Definitions of event shape variables. The limiting cases shown in the last columns represent the values obtained for the aspect ratios $\frac{1}{3}$:$\frac{1}{3}$:$\frac{1}{3}$, $\frac{1}{2}$:$\frac{1}{2}$:0 and 1:0:0, respectively[Cugn83]. The definition of Eccentricity depends on the momentum-space configuration. Prolateness (oblateness) is defined via the relation $q_1-q_2>(<)q_2-q_3$.

We can illustrate the multiplicity distortions to the shape variables through the use of an event generator. We have used the event generator EGSIM[Gual95] to create events with well-defined momentum-space fragment emission patterns. The aspect ratio of the momentum ellipsoid is one of the primary input parameters to this generator. Details regarding the other input parameters necessary to run this generator are discussed in Appendix C. Thus, we can generate events with constrained momentum-space aspect ratios. Since the values of event shape variables are directly related to this aspect ratio, EGSIM provides an excellent vehicle for probing multiplicity distortions and also acceptance effects.

In order to first demonstrate that EGSIM is capable of generating distinctly spherical, disklike and rodlike events, we have run simulations with input aspect ratios of 1:1:1, 2.5:2.5:1 and 1:1:2.5, respectively. The resulting center-of-momentum frame momentum distributions are shown in Figure 4.7. The disk-like (rod-like) emission of fragments can be clearly seen by the flattening (elongation) along the Z-axis in these P'_x vs. P'_z and P'_y vs. P'_z histograms.

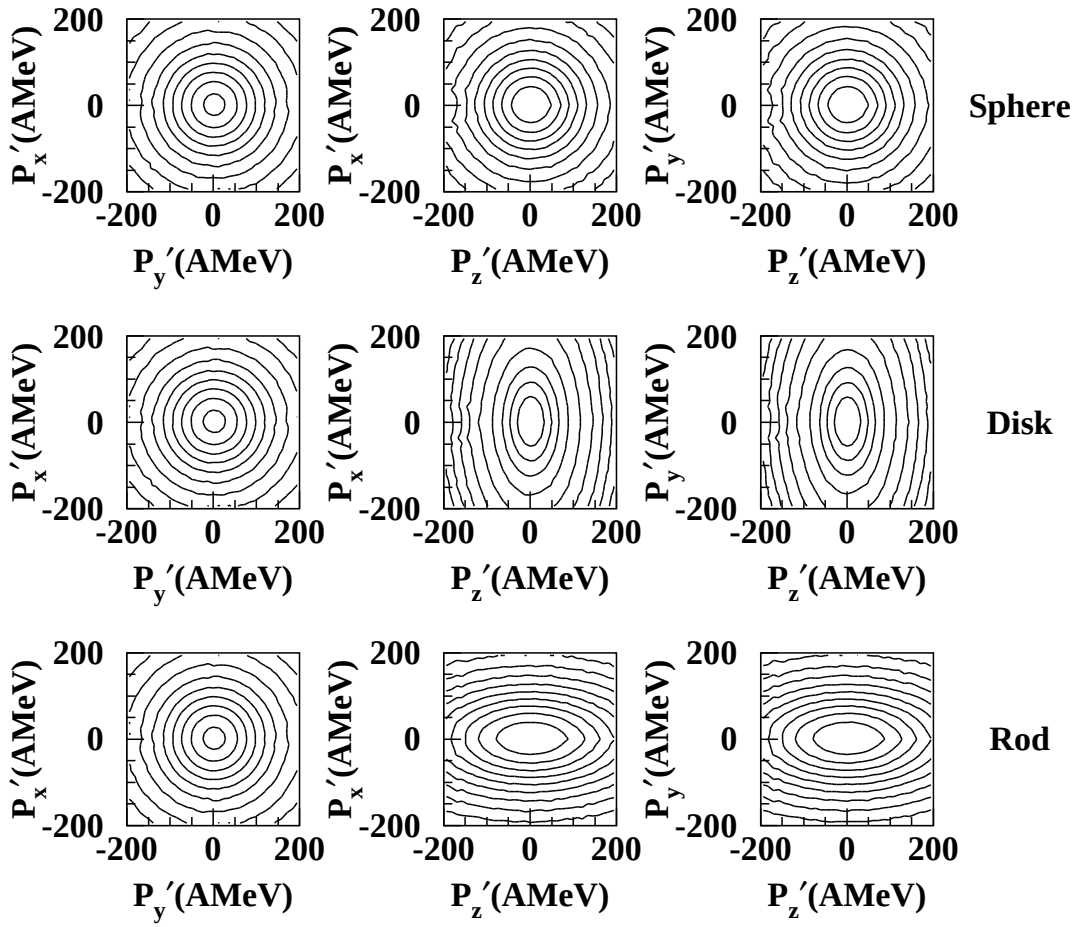

Figure 4.7: Center-of-momentum frame momentum profiles of spherical (top row), disk-like (middle row) and rod-like (bottom row) simulated events.

We have calculated mean values for each of the 5 shape variables defined in Table 4.1, and have plotted them versus the IMF multiplicity in Figure 4.8. In this case, only IMFs are included in the tensor sum (Equation 4.1). Initially, all variables appear to be well-behaved. Each variable shows some sensitivity to the three different configurations, most efficiently for higher multiplicities. However, a close examination of the plots for Coplanarity (C), Prolateness(ϕ), Eccentricity(ϵ) and the second reduced eigenvalue (q_2) reveals crossing points between the sphere and disk lines. These crossing points represent severe multiplicity distortions to the shape variables which display them. For example, it is clear from the Coplanarity plot that a sphere has a higher Coplanarity than a disk, if it is created with roughly 5 particles or less. This effect is not only counter-intuitive, but compromises its ability to make a correct event shape identification.

To further clarify this distortion, we have plotted the mean values of the 5 event shape variables and 3 reduced eigenvalues versus the total charged particle multiplicity (see Figure 4.9). In this case, all particles, not only IMFs, are included in the tensor sum (Equation 4.1). We should expect to see the same trends in these plots, since the kinetic energy tensor is coalescence invariant. This method allows us to plot on an expanded scale, which provides an indication of the asymptotic limits of the shape variables. Even with the expanded scale, agreement between the IMF multiplicity plots of Figure 4.8 and these plots can be verified (*i.e.* coalescence invariance). From Figures 4.8 and 4.9 we can identify that there are actually two types of multiplicity distortions. The first is the narrowing of the range of observed values at low multiplicities (all three curves join at $N_{imf} = N_c = 1$), but the second is the reversal of the expected (asymptotic) trends at low multiplicities, evidenced by the crossing of the sphere and disk lines. For the remainder of this chapter, we will confine our discussion of event shapes to the sphericity, because this variable is

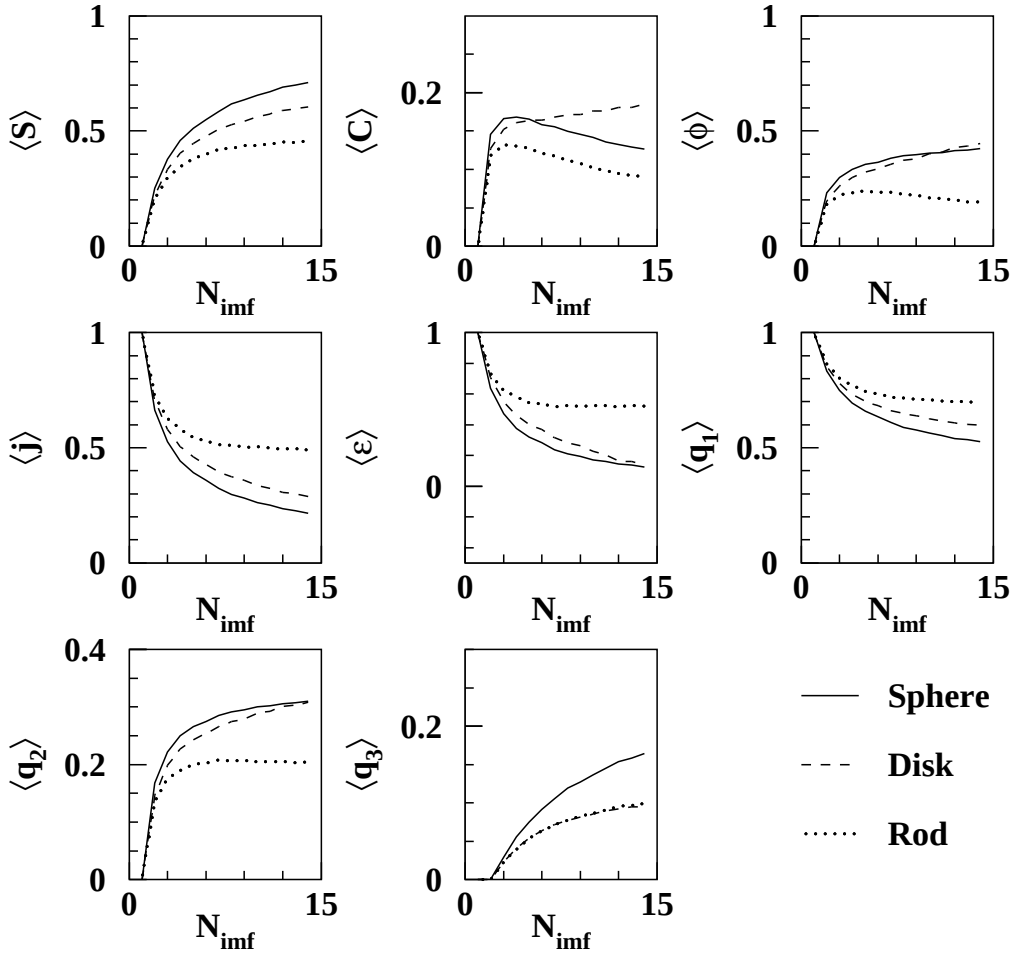

Figure 4.8: Calculated behavior of all shape-variables for simulated spherical(solid lines), disklike (dashed lines) and rodlike (dotted lines) events, plotted versus IMF multiplicity.

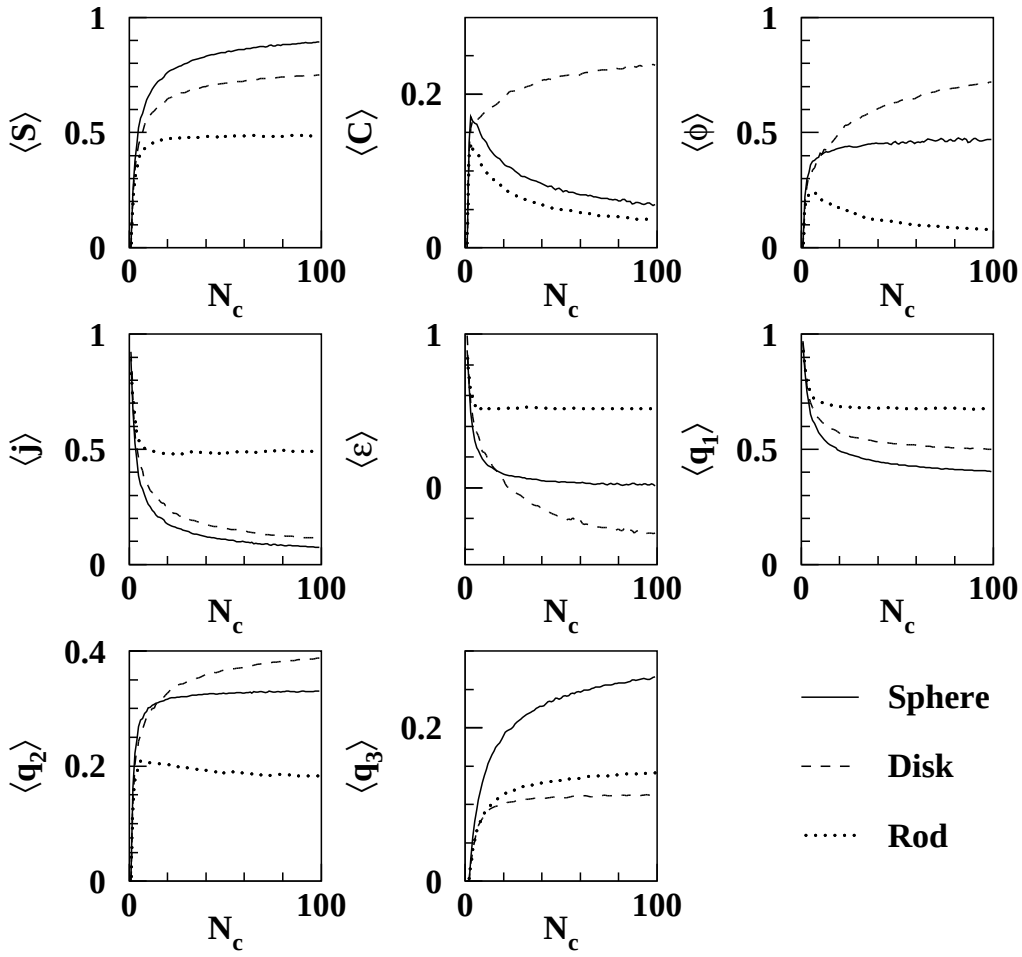

Figure 4.9: Same as Figure 4.8, except plotted versus total charged particle multiplicity, allowing extended (asymptotic) multiplicity scale.

both well-known and well-behaved (meaning that it does not show the second type of multiplicity distortion).

We have calculated the mean sphericity of central events in the experimental data, sorting them by IMF multiplicity, and compared the mean values to those obtained from the simulations in Figure 4.10. If we focus momentarily on the mean sphericity values obtained for IMF multiplicity 5, which is the mean multiplicity for these events (see Figure 4.2), then we can see an interesting energy progression. At low energies, the experimental data (solid lines) lie between the spherical (dashed) and disk (dot-dashed) values. This is also the case at high energies. However, at an intermediate energy of 60 MeV/nucleon, the experimental values are nearer to the disk values. This same basic trend is furthermore observed for all multiplicities $N_{imf} \geq 4$.

To clarify this trend, we have calculated the mean values of the sphericity of IMF emission and plotted these (markers) versus the incident beam energy per nucleon for three representative IMF multiplicities ($N_{imf} = 4, 5, 7$) in Figure 4.11. We have also plotted the mean values resulting from spherical (dotted lines) and disk-like (dot-dashed lines) emission patterns above and below each of these three multiplicity curves. Statistical errors on the mean values are smaller than the marker size and systematic errors are shown. The suppression of the sphericity value at 60 MeV/nucleon is now clear, and occurs for all IMF multiplicities shown, and those not shown ($N_{imf} \geq 4$) as well.

It is worthwhile to note two features of the filtered simulation data. First, the sphericity values resulting from the disk-like simulation are lower than those resulting from the spherical simulation. These lower values illustrate the effectiveness of sphericity in quantitatively distinguishing disk-like emission from spherical emission. Second, an examination of the excitation function of the sphericity values yielded by

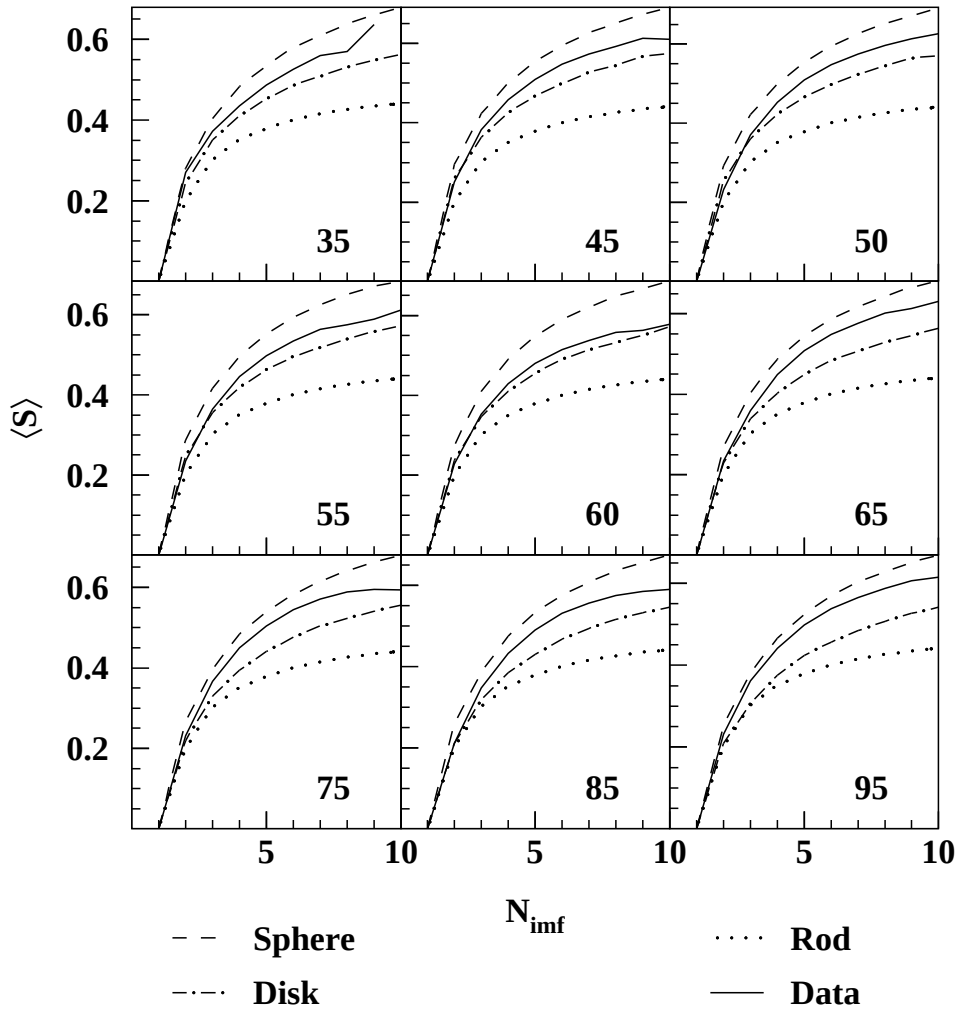

Figure 4.10: Mean values of sphericity extracted for spherical (dashed), disklike (dot-dashed) and rodlike (dotted) filtered simulations compared to those extracted from the experimental data (solid) for all beam energies, as labelled.

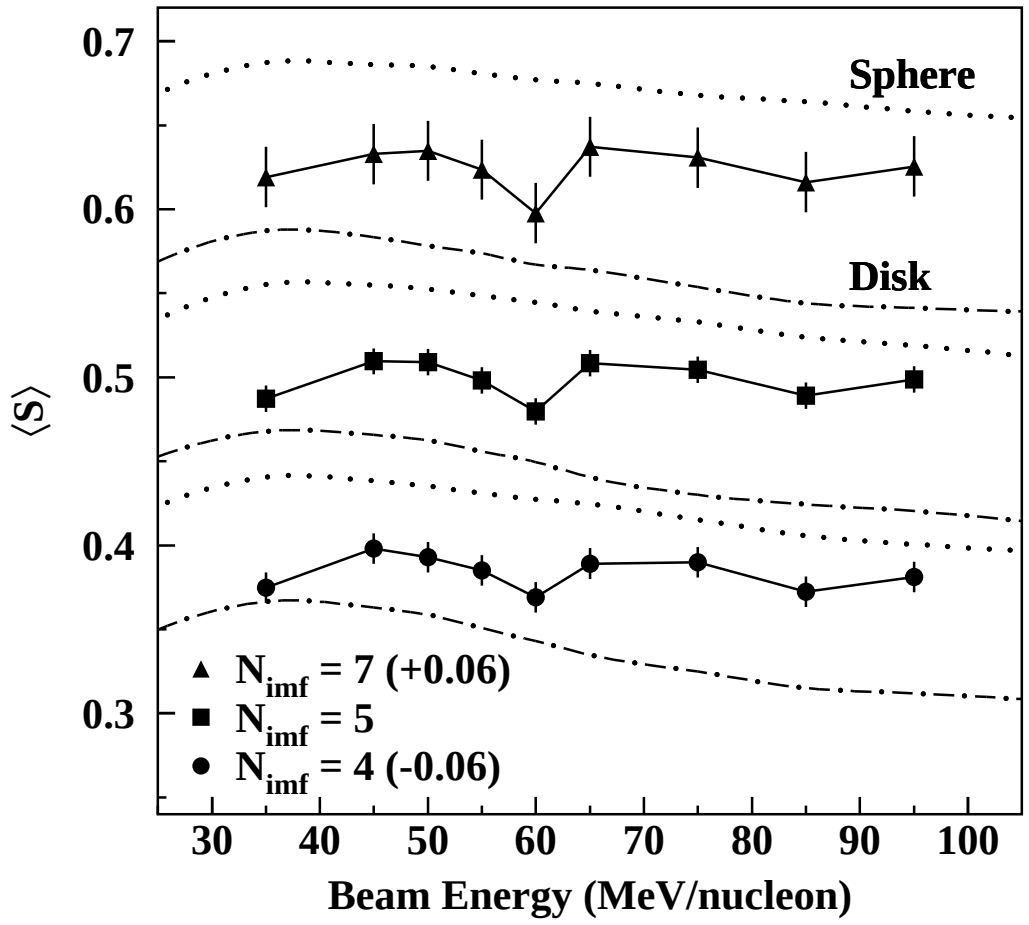

Figure 4.11: Measured values of the mean sphericity of IMF emission (markers) versus the incident beam energy for three representative IMF multiplicities, as labelled. The dotted (dot-dashed) lines in each case indicate the mean values obtained for filtered spherical (disk-like) simulations. Small offsets have been added for clarity.

the filtered simulation reveals that changes in the acceptance effects upon $\langle S \rangle$ with increasing beam energy are smooth, so that any significant change in the experimental data that does not follow this smooth trend cannot be attributed to systematic changes in acceptance.

Over the range of beam energies measured, the experimental values of sphericity fall between the limiting values obtained for the spherical and disk-like simulations, and the shape of the curves for each multiplicity reflect the same basic trends which we associate with acceptance effects. However, at a beam energy of 60 MeV/nucleon, the experimental value of $\langle S \rangle$ is suppressed, approaching the disk-like values. This suppression cannot be attributed to experimental acceptance and is beyond statistical fluctuations, and indicates a more disk-like, or coplanar, IMF emission at this energy. To be more quantitative, the value of sphericity achieved at 60 MeV/nucleon is consistent with a disk of aspect ratio 2:2:1. For completeness, we have calculated the mean values for each of the other shape variables and have scaled the values to allow placing them on the same plot. The resulting scaled values, extracted for an IMF multiplicity of 5, are shown in Figure 4.12. Despite the multiplicity distortions shown in Figures 4.8 and 4.9, the trends shown in the other event shape observables are quite similar to those observed for the sphericity.

Early studies involving the flow tensor[Gyul82] quantified the collective flow of the system in terms of "flow angles," the azimuthal angles of the three principle axes of the ellipsoid in momentum space. Thus, we can not only gain information from the eigenvalues, which we have done in the preceeding pages, we can also gain information from the eigenvectors. If the formation of a toroid were the cause of the increased coplanar emission of IMFs indicated by the event shapes analysis, then the one might expect to see a shift in the flow angles as well. (The toroidal and disk-like configurations shown in Figures 1.6 and 1.8 were formed perpendicular to the beam

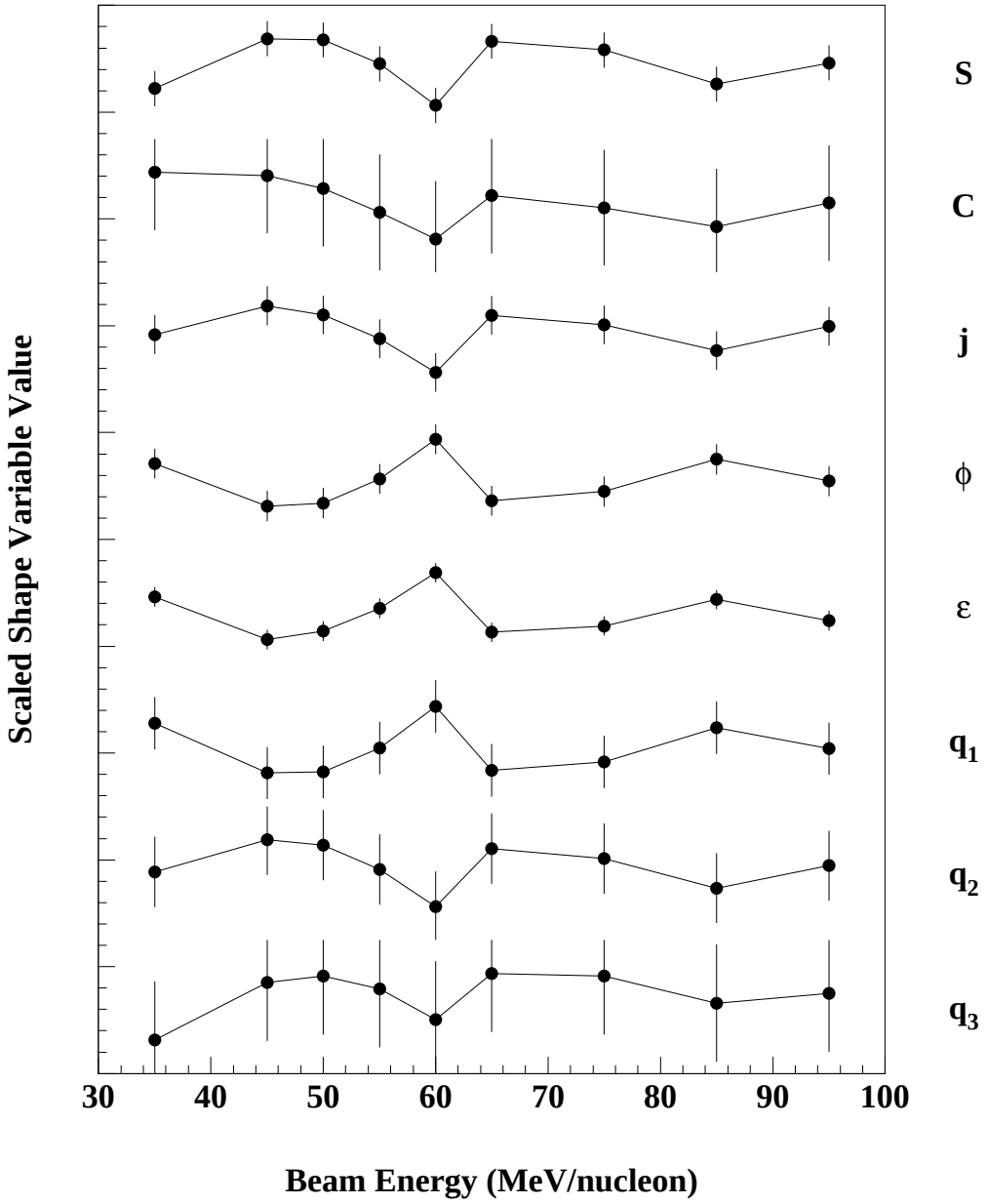

Figure 4.12: Scaled values of all eight shape-variables (as labelled at right) for IMF multiplicity 5. This reveals the suppression or enhancement of the all shape variables at 60 MeV/nucleon.

axis.) So we can examine the flow angles for the experimental data to determine whether there is a shift in the alignment of the major axis of the flow tensor. We have calculated the mean values of the cosines of the three flow angles (θ_1, θ_2, θ_3) corresponding to the three reduced eigenvalues (q_1, q_2, q_3) and plotted them versus the beam energy in Figure 4.13. The largest eigenvector also has the largest cosine of its flow angle, thus the momentum ellipsoid is pointing mostly forward. However, at 65 and 75 MeV/nucleon, the major axis shifts slightly toward smaller cosine values, indicating a shift toward a more perpendicular alignment. The shift is small, but it does move in a direction consistent with the scenario discussed above.

The suppression in the mean sphericity value observed for all IMF multiplicities is indicative of a transition to more two-dimensional emission of fragments. Increased coplanar emission of large fragments has been suggested as an additional consequence of toroid formation specifically[Xu93]. Having established the non-compact nature of the breakup geometry through the use of the previously shown charge signatures, and the two-dimensional nature of the fragment emission, toroidal break-up is a current scenario which can explain the anomalous behavior shown in all three observables presented. The fact that all three of these signatures appear and then vanish rather abruptly supports related predictions that the occurrence of non-compact geometries has a sensitive dependence upon the initial conditions of formation[More92, Baue92].

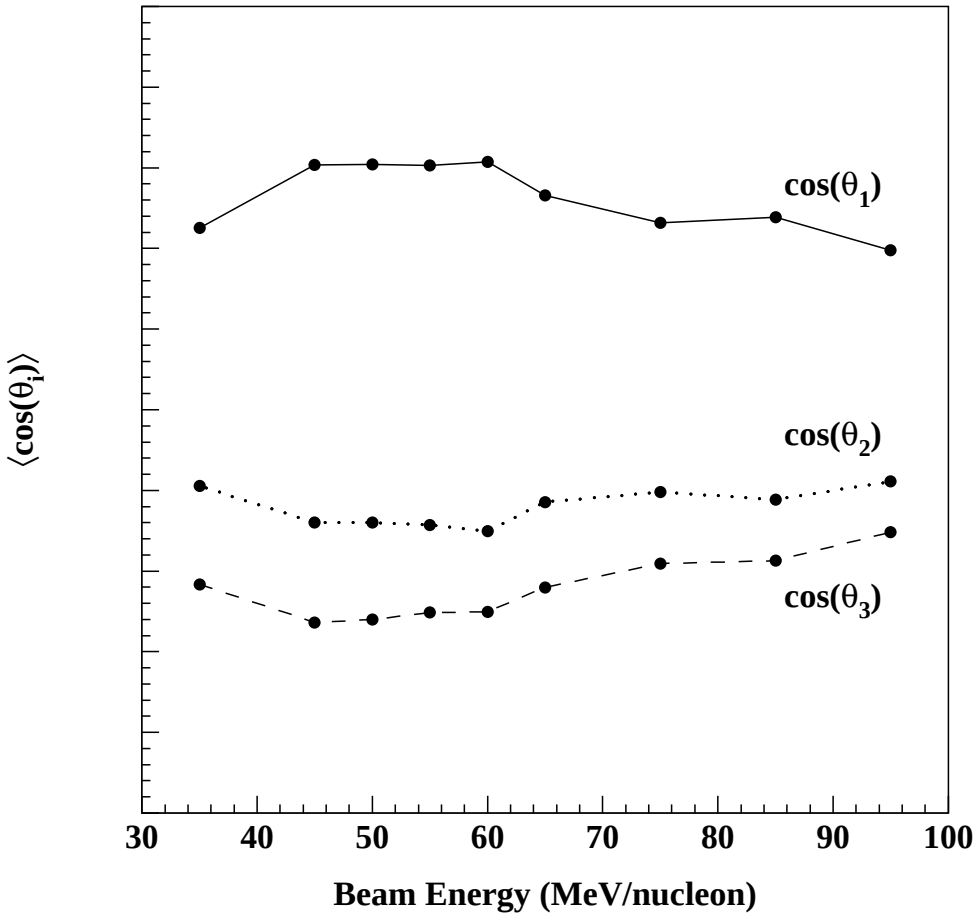

Figure 4.13: Cosine values of the azimuthal angles (termed the "flow angles") of the three eigen-vectors of the kinetic energy tensor, plotted versus the incident beam energy.

Chapter 5

Conclusion

In Chapter 3 we described a method of evaluating the importance of the specific disassembly mechanisms in a comprehensive set of central heavy-ion reactions using charge Dalitz plots. Small impact parameter collisions were selected using two-dimensional cuts on centrality variables that do not autocorrelate with the relative charge distributions. The observables D_{cent} and D_{edge} were introduced for the purpose of quantifying the distribution of events in the charge Dalitz triangles for each reaction. The constraints imposed on these observables, by definition and by the inefficiencies in the detection system, were shown not to affect our conclusions. Transitions from sequential binary disassembly to multifragmentation were observed in the central ^{40}Ar+^{45}Sc and ^{129}Xe+^{139}La entrance channels at beam energies of ~50 and ~30 MeV/nucleon, respectively. The results for the central ^{20}Ne+^{27}Al (^{87}Kr+^{93}Nb) reactions are consistent with the trends noted for the central ^{40}Ar+^{45}Sc(^{129}Xe+^{139}La) reactions over a more limited range of available beam energies.

In Chapter 4 we presented a systematic study of three global experimental observables for the ^{86}Kr+^{93}Nb system for incident energies ranging from 35 to 95 MeV/nucleon. Our study reveals enhanced emission of intermediate-mass fragments (IMFs) and a suppression in the power-law exponent α of ordered Z distributions,

which together establish the non-compact nature of the break-up geometry. We also observe a suppression in the mean value of the sphericity of IMF emission, which indicates toroidal, as opposed to bubble-like, geometries. All three of these signatures occur at energies between 60 and 75 MeV/nucleon. These signatures are predicted by many of the same theoretical models that have provided us with the most recent descriptions of non-compact geometries, and should be interpreted in that context as experimental evidence for the existence of toroidal break-up geometries.

We have established two basic changes in the reaction mechanisms for the systems studied. The first is the transition from sequential binary decay to multifragmentation in the incident beam energy range of 30 to 50 MeV/nucleon, for the systems studied. Second, we have shown that with increasing energy, the system evolves from a state in which a brief expansion is followed by a collapse, through an intermediate state in which the initial expansion stalls, to a state in which the expansion continues unabated. The stall in the expansion of the system studied has been related to the creation of exotic geometries. Previous theoretical work has already indicated that these exotic geometries will be subject to different decay modes. Further theoretical work concerning these distinct effects will advance the understanding of nuclear matter and its equation of state.

APPENDICES

Appendix A

High Voltage Circuit Components

Following are lists of the components used in the high voltage circuits shown in figure 2.6.

Label	Part	Quantity	Vendor (part #)
Re1, Re2	20MΩ, 1/2 W res.	2	Mouser (29SJ500-20M)
Rb1, Rb2	10kΩ, 1/2 W res.	2	Mouser (29SJ500-10K)
Ra1 - Ra8	100Ω, 1/4 W res.	8	Mouser (29SJ250-100)
Ca1 - Ca8	1nF, 3kV cap.	8	Newark (46F5277)
Cc1	10nF, 3kV cap.	1	Newark (95F4048)
P1	14 pin IDC socket	1	
P2	PMT Socket	1	
P3	SHV Connector	1	
P4	BNC Connector	1	
Hardware Components			
	PC Board	1	Hughes
	1" Spacer (4/40 thread)	3	DigiKey (8440GK-ND)
	5/16" Screw (4/40 thread)	6	DigiKey (H143-ND)
	PMT Base Cover	1	Classic Precision

Table A.1: List of Components for PMT socket.

Label	Part	Quantity	Vendor (part #)
Rd1 - Rd3	1MΩ, 1/2 W res.	3	Mouser (29SJ500-1M)
R1 - R3	43kΩ, 1 W res.	3	Mouser (261-43K)
R4 - R6	82kΩ, 1 W res.	3	Mouser (261-82K)
R7, R8	100kΩ, 1 W res.	2	Mouser (261-100K)
R9	130kΩ, 1 W res.	1	Mouser (261-130K)
R10	180kΩ, 1 W res.	1	Mouser (261-180K)
R11	150kΩ, 1 W res.	1	Mouser (261-150K)
R12	220kΩ, 1 W res.	1	Mouser (261-220K)
R13	200kΩ, 1 W res.	1	Mouser (261-200K)
Ra1 - Ra8	100Ω, 1/4 W res.	8	Mouser (29SJ250-100)
Z1, Z2	100V Transorb	2	DigiKey (P6KE100CACT-ND)
Z3	150V Transorb	1	DigiKey (P6KE150CACT-ND)
Za1 - Za8	15V Zener Diode	8	DigiKey (IN5245B)
Va1 - Va8	360V Varistor	8	DigiKey (P7243-ND)
Qa1 - Qa8	E-HexFET	8	DigiKey (IRF820-ND)
P1	14 pin IDC docket	1	DigiKey (MHD14G-ND)
Hardware Components			
	PC Board	1	Hughes
	Pomona Box	1	Newark (35F3520)

Table A.2: List of Components for the PMT divider.

Appendix B

Centrality Selection

The importance of centrality selection in experimental nuclear physics has been well established in previous studies[Phai92, Ogil89, Cava90] and merits careful consideration in this study as well. Of primary importance is the effective selection of central collisions from among the inclusive data in such a way as not to bias the sample of events. Several global observables have been shown in the cited studies to correlate to the impact parameter (b) in nuclear collisions. We have chosen to consider the following five variables from among the list of known centrality variables:

- The total number of detected charged particles (N_c).
- The total number of detected protons (N_p).
- The total charge of light charged particles (Z_{lcp}).
- The total transverse kinetic energy ($E_t = \sum_{i=1,N_c} E_i \sin(\theta_i)$), where E_i and θ_i are the kinetic energy and polar angle of each detected fragment.
- The total charge of fragments travelling at mid-rapidity ($Z_{mr} = \sum_{i,0.75Y'_{targ}<Y'_{frag,i}<0.75Y'_{proj}} Z_i$), where Y'_{targ}, $Y'_{frag,i}$, and Y'_{proj} are the center-of-momentum frame rapidities of the target, emitted fragments, and projectile, respectively.

In defining this subset, we have attempted to choose well known, reliable and simple observables, in order to minimize the number of unknown effects in the analysis.

B.1 Numerical Calculations

The application of a centrality observable is based on the simple geometric concept that the scalar value of the impact parameter is monotonically related to the value of a centrality variable by the relation[Cava90]

$$\frac{2\pi b \mathrm{d}b}{\pi b_{max}^2} = f(q)\mathrm{d}q$$

where f(q) is the probability of measuring an event with centrality variable value q. This can then be integrated to yield the relation between the value of the reduced impact parameter (b/b_{max}) and the integrated probability as a function of the centrality variable

$$b/b_{max} = \sqrt{1 - F(Q)} \tag{B.1}$$

where $F(Q) = \int_{Q_{central}}^{Q} f(q)\mathrm{d}q$, and b_{max} is the maximum impact parameter leading to a triggered event. In this strict geometrical picture, $b_{max} = (R_{proj} + R_{targ})$, where R_{proj} (R_{targ}) is the radius of the projectile (target) and can be approximated by $R = r_0 A^{1/3}$[Cava90].

For example, in Figure B.1 we show the probability distributions of two centrality variables E_t and Z_{mr} (unshaded histograms) for the ^{40}Ar+^{45}Sc system at 95 MeV/nucleon incident energy. The horizontally (vertically) shaded sections show the subsets selected by 10% cuts on Z_{mr} (E_t) alone. From the relation given above, a 10% cut corresponds to a reduced E_t value of a reduced impact parameter of

$$b/b_{max} = \sqrt{1 - 0.9} = 0.31$$

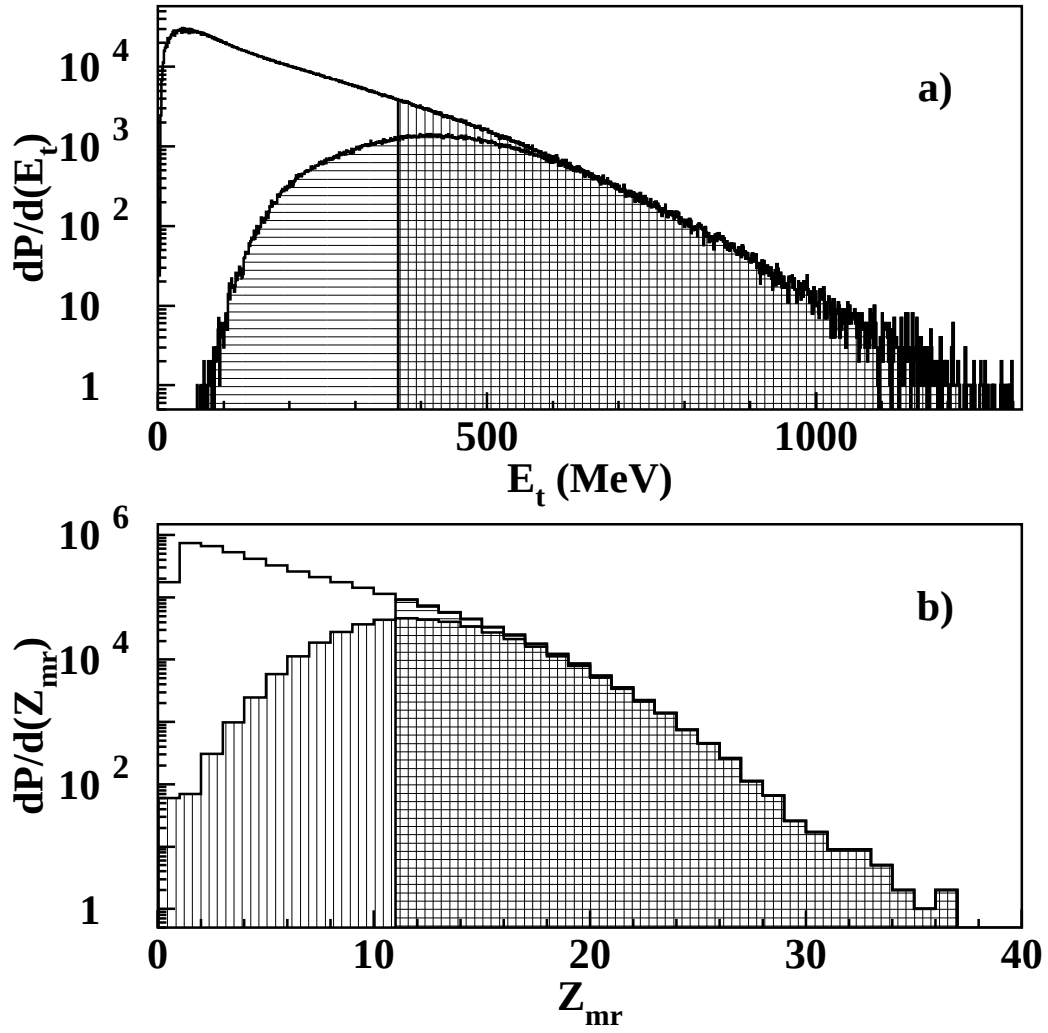

Figure B.1: Two centrality variable distributions for (a) E_t and (b) Z_{mr} (see text for definitions). The unshaded histogram shows the inclusive distribution for System-2 (see text) events, while the horizontally (vertically) shaded sections show the subsets selected by 10% cuts on Z_{mr} (E_t) alone. The intersection of these two subsets shows the portion of the inclusive data selected by simultaneous 10% cuts on both of these variables (roughly 7%).

so that events above this 10% threshold have a value of the impact parameter

$$b \leq 0.31(1.2\text{fm})(40^{1/3} + 45^{1/3}) \leq 2.5\text{fm} \ .$$

B.2 Autocorrelations

Efficiency is not the only consideration when choosing a centrality variable. We need to verify also that the centrality variable we choose is not autocorrelated to the observables in our study. An autocorrelation is a correlation between the centrality variable and the experimental observable which is inherent in the definition of the observable. A trivial example of an autocorrelation is between the number of charged particles (N_c) and itself. Other similar, but more subtle, autocorrelations are between N_c and the number of intermediate-mass fragments (IMFs), the number of light charged particles, or the number of protons detected, the common thread between all of these latter observables being a number of particles.

Autocorrelations are not always so obvious as those stated in the above examples, and they must be thoroughly investigated before any serious analysis is performed. In order to identify autocorrelations, we rely on the fact that the width of the distribution of values for an experimental observable will be narrower when selected by an autocorrelated centrality variable. Consider our trivial example again; if we make a very narrow cut on the centrality variable N_c, then the distribution of N_c (or N_{imf}, etc.) values will be correspondingly narrow. Intuitively, one should expect that observable distributions selected via centrality cuts will become more narrow, as compared to inclusive distributions, by virtue of the selection of a well-characterized subset of events. In this light, the separation between autocorrelated and non-autocorrelated centrality variables based on the observed widths, as described, becomes one of a relative suppression of the widths.

Since the analysis in Chapter 3 is an analysis of the three largest charges in each event, we have examined the effects of cuts on the five centrality variables listed above on the sizes and RMS widths of the distributions of these charges (Z_1, Z_2, Z_3). We have plotted the RMS widths for these three charges versus the incident beam energy for 5% cuts in the ^{40}Ar+^{45}Sc system (Fig. B.2). The corresponding mean charge values are also plotted in Fig. B.3, for completeness. For each of the three charge widths measured, the widths resulting from cuts on Z_{lcp} are the most strongly suppressed for nearly all beam energies. The two centrality variables which cause the least suppression in the charge distributions are E_t and Z_{mr}. Similar suppression of widths was observed for D_{cent} and D_{edge}, although not as pronounced. For this reason, centrality cuts for the study in Chapter 3 will be performed on these two variables.

In general, the correlation between any given centrality variable and the impact parameter (b) is not a perfect correlation, *i.e.* it has some non-zero width due to fluctuations, as mentioned above. To minimize the effects of these fluctuations upon the determination of centrality, we will perform two-dimensional cuts to select the central events we will study in Chapter 3. Specifically, we will require that events have values of both E_t and Z_{mr} which fall in the top 10% of the respective distributions simultaneously. This is illustrated in Figure B.1 by the intersection of the vertically and horizontally shaded areas (which represent the one-dimensional cuts) into the hatched area in each panel. This region includes roughly the top 4-8% of the total inclusive data.

A similar analysis was performed to select E_t as the centrality variable for the charge-based observables shown in Chapter 4 and Z_{mr} as the centrality variable for the energy/momentum based observables in that chapter.

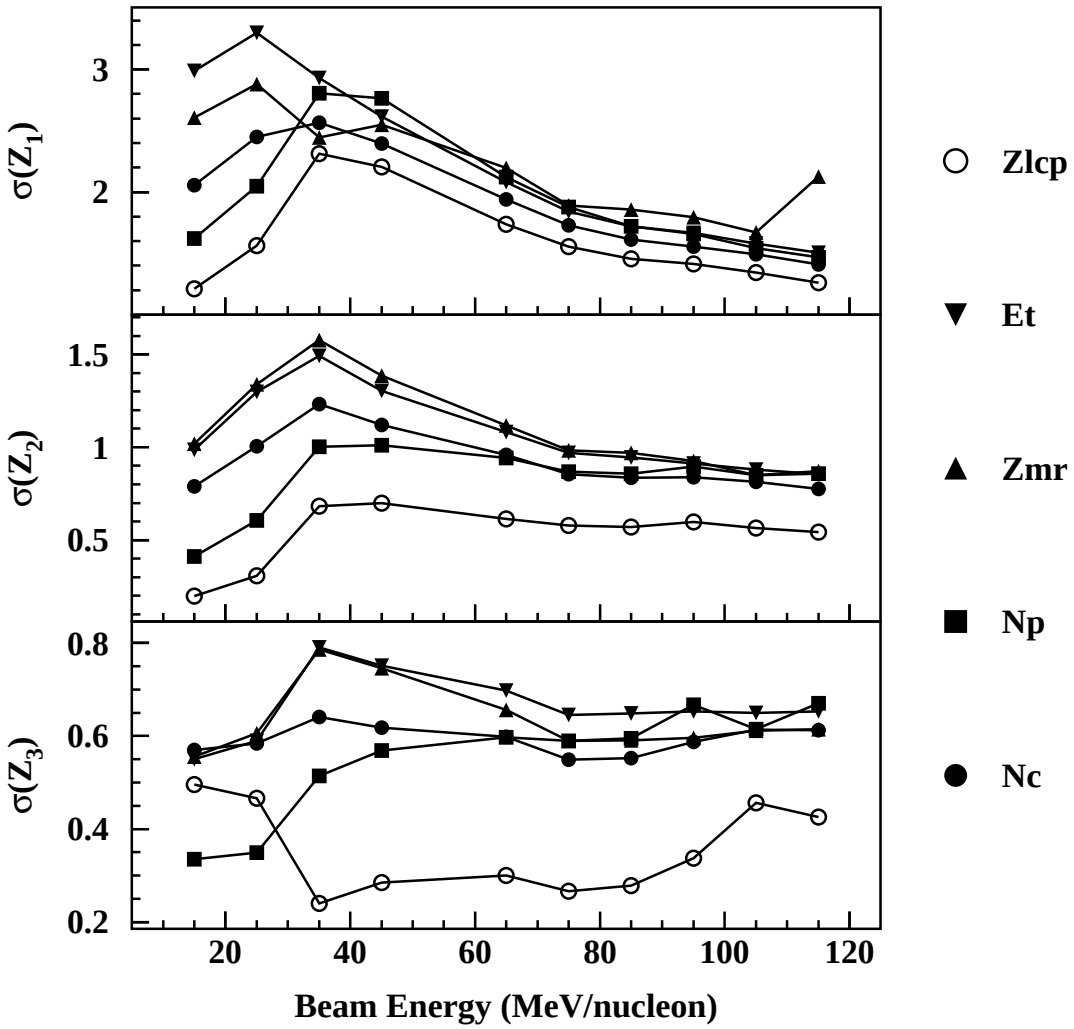

Figure B.2: RMS widths of the charge distributions of first, second and third largest fragments in central events in the ^{40}Ar+^{45}Sc system selected by 5% cuts on 5 centrality variables (as labelled).

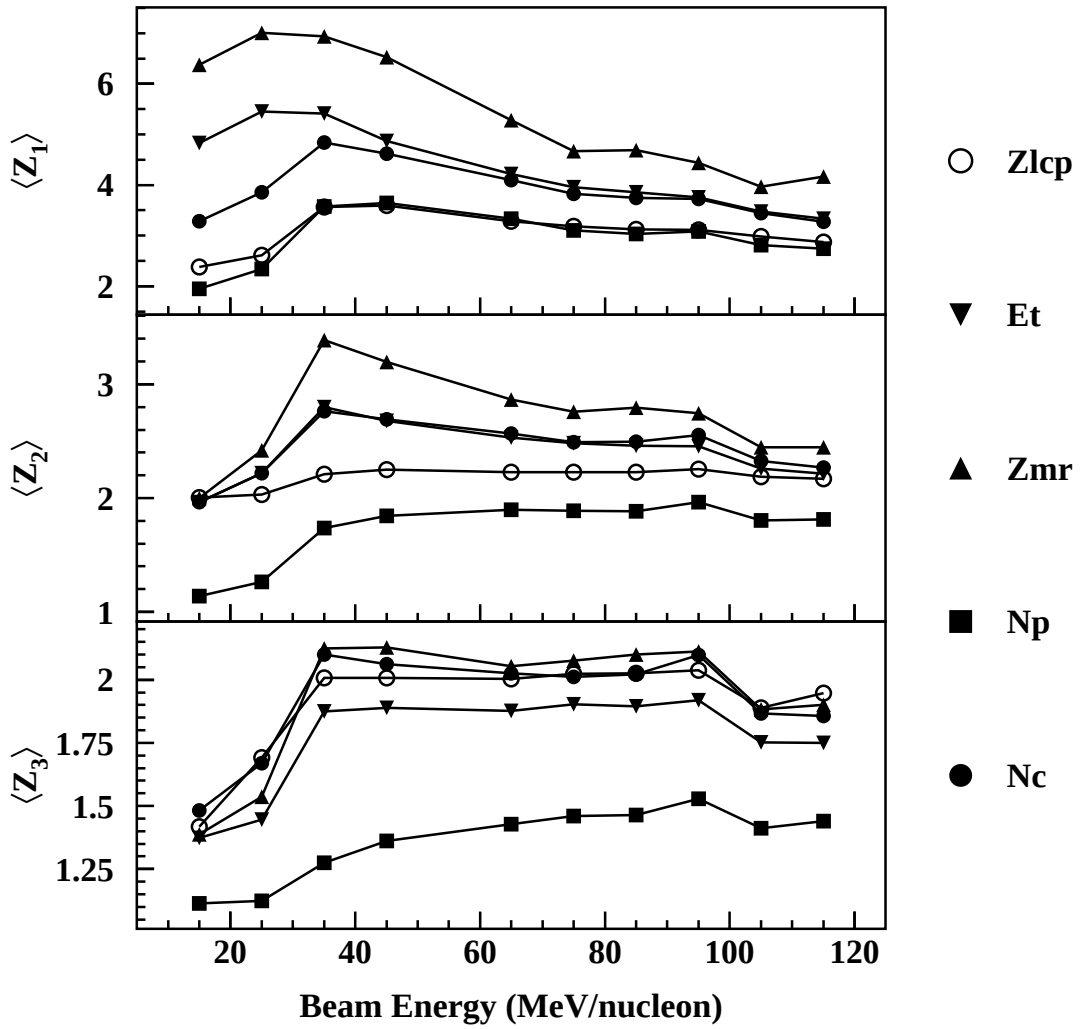

Figure B.3: Mean charge of the first, second and third largest fragments in central events in the ^{40}Ar+^{45}Sc system selected by 5% cuts on 5 centrality variables (as labelled).

Appendix C

Simulation Parameter Definitions

We have generated simulated events having well-defined momentum-space distributions (see Figure 4.7). The purpose of generating events in this thesis is twofold: (1) to compare the overall magnitudes of the extracted event shape observables to the experimentally measured values and (2) to elucidate how measured values are affected by the detector apparatus itself. In order to achieve either of these goals, it is necessary to filter the generated events. All simulation data shown in this thesis has been generated by the code EGSIM and subsequently passed through a software replica of the 4π detector. This event filter accounted for particle loss due to effects such as upper and lower energy thresholds, uncovered solid angle, malfunctioning detectors, target shadowing and multiple particle hits in the same detector.

Before such a comparison can be made, particular care must be taken to ensure a meaningful event structure. In this Appendix, we shall detail the process by which we selected a set of input parameters for the event generator EGSIM[Gual95]. The workings of this event generator were based on a model described by the authors of Reference [Bond90]. The basic concept consists of the selection of momenta from a three-dimensional gaussian distribution, to fix the direction, and the selection of kinetic energies from a Maxwellian distribution, to fix the energy normalization.

Of particular value to the analysis of Chapter 4 is the ability that this generator provides the user to define the relative sizes of the axes of the momentum ellipsoid. It is these relative sizes, extracted from the kinetic energy tensor[Gyul82], that are used in an event shape analysis to define observables like Sphericity, Coplanarity, Prolateness, Eccentricity[Cugn83, Fai83, Lópe89], etc. In this way, one can define a particular event shape in momentum space and examine the effects of detector acceptance on the measurement of event shapes variables.

The four available input parameters are the relative sizes of the principle axes, the emission source temperature (or temperatures, if multiple sources are used), and the charge and charged particle multiplicity distributions. The aspect ratio used, as discussed, is the parameter which will be varied in the discussions of Chapter 4. A discussion of the determination of the others follows below.

C.1 Temperature

We base the selection of an emission source temperature on inverse-slope parameters extracted from fits of experimental data to Maxwell-Boltzmann distributions. The functional form is given by:

$$\frac{dP}{dE} = N\frac{P_{lab}}{P_{CM}}\sqrt{KE_{CM}}\exp\left(\frac{-KE_{CM}}{T}\right)$$

, where N is an overall normalization, P_{lab} (P_{CM}) is the lab- (CM-) frame momentum, KE_{CM} is the CM-frame fragment kinetic energy, and T is the source temperature. Since the analysis of Chapter 4 involves intermediate-mass fragments (IMFs) only, we have plotted kinetic energy (per nucleon) distributions for ^{7}Li, the smallest IMF, in Figure C.1. The histograms show the measured kinetic energy spectra, while the solid line superimposed on each frame is the χ^2 fit of the Maxwell-Boltzmann distribution to each histogram. The extracted kinetic temperatures are shown in Figure C.2. It

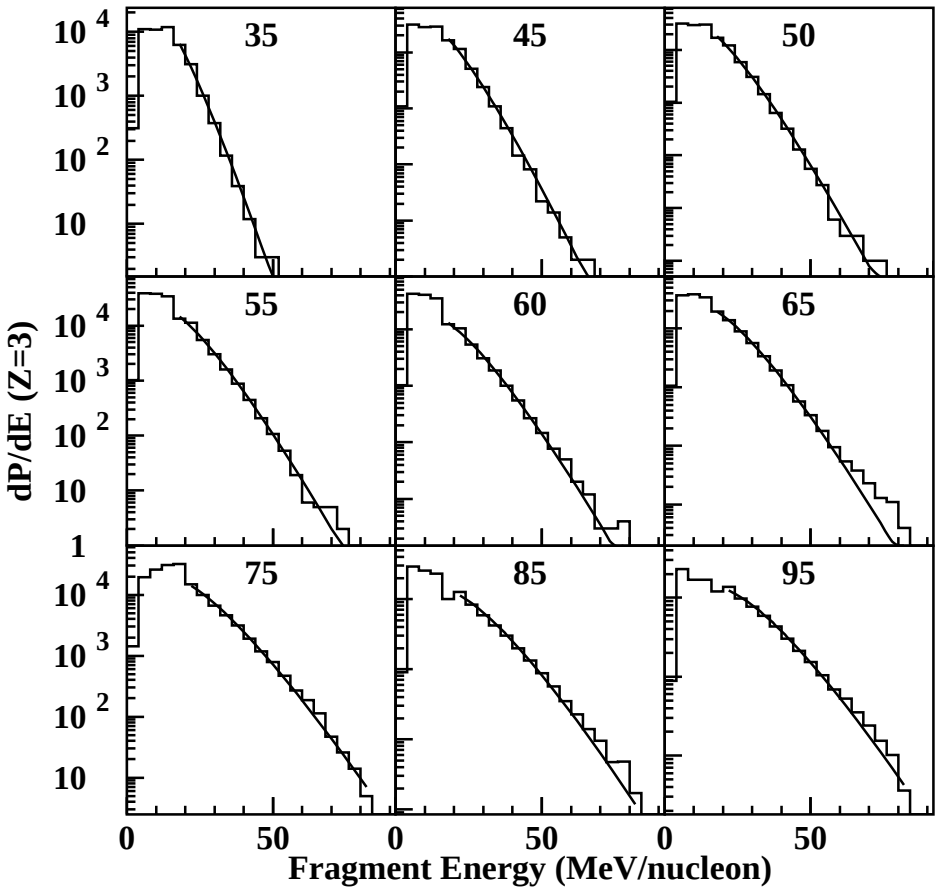

Figure C.1: Kinetic energy (per nucleon) spectra (histograms) for ^{7}Li fragments for each energy, as labelled. Each spectra has been fit with a Maxwell-Boltzmann distribution (solid line) in order to extract the emission source temperature.

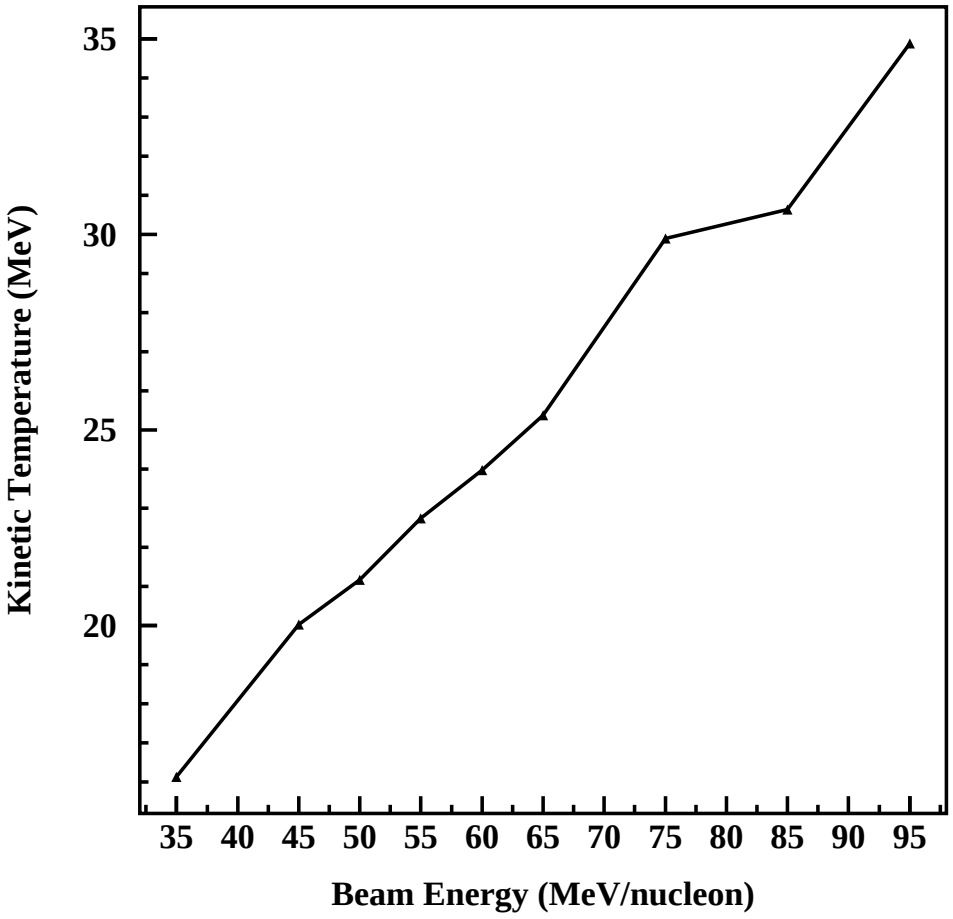

Figure C.2: Kinetic temperatures extracted from energy spectra for ^{7}Li fragments.

is these values which were used as the emission source temperatures for EGSIM.

C.2 Charge and Multiplicity Distributions

In order to reproduce the observed charge and multiplicity distributions, we adjusted the input parameters to the event generator and compared the filtered distributions those obtained by experiment. A distribution of the total charged particle multiplicity is shown in Figure C.3 for both the filtered simulation (top panel) and the experiment (bottom panel). Experimental distributions shown in this Appendix were taken from central collisions (see Appendix B) in a 65 MeV/nucleon ^{86}Kr+^{Nb} sample. Each of the distributions has been fit with a gaussian function, and the resulting fit parameters are shown in the upper right corner of each frame. For the input parameters chosen, the filtered simulation well-reproduces the multiplicities observed in the experiment. In a similar fashion, we show simulated and measured charge distributions for the same data sample in Figure C.4. The filtered simulation well-reproduces the observed charged distributions as well.

With these two sets of parameters defined, it is of interest to examine the resulting simulated IMF multiplicity spectrum. These are shown in Figure C.5 with the experimental distributions. These two have been fitted with gaussian distributions and the extracted parameters are shown in the upper right corner of each frame. Here, for the first time, the filtered simulation data do not quite reproduce the observed experimental distribution. The mean IMF multiplicity for the simulation is shifted with respect to the experimental value by roughly 3 units. Even with this enhanced IMF multiplicity in the simulation, we can compare the event shapes yielded in these events to those from experiment if we only compare events having the same IMF multiplicity. This constraint is already required in event shape analyses by virtue of

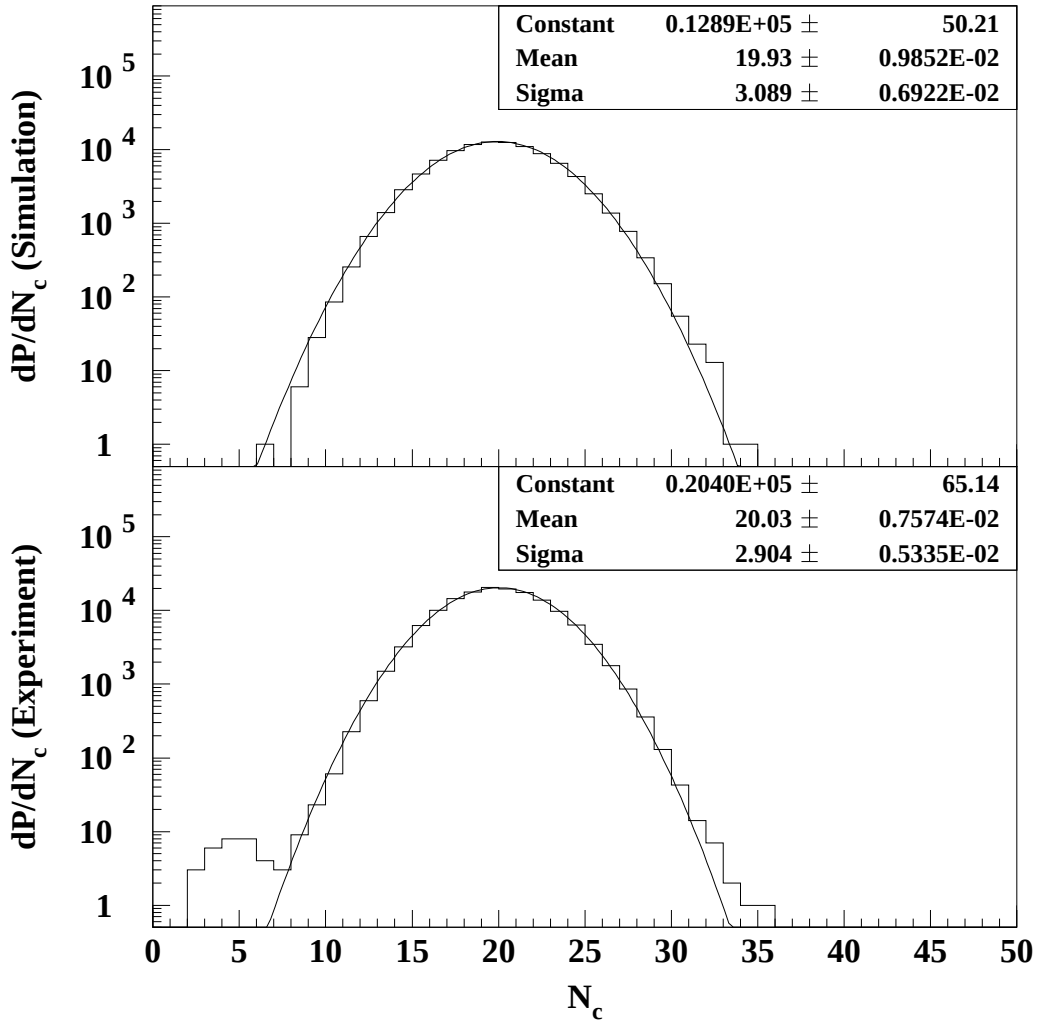

Figure C.3: Comparison of charged particle multiplicity distributions (histograms) generated by the simulation (top panel) and measured for central events in the experiment (bottom panel). Gaussian distributions have been fit to the data (solid lines) and fit parameters are shown in the upper right corner of each panel.

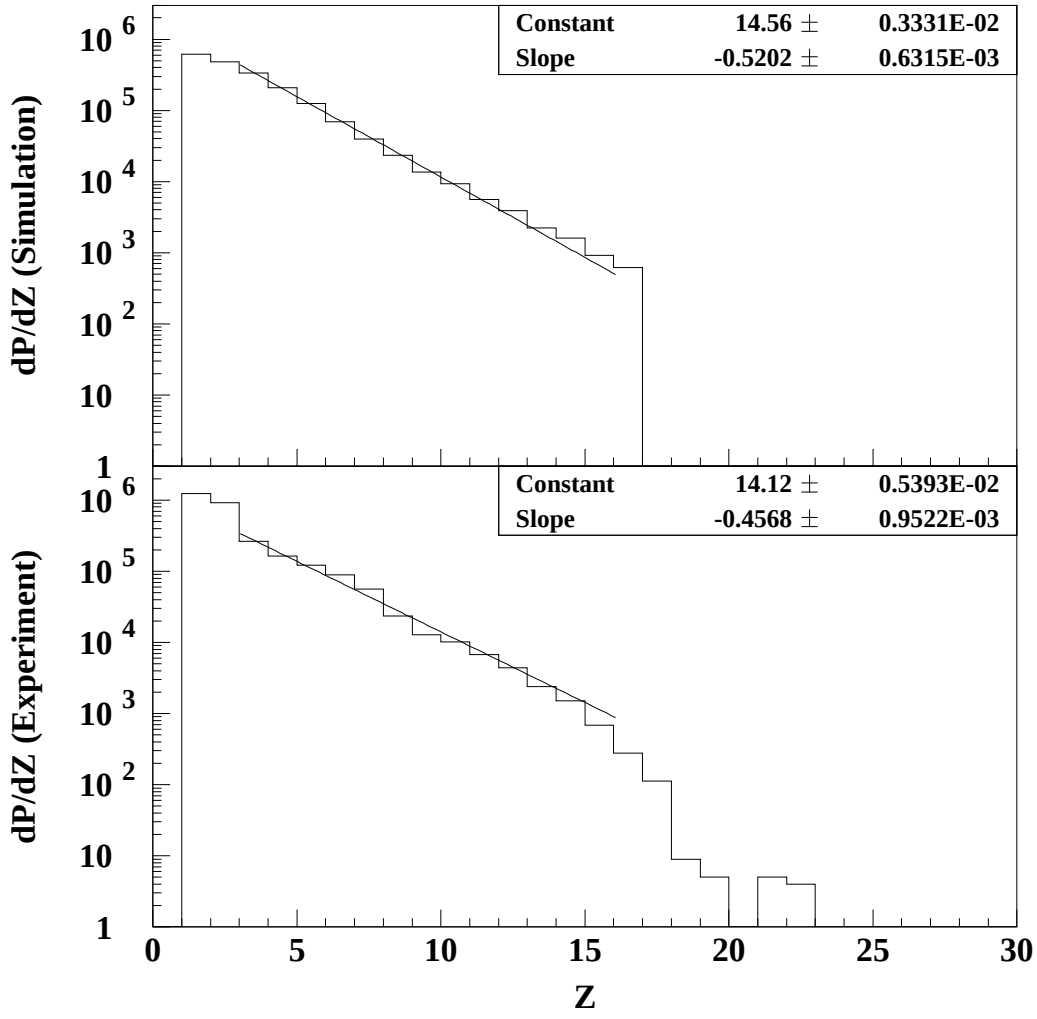

Figure C.4: Same as Figure C.3, except for charge distributions, fitted with exponential functions.

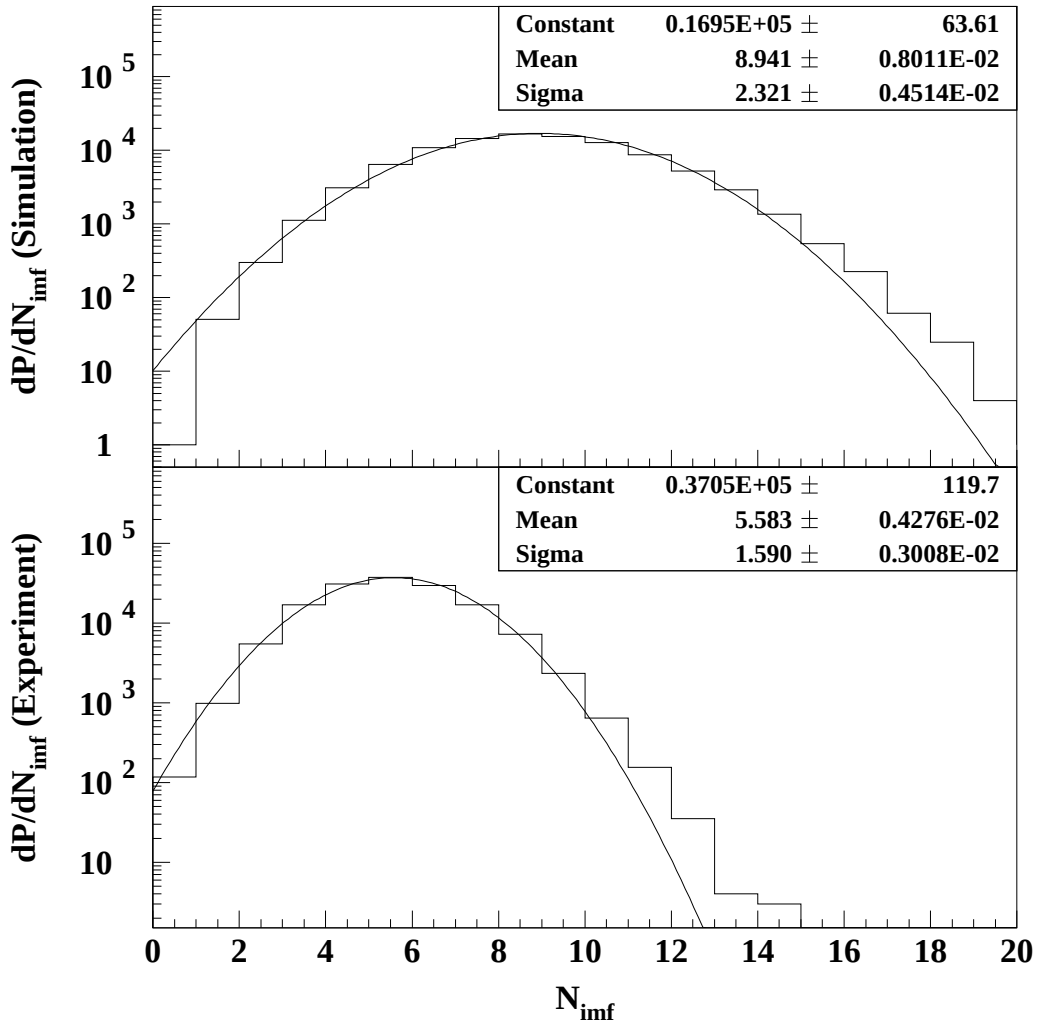

Figure C.5: Same as Figure C.3, except for IMF multiplicity distributions.

the low-multiplicity distortions to event shape observables[Fai83, Llop95b].

By the above methods, we have constrained the model input parameters relating to the emission source temperature and the charge and multiplicity distributions. In this way, we are now able to examine both the effects of varying the momentum space aspect ratio upon filtered simulation, and the detector acceptance effects upon the experimentally measured values.

BIBLIOGRAPHY

Bibliography

[Aich88] J. Aichelin, G. Peilert, A. Rosenhauer, H. Stöcker and W. Greiner, Phys. Rev. C **37**, 2451 (1988).

[Ayik90] S. Ayik and C. Gregoire, Nucl. Phys. **A513**, 187 (1990).

[Bada93] A.Badalà, R. Barbera, A. Palmeri, G.S. Pappalardo and F. Riggi, Phys. Rev. C **48** (1993).

[Barb86] C. Barbagallo, J. Richert, and P. Wagner, Z. Phys. A **324**, 97 (1986).

[Barz86] H.W. Barz, J.P. Bondorf, R. Donangelo, I.N. Mishustin and H. Schulz, Nucl. Phys. **A448**, 753 (1986).

[Baue88] W. Bauer, Phys. Rev. C **38**, 1297 (1988).

[Baue92] W. Bauer, G.F. Bertsch and H. Schulz, Phys. Rev. Lett. **69**, 1888 (1992).

[Baue95] W. Bauer and Alexander Botvina, Phys. Rev. C **52**, R1760 (1995).

[Bert88] G.F. Bertsch and S. das Gupta, Phys. Rep. **160**, 189 (1988).

[Birk64] J.B. Birks, *The Theory & Practice of Scintillation Counting* (Pergammon Press, New York, 1964).

[Biza93] G. Bizard, R. Bougault, R. Brou, J. Colin, D. Durand, A. Genoux-Lubain, J.L. Laville, C. Le Brun J.F. Lecolley, M. Louvel, J. Péter, J.C. Steckmeyer, B. Tamain, A. Badala, T. Motobayashi, G. Rudolf and L. Stuttgé, Phys. Lett. B **302**, 162 (1993).

[Bona92] A. Bonasera and F. Gulminelli, Phys. Lett. B **275**, 24 (1992).

[Bond85] J.P. Bondorf, R. Donangelo, I.N. Mishustin, C.J. Pethick, H.Schulz and K. Sneppen, Nucl. Phys. **A443**, 321 (1985).

[Bond90] J.P. Bondorf, C.H. Dasso, R. Donangelo and G. Pollarolo, Phys. Lett. B **240**, 28 (1990).

[Botv87] A.S. Botvina, A.S. Iljinov, I.N. Misustin, J.P. Bondorf, R. Donangelo and K. Sneppen, Nucl. Phys. **A475**, 663 (1987).

[Bowm92] D.R. Bowman, C.M. Mader, G.F. Peaslee, W. Bauer, N. Carlin, R.T. de Souza, C.K. Gelbke, W.G. Gong, Y.D. Kim, M.A. Lisa, W. G. Lynch, L.Phair, M.B. Tsang, C. Williams, N. Colonna, K. hanold, M.A. McMahan, G.J. Wozniak, L.G. Moretto and W.A. Friedman, Phys. Rev. C **46**, 1834 (1992).

[Camp88] X. Campi, Phys. Lett. **B208**, 351 (1988).

[Casi93] G. Casini, P.G. Bizzeti, P.R. Maurenzig, A. Olmi, A.A. Stefanini, J.P. Wessels, R.J. Charity, R. Freifelder, A. Gobbi, N. Herrmann, K.D. Hildenbrand and H. Stelzer, Phys. Rev. Lett. **71**, 2567 (1993).

[Cava90] C. Cavata, M. Demoulins, J. Gosset, M.-C. Lemaire, D. L'Hôte, J. Poitou and O. Valette, Phys. Rev. C **42**, 1760 (1990).

[Cebr90] D.A. Cebra, S. Howden, J. Karn, A. Nadasen, C.A. Ogilvie, A. Vander Molen, G.D. Westfall, W.K. Wilson, J.S. Winfield and E. Norbeck, Phys. Rev. Lett. **64**, 2246 (1990).

[Cebr91] D.A. Cebra, S. Howden, J. Karn, D. Kataria, M. Maier, A. Nadasen, C.A. Ogilvie, N. Stone, D. Swan, A. Vander Molen, W.K. Wilson, J.S. Winfield, J. Yurkon and G.D. Westfall, Nucl. Inst. and Meth. **A300**, 518 (1991).

[Cebr92] D. Cebra, W.K. Wilson, A. Vander Molen and G.D. Westfall, Nucl. Inst. Meth. **A313**, 367 (1992).

[Char88] R.J. Charity, M.A. McMahan, G.Z. Wozniak, R.J. McDonald, L.G. Moretto, D.G. Sarantites, L.G. Sobotka, G. Guarino, A. Pantaleo, L. Fiore, A. Gobbi and K.D. Hildenbrand, Nucl. Phys. **A483**, 371 (1988).

[Colo92] M. Colonna, P. Roussel-Chomaz, N. Colonna, M. Di Toro, L.G. Moretto and G.J. Wozniak, Phys. Lett. **B283**, 180 (1992).

[Cugn83] J. Cugnon and D. L'Hôte, Nuc. Phys. **A397**, 519 (1983).

[Dela86] H. Delagrange, C. Grégoire, F. Scheuter and Y. Abe, Z. Phys. A **323**, 437 (1986).

[Desb87] J. Desbois, Nucl. Phys. **A446**, 724 (1987).

[Dura96] D. Durand, J.F. Lecolley, M. Aboufirassi, R. Bougault, J. Colin, A. Genoux-Lubain, C. Le Brun, O. Lopez, M. Louvel, C. Meslin, G. Rudolf, L. Stuttgé and S. Tomasevic, LPC CAEN Preprint **LPCC96-02**, Submitted to Phys. Lett. (1996).

[Elli94] J.B. Elliott, M.L. Gilkes, J.A. Hauger, A.S. Hirsch, E. Hjort, N.T. Porile, R.P. Scharenberg, B.K. Srivastava, M.L. Tincknell and P. Warren, Phys. Rev. C **49**, 3185 (1994).

[Fai83] G. Fai and J. Randrup, Nuc. Phys. **A404**, 551 (1983).

[Finn82] J.E. Finn, S. Agarwal, A. Bujak, J. Chuang, L.J. Gutay, A.S. Hirsch, R.W. Minich, N.T. Porile, R.P. Scharenberg, B.C. Stringfellow and F. Turkot, Phys. Rev. Lett. **49**, 1321 (1982).

[Fish67] M.E. Fisher, Physics (Long Island City, NY) **3**, 255 (1967).

[Frie88] W. Friedman, Phys. Rev. Lett. **60**, 2125 (1988).

[Frie90] W. Friedman, Phys. Rev. C **42**, 667 (1990).

[Gilk94] M.L. Gilkes, S. Albergo, F. Bieser, F.P. Brandy, Z. Caccia, D.A. Cebra, A.D. Chacon, J.L. Chance, Y. Choi, S. Costa, J.B. Elliott, J.A. Hauger, A.S. Hirsch, E.L. Hjort, A. Insolia, M. Justice, D. Keane, J.C. Kintner, V. Lindenstruth, M.A. Lisa, U. Lynen, H.S. Matis, M. McMahan, C. McParland, W.F.J. Müller, D.L. Olson, M.D. Partlan, N.T. Porile, R. Potenza, G. Rai, J. Rasmussen, H.G. Ritter, J. Romanski, J.L. Romero, G.V. Russo, H. Sann, R. Scharenbert, A. Scott, Y. Shao, B.K. Srivastaba, T.J.M. Symons, M. Tincknell, C. Tuvé, S. Wang, P. Warren, H.H. Wieman and K. Wolf, Phys. Rev. Lett, **73**, 1590 (1994).

[Glas93] T. Glasmacher, C. Gelbke and S. Pratt, Phys. Lett. B **314**, 265 (1993).

[Good84] A.L. Goodman, J.I. Kapusta and A.Z. Mekjian, Phys. Rev. C **30**, 851 (1984).

[Gros87] D.H.E. Gross and H. Massmann, Nucl. Phys. **A471**, 339c (1987).

[Gros92] D.H.E. Gross, B.A. Li and A.R. DeAngelis, Ann. Phys. **1**, 467 (1992).

[Gros93] D.H.E. Gross, Prog. Part. Nucl. Phys. **30**, 155 (1993).

[Gual95] E.E. Gualtieri, Ph.D. Dissertation, Michigan State University, 1995 (Unpublished).

[Guar95] A. Guarnera, B. Jacquot, P. Chomaz and M. Colonna, GANIL Preprint **P95-05** (1995).

[Gutb91] H. Gutbrod and H. Stöcker, Scientific Amarican **265**(5), 58 (1991).

[Gyul82] M. Gyulassy, K.A. Frankel and H. Stöcker, Phys. Lett. B **110**, 185 (1982).

[Hage92] K. Hagel, M. Gonin, R. Wada, J.B. Natowitz, B.H. Sa, Y. Lou, M. Gui, D. Utley, G. Nebbia, D. Fabris, G. Prete, J. Ruiz, D. Drain, B. Chambon, B. Cheynis, D. Guinet, X.C. Hu, A. Demeyer, C. Pastor, A. Giorni, A. Lleres, P. Stassi, J.B. Viano, P. Gonthier, Phys. Rev. Lett. **68**, 2141 (1992).

[Hirs84] A.S. Hirsch, A. Bujak, J.E. Finn, L.J. Gutay, R.W. Minich, N.T. Porile, R.P. Scharenbert, B.C. STringfellow and F. Turkot, Phys. Rev. C **29**, 508 (1984).

[Kreu93] P. Kreutz, J.C. Adloff, M. Begemann-Blaich, P. Bouissou, J. Hubele, G. Imme, I. Iori, G.J. Kunde, S. Leray, V. Lindenstruth, Z. Liu, U. Lynen, R.J. Meijer, U. Milkau, A. Moroni, W.F.J. Müller, C. Ngô, C.A. Ogilvie, J. Pochadzalla, G. Raciti, G. Rudolf, H. Sann, A. Schüttauf, W. Seidel, L. Stuttgé, W. Trautmann and A. Tucholski, Nucl. Phys. **A556**, 672 (1993).

[Li93] T. Li, W. Bauer, D. Craig, M. Cronqvist, E. Gualtieri, S. Hannuschke, R. Lacey, W.J. Llope, T. Reposeur, A.M. Vander Molen, G.D. Westfall, W.K. Wilson, J.S. Winfield, J. Yee, S.J. Yennello, A. Nadasen, R.S. Tickle and E. Norbeck, Phys. Rev. Lett. **70**, 1924 (1993).

[Llop92] W.J. Llope, R. Pedroni, R. Pak, G.D. Westfall, J. Wagner, A. Mignerey, D. Russ, J. Shea, H. Madani, R.A. Lacey, D. Craig, E. Gualtieri, S. Hannuschke, T. Li, J. Yee and E. Norbeck, NSCL Annual Report, 236 (1992).

[Llop95a] W.J. Llope, J.A. Conrad, C.M. Mader, G. Peilert, W. Bauer, D. Craig, E. Gualtieri, S. Hannuschke, R.A. Lacey, J. Lauret, T. Li, A. Nadasen, E. Norbeck. R. Pak, N.T.B. Stone, A.M. Vander Molen, G.D. Westfall, J. Yee and S.J. Yennello, Phys. Rev. C **51**, 1325 (1995).

[Llop95b] W.J. Llope, W. Bauer, D. Craig, E.E. Gualtieri, S. Hannuschke, R.A. Lacey, J. Lauret, T. Li, C.M. Mader, A. Nadasen, E. Norbeck, R. Pak, G. Peilert, N.T.B. Stone, A.M. Vander Molen, G.D. Westfall, J. Yee and S.J. Yennello, Phys. Rev. C **52**, 1900 (1995).

[Lópe89] J.A. López and J. Randrup, Nucl. Phys. **A491**, 477 (1989).

[Made93] C.M. Mader, Ph.D. Thesis, Michigan State University, 1993 (unpublished).

[More92] L.G. Moretto, K.Tso, N. Colonna and G.J. Wozniak, Phys. Rev. Lett. **69**, 1884 (1992).

[More93] L.G. Moretto and G.J. Wozniak, Ann. Rev. Nucl. Part. Sci. (May, 1993).

[More96] L.G. Moretto, T. Rubehn, L. Phair, N. Colonna, G.J. Wozniak, D.R. Bowman, G.F. Peaslee, N. Carlin, R.T. de Souza, C.K. Gelbke, W.G. Gong, Y.D. Kim, M.A. Lisa, W.G. Lynch and C. Williams, LBNL Preprint **LBL-38529**, Submitted to Phys. Rev. Lett. (1996).

[Ogil89] C.A. Ogilvie, D.A. Cebra, J. Clayton, S. Howden, J. Karn, A.M. Vander Molen, G.D. Westfall, W.K. Wilson and J.S. Winfield, Phys. Rev. C **40**, 654 (1989).

[Pak92] R. Pak, W.J. Llope, D. Swan, J. Wagner, G.D. Westfall, D. Craig, E. Gualtieri, S. Hannuschke, T. Li, N. Stone, A.M. Vander Molen and J. Yee, NSCL Annual Report, 233 (1992).

[Pak93] R. Pak, W.J. Llope, D. Swan, J. Wagner, G.D. Westfall, D. Craig, E. Gualtieri, S. Hannuschke, N. Stone, A.M. Vander Molen and J. Yee, NSCL Annual Report, 244 (1993).

[Pak96] R. Pak, Ph.D. Dissertation, Michigan State University, 1996 (Unpublished).

[Pana84] A.D. Panagiotou, M.W. Curtin, H. Toki, D.K. Scott and P.J. Siemens, Phys. Rev. Lett. **52**, 496 (1984).

[Past83] C. Pastor, F. Benrachi, B. Chambon, D. Drain, A. Dauchy, A. Giorni and C. Morand, Nuc. Inst. & Meth. **212**, 209 (1983).

[Peas94] G.F. Peaslee, M.B. Tsang, C. Schwarz, M.J. Huang, W.S. Huang, W.C. Hsi, C. Williams, W. Bauer, D.R. Bowman, M. Chartier, J. Dinius, C.K. Gelbke, T. Glasmacher, D.O. Handzy, M.A. Lisa, W.G. Lynch, C.M. Mader, L. Phair, M-C. Lemair, S.R. Souza, G. Van Buren, R.J. Charity, L.G. Sobotka, G.J. Kunde, U. Lynen, J. Pochadzalla, H. Sann, W. Trautmann, D. Fox, R.T. de Souza, G. Pielert, W. A. Friedman and N. Carlin, Phys. Rev. C **49**, R2271 (1994).

[Phai92] L. Phair, D.R. Bowman, C.K. Gelbke. W.G. Gong, Y.D. Kim, M.A. Lisa, W.G. Lynch, G.F. Peaslee, R.T. de Souza, M.B. Tsang and F. Zhu, Nucl. Phys. **A548**, 489 (1992).

[Phai93] L. Phair, W. Bauer and C.K. Gelbke, Phys. Lett. B **314**, 271 (1993).

[Pühl77] F. Pühlhofer, Nucl. Phys. **A280**, 267 (1977).

[Rich90] J. Richert and P. Wagner, Nucl. Phys. **A517**, 399 (1990).

[Rous93] P. Roussel-Chomaz, N. Collonna, Y. Blumenfeld, B. Liby, G.F. Peaslee, D.N. Delis, K. Hanold, M.A. McMahan, J.C. Meng, Q.C. Sui, G.J. Wozniak, L.G. Moretto, H.Madani, A.A. Marchetti, A.C. Mignerey, G. Guarino, N. Santoruvo, I. Iori and S. Bradley, Nucl. Phys. **A551**, 508 (1993).

[Sa85] Sa Ban-Hao and D.H.E. Gross, Nucl. Phys. **A437**, 643 (1985).

[Siwe93] K. Siwek-Wilczynska, J. Wilczynski, H.K.W. Leegte, R.H. Siemssen, H.W. Wilschut, K.Grotowski, A. Panasiewicz, Z. Sosin and A. Wieloch, Phys. Rev. C **48**, 228 (1993).

[Souz93] S.R. Souza and C.Ngô, Phys. Rev. C **48**, R2555 (1993).

[Souz94] S.R. Sourza, F. Schussler, R. Donangelo, K. Sneppen, J.P. Bondorf, R. Elmér, B. Jakobsson, S. Leray, C. Ngô and H. Nifenecker, Phys. Rev. C **50**, 257 (1994).

[Sowi86] M. Sowiński, M. Lewitowicz, R. Kupczak, A. Jankowski, N.K. Skobelev and S. Chojnacki, Z. Phys. A **324**, 87 (1986).

[Stan71] H.E. Stanley, *Introduction to Phase Transitions and Critical Phenomena*, (Oxford University Press, Oxford, 1971).

[Stau79] D. Stauffer, Phys. Rep. **54**, 1 (1979).

[Ston93] N. Stone, D. Craig, E. Gualtieri, S. Hannuschke, W. Llope, A. Nadasen, E. Norbeck, R. Pak, J. Yee, D. Swan, A. Vander Molen and G.D. Westfall, NSCL Annual Report, 240 (1993).

[Ston94] N.T.B Stone, G.D. Westfall, E.E. Gualtieri, S. Hannuschke, R. Pak, A.M. Vander Molen, W.J. Llope, D. Swan, R. Lacey and J. Lauret, NSCL Annual Report, 181 (1994).

[West85] G.D. Westfall, J.E. Yurkon, J. Van Der Plicht, Z.M. Koenig, B.V. Jacak, R. Fox, G.M. Crawley, M.R. Maier, B.E. Hasselquist, R.S. Tickle and D. Horn, Nucl. Inst, Meth. **A238**, 347 (1985).

[West93] G.D. Westfall, W. Bauer, D. Craig, M. Cronqvist, E. Gualtieri, S. Hannuschke, D. Klakow, T. Li, T. Reposeur, A.M. Vander Molen, W.K. Wilson, J.S. Winfield, J. Yee, S.J. Yennello, R. Lacey, A. Elmaani, J. Lauret, A. Nadasen and E. Norbeck, Phys. Rev. Lett. **71**, 1986 (1993).

[Xu93] H.M. Xu, J.B. Natowitz, C.A. Gagliardi, R.E. Tribble, C.Y. Wong and W.G. Lynch, Phys. Rev. C **48**, 933 (1993).

[Zhan87a] Zhang X.-Z., D.H.E. Gross, Xu S.-Y. and Zheng Y.-M., Nucl. Phys. **A461**, 641 (1987).

[Zhan87b] Zhang X.-Z., D.H.E. Gross, Xu S.-Y. and Zheng Y.-M., Nucl. Phys. **A461**, 668 (1987).